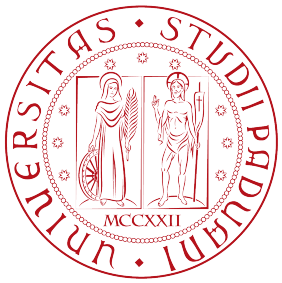

UNIVERSITÀ DEGLI STUDI DI PADOVA

Dipartimento di Fisica e Astronomia "Galileo Galilei"

Master Degree in Physics

Final Dissertation

Studying the CMB Polarization. Calibration and First Observations of the QUIJOTE 30 and 40 GHz Instruments

Thesis supervisor
Prof. Sabino Matarrese

Thesis co-supervisor
Prof. José Alberto Rubiño Martín

Candidate
Felice Antonio Martire

Academic Year 2018/2019

Abstract

Since its discovery in 1964, the Cosmic Microwave Background has been a crucial source of information about our Universe and a huge effort has been made to produce increasingly detailed maps of the CMB temperature field. The next frontier of CMB research involves measurements of its polarization, i.e. the orientation of the light perpendicular to the direction of propagation, which was first detected in 2002.
The possibility to constrain some theories about the Universe evolution at very early times, made the CMB polarization measurement one of the most discussed and challenge future objective in Physics.
In this work, we will treat the argument from two different points of view: in the fist two chapters we will explain how the CMB polarization is related to some Cosmological theoretical frameworks and we will dedicate the last three chapters to the past and actual CMB experiments, moreover, my contribution to the QUIJOTE Experiment.
The work comes from the experience made at the University of Padova with Professor Sabino Matarrese, who provided me the theoretical tools to deeply understand the subject, and the collaboration with Professor José Alberto Rubiño Martín and the QUIJOTE group, who showed and introduced me to the world of experimental research.

Contents

Chapter 1

The Universe at very Early Times

Cosmology is a branch of physics concerned with the studies of the origin and evolution of the Universe. In this first chapter we will present the Hot Big Bang theory, it is a model which describes how the Universe evolved from a very high-density state till today and offers a explanation for a broad range of phenomena. Moreover, we will show its limits and how to overcome these with the theory of cosmological inflation. In conclusion we present a discussion on the results of the inflationary theory and its relation with observable.

1.1 Hot Big Bang

The *Cosmological Principle* states that the Universe, on large scales, is isotropic and homogeneous, moreover, in 1929, Edwin Hubble showed experimentally the Universe is expanding. [1]
The geometry which describes an isotropic, homogeneous and expanding Universe is the *Robertson-Walker metric*

$$\mathrm{d}s^2 = -\mathrm{d}t^2 + a(t)^2\Big(\frac{\mathrm{d}r^2}{1-kr^2} + r^2(\mathrm{d}\theta^2 + \sin^2\theta\,\mathrm{d}\phi^2)\Big) \tag{1.1}$$

where: t is the cosmological proper time, the spatial variables (r, θ, ϕ) are the comoving coordinates of a point in space, $a(t)$ is a dimensionless scalar function of time and k is the curvature constant: if $k = 0$, no curvature, the Universe is intended as flat, if $k = 1$, positive curvature, the Universe is closed, finally, if $k = -1$, negative curvature, the Universe is open.
Causality is determined by the propagation of light in space, therefore, it makes sense define a new parameter: the *conformal time*

$$\tau = \int \frac{\mathrm{d}t}{a(t)} = \int \frac{1}{aH}\mathrm{d}\ln a \tag{1.2}$$

where $H = \dot{a}/a$ is the so-called *Hubble parameter*, it represents a fundamental cosmological parameter, indeed, it describes the rate of expansion of the Universe, its value is

$$H_0 = 100\ h^2\,\mathrm{km\,s^1\,Mpc^{-1}}$$

where the uncertainty in the parameter is contained in the factor $h \simeq 0.67$.
According to the General Relativity, photons follow null geodesic $\mathrm{d}s = 0$, so we can define the *comoving distance* as

$$\chi(\tau) = \pm\tau \tag{1.3}$$

being the speed of light the maximum velocity reached by particles, the comoving distance gives us the measure of the *event horizon* i.e. the set of points in causal contact.

Λ-*CDM*
The dynamics of the Universe is generally determined by the Einstein Equation

$$R_{\mu\nu} - \tfrac{1}{2} R\, g_{\mu\nu} = 8\pi G\; T_{\mu\nu} \tag{1.4}$$

where $R_{\mu\nu}$ is the Ricci curvature tensor, R is the scalar curvature, $g_{\mu\nu}$ is the metric tensor, G is Newton's gravitational constant and $T_{\mu\nu}$ is the stress-energy tensor. This equation is constrained from some assumptions: (i) the Universe is filled with the so called perfect cosmic fluid, i.e. fluid with null viscosity and without heat flows, which constrains the stress-energy tensor, (ii) on large scale we have the geometrical symmetries already described (1.1), thus, the Einstein Equation takes the form of the so called *Friedmann Equations*

$$H^2 = \left(\frac{\dot{a}}{a}\right)^2 = \frac{1}{3}\rho - \frac{k}{a^2} \tag{1.5}$$

$$\dot{H} + H^2 = \frac{\ddot{a}}{a} = -\frac{1}{6}(\rho + 3p). \tag{1.6}$$

Equations (1.5) and (1.6) may be combined into the *continuity equation*

$$\dot{\rho} + 3H(\rho + p) = 0 \tag{1.7}$$

where ρ is the energy density and p is the pressure of all elements that make up the Universe. A flat universe (k = 0) currently corresponds to the following critical energy density ($t = t_0$)

$$\rho_{crit,0} = \frac{3H_0^2}{8\pi G}. \tag{1.8}$$

The Lambda cold dark matter, or ΛCDM, is a the worldwide used parametrization of the cosmological model, according to this, the Universe is composed by four components: a *cosmological constant* (Λ) associated with dark energy, the cold dark matter (CDM), ordinary matter, or baryonic matter, and radiation. Each component evolved differently during the Universe history:

- *Matter*, bright and dark, is the massive component for which $p = 0$, and $\rho \propto a^{-3}$
- *Radiation* is the massless component for which $p = \frac{1}{3}\rho$ and $\rho \propto a^{-4}$
- *Dark energy* is a negative pressure component, $p = -\rho$ and ρ constant.

By mean of these definitions, we can rewrite the first Friedmann equation (1.5) in terms of the present values of the density parameters (1.8)

$$\frac{H^2}{H_0^2} = \Omega_{0,r} a^{-4} + \Omega_{0,m} a^{-3} + \Omega_{0,k} a^{-2} + \Omega_{0,\Lambda} \tag{1.9}$$

where $\Omega_{i,0} = \rho_{i,0}/\rho_{crit,0}$ and $\Omega_{k,0} = -k/H_0^2$.
The latest *Planck* observational results give the best current contribute values of each component

$$|\Omega_k| < 0.01, \quad \Omega_r = 9.4 \times 10^{-5}, \quad \Omega_m = 0.32, \quad \Omega_\lambda = 0.68.$$

The actual dominant component is the dark energy, which lead to an accelerated expansion of the Universe. Looking at the evolution equations of the single components, we can easily imagine that this is not always been the case; at the very early times we encounter a singularity point of infinite density, which we call *Big Bang*, it is placed around 13.8 billion years ago which is thus considered the age of the Universe; after that, the scale factor increases as function of time, consequently the temperature T decreases as function of time, with a roughly inverse relation $T \sim a^{-1}$, which lead to three different epochs: the radiation domination era, the matter domination era and the present dark energy domination era. What characterized the Universe before the Big Bang will be the central discussion on the further sections.
The four pillars of this Big Bang theory are the four direct observational evidences of the validity of the theory: the expansion of the Universe according to Hubble's law, the discovery and measurement of the Cosmic Microwave Background, the relative abundances of light elements produced during the Nucleosynthesis and observations of the distribution of large-scale cosmic structures.

Cosmic Microwave Background
The Cosmic Microwave Background (CMB) is the radiation coming from a spherical surface called *surface of last scattering* on the sky, that is the thermal radiation left over from the time of *recombination*. In principle, because of extreme temperature, matter was in a state of hydrogenic plasma and free electrons strongly interacted with photons through Thomson scattering, the Universe was opaque. As the expansion proceed, both plasma and radiation cooled down and once the electrons became stably bound to nuclei, atoms could not scatter the thermal radiation anymore and so the Universe became transparent i.e. the photons became free to propagate in space. The surface of last scattering, indeed, refers to the photons we are receiving now from the time of photon decoupling, when the Universe was 380 000 years old.

The CMB was discovered in 1964, two physicists: A. Penzias and B. Wilson were working at Bell Laboratories in New Jersey and what they thought was simple "noise" of their microwave antenna has earned them the Nobel prize in 1978, and since then, a great effort has been made to study and characterize the CMB with higher and higher precision, both with ground-based and satellite experiments.
Today, we know that the CMB contributes

$$\Omega_{CMB} \simeq 4.3 \times 10^{-5}\ h^{-2}$$

to the whole energy density of the Universe, it is characterize by a thermal *black body* spectrum at an average temperature of $T_{CMB} = 2.725\,\mathrm{K}$, the peak is at a frequency around 160 GHz, or wavelength of about 1 mm. It is extremely *isotropic*, fluctuations are very small, around

$$\langle \Big(\frac{\delta T}{T}\Big)^2 \rangle^{1/2} = \langle \Big(\frac{T(\underline{x}) - \langle T \rangle}{\langle T \rangle}\Big)^2 \rangle^{1/2} = 1.1 \times 10^{-5}$$

i.e. order of one part in 100 000 and it is *polarized* at the level of a few microkelvin.
The anisotropy is divided into two categories: primary anisotropy, due to effects which

occur before and at the last scattering surface, and secondary anisotropy, due to effects which occur after the last scattering surface as interaction with hot gasses or distortion by gravitational potentials.

1.2 Inflation Theory

The Big Bang Theory provides a very powerful and accurate description of the Universe as we know today and how it was till his very early times, but what there was before and why it happens to be like that is one of the most important questions that Modern Cosmology have to face. The theory described so far is a consequence of precisely such a fine-tuned set of initial conditions, but, seeing the Universe as an unlikely accident leads cosmologists to question the meaning and reasons for these conditions. [2]

Cauchy problem
The two mean conceptual issues with the standard Hot Big Bang scenario, which form the so-called Cauchy problem, are:

- The *Flatness* problem: the results of the type Ia supernova observations and the measurements of the CMB anisotropy are consistent with a flat Universe at our time
$$|1-\Omega|_0 = |\frac{k}{(aH)_0^2}| \leq 0.2 \tag{1.10}$$
the so-called *comoving Hubble radius* $(aH)^{-1}$, which represent the maximum distance between particles in causal contact, grows with time, therefore, the density parameter was closer to one in the past, i.e. the Universe was even flatter. Roughly, at the Planck epoch $t_p \approx 5 \times 10^{-44}$ s the Universe was extremely flat
$$|1-\Omega|_p \leq 10^{-60} \quad .$$
which represent a very unlikely casual initial condition.

- The *Horizon* problem: the homogeneity and isotropy of space are experimental assumptions, but there is no reason why it happens. Consider the Universe filled with a fluid described by the parameter $w = p/\rho$, pressure over energy density. The comoving distance (1.3) is then proportional to
$$(aH)^{-1} = \frac{1}{H_0^2} a^{\frac{1}{2}(1+3w)} \quad \text{so} \quad \chi = \pm\tau \propto \pm a^{\frac{1}{2}(1+3w)} \tag{1.11}$$
i.e. the comoving horizon grows monotonically with time. This means that at the time of the recombination, the event horizon was much smaller than the size of the Universe.
For instance, according to the ΛCDM, the current proper distance to the last scattering surface is a bit smaller than the horizon distance
$$\chi_p(t_0) = \int_{t_{ls}}^{t_0} \frac{\mathrm{d}t}{a(t)} = 0.98\chi_{hor}(t_0) \tag{1.12}$$

which means that the two points separated by 180°, as seen by an observer on Earth today, are currently separated by a proper distance of $1.96\chi_{hor}(t_0)$, therefore, they have never been in casual contact. Through the full computation, it is possible to prove that even two points on the sky with an angular separation exceeding 2°, should never have been in casual contact, but yet they are observed to have the same temperature to extremely high precision.
In other words, there is no reason why the CMB has the same temperature to within one part in 10^5 and, further, the small fluctuations show a perfect uniform correlation in all directions.

Inflation solution

A very intuitive solution for the Cauchy problem is to suppose that at very early times, before the Big Bang, everything was in casual contact, and then, an exponential expansion of space lead to the initial conditions of the Hot Big Bang scenario. This is the basic idea of the the cosmic *Inflation*. [3]
The Inflation theory was presented the first time by Alan Guth in 1979 in order to explain the problem concerning the absence of magnetic monopoles in the Universe, since then, it is became one of the most discussed topics of the modern Cosmology. Nowadays, the basic paradigm is supported by a series of observational evidences predicted by the different inflation models thus it is worldwide accepted by the majority of the physical community.
In formulas, if we assume the Universe passed from complete causality to the condition of not causal contact, we assume the existence of a period in which the comoving Hubble radius $(aH)^{-1}$, so the event horizon, decreases, i.e.

$$\frac{\mathrm{d}}{\mathrm{d}t}(aH)^{-1} = -\frac{\ddot{a}}{(aH)^2} < 0 \quad \text{so} \quad \ddot{a} > 0 \tag{1.13}$$

i.e. a period of accelerated expansion, for this the name *inflation*.
From the second Friedmann Equation (1.5)

$$\frac{\ddot{a}}{a} = -\frac{1}{6}(\rho + 3p) > 0 \quad \Leftrightarrow \quad p < \frac{1}{3}\rho \tag{1.14}$$

it is simple to understand that matter ($p = 0$) and radiation ($p = \rho/3$) cannot be the responsible of this acceleration, the only component which satisfies this inequality is the cosmological constant ($p = -\rho$). Therefore, the particle physics we know is not enough and not already discovered physical field can be the responsible for this inflation.
Back to the Cauchy problem, the Inflation paradigm (1.13) of Universe in casually contact directly solve the Horizon problem (1.13), but also the Flatness problem is simple solved: let generalize (1.10)

$$|1 - \Omega(t)| = \frac{k}{(a(t)H(t))^2} \tag{1.15}$$

and evaluate the rate at beginning (t_i) and end (t_f) of Inflation

$$|1 - \Omega(t_f)| = \frac{a(t_f)}{a(t_i)}\ |1 - \Omega(t_i)| \tag{1.16}$$

it turns out: whatever the very initial curvature is ($\Omega(t_i)$), after inflation it is reduced by the the factor $a(t_f)/a(t_i)$. Therefore, the extreme flatness of the Universe at the

Planck scale is not a coincidence, but a consequence of the exponential expansion.

Different Inflation models have been developed across the years. Because a simple cosmological constant does not fit for a dynamical process, first models investigated the possible responsible quantum fields, whose vacuum state reproduces the constant Λ. The simplest model involves a scalar quantum field $\phi(x,t)$, the *Inflaton*, function of position and time and characterize by a potential energy density $V(\phi)$ and a kinetic energy $\dot{\phi}^2/2$.

Slow-roll conditions
In order to have an efficient Inflation which solves the Cauchy problem, many models shear two constrains which have to be respected, the Slow-roll conditions:

- First condition arises from the fact that $p < \rho/3$, therefore the potential $V(\phi)$ must be much larger than the kinetic term $\dot{\phi}^2/2$ in order to have an exponential expansion
$$\dot{\phi}^2 \ll V(\phi) \;:\; \epsilon \doteq -\frac{\dot{H}}{H^2} = \frac{1}{2}\frac{\dot{\phi}^2}{H^2} < 1 \tag{1.17}$$
- Second condition arises from the fact that this state of accelerated expansion has to persist for a sufficiently long period of time, therefore, the evolution of the field must be slightly constant
$$|\ddot{\phi}| \ll |H\dot{\phi}| \;:\; \eta \doteq -\frac{\ddot{\phi}}{H\dot{\phi}} < 1 \tag{1.18}$$

These two conditions are preserved when the two parameters ϵ and η, called *slow-roll parameters*, are small. The end of Inflation happens when they both approach one. For simplicity, they are usually considered constant at first order during Inflation, but in reality they are dynamical variables and their actual values depends on the model we are considering.
The following treatment of the Inflation evolution led by a single scalar field will be as general as possible, but we will often look back to the Slow-roll models. Moreover, it is important to mention there a class of models defined *hybrid* which can present completely different features, for instance, more than one inflaton fields, which need more sophisticated treatments.

Klein-Gordon equations
The dynamics of the Inflaton field coupled to gravity is completely determined by the *action*
$$S = \int \mathrm{d}^4x\sqrt{-g}\,\left(\frac{1}{2}R + \frac{1}{2}g^{\mu\nu}\partial_\mu\phi\partial_\nu\phi - V(\phi)\right) = S_{EH} + S_\phi \tag{1.19}$$
where S_ϕ is the action of a scalar field with canonical kinetic term and S_{EH} represents the gravitational contribution. According to the variational principle, imposing $\delta S = 0$, we obtain the equation of motion of the inflaton field
$$\Box\phi = \frac{\partial V}{\partial\phi} \;\longrightarrow\; \ddot{\phi} + 3H\dot{\phi} - \frac{\nabla^2\phi}{a^2} = -\frac{\partial V}{\partial\phi} \tag{1.20}$$
it is the Klein-Gordon equation of a scalar field in a RW metric.
The inflaton field is a quantum field and can always be seen as combination of an

homogeneous background $\bar{\phi}(t)$ and a small perturbation $\delta\phi(t, \mathbf{x})$ depending on time and space

$$\phi(t, \mathbf{x}) = \bar{\phi}(t) + \delta\phi(t, \mathbf{x}). \tag{1.21}$$

The inflaton field is the only component which filled the Universe at very early times, thus the only component in the stress-energy tensor $T_{\mu\nu}$. Therefore, according to the Einstein Equation (1.4), fluctuations of the field $\delta\phi$, which means fluctuations in the stress-energy tensor $\delta T_{\mu\nu}$, lead to fluctuations in the metric itself

$$g_{\mu\nu}(t, \mathbf{x}) = \bar{g}_{\mu\nu}(t) + \delta g_{\mu\nu}(t, \mathbf{x}) \tag{1.22}$$

where $\bar{g}_{\mu\nu}$ in our case is the RW metric (1.1) and $\delta g_{\mu\nu}$ enters in the Klein-Gordon equation as metric perturbations. Some details: let consider a metric composed of FRW background metric plus perturbations at first order

$$ds^2 = -dt^2 + a(t)^2(\delta_{ij} + h_{ij}(t, \vec{x}))dx^i dx^j \tag{1.23}$$

in this case, we neglect scalar and vector contributions and deal only with tensor perturbations h_{ij} which have some important properties:

$$h_{ij} = h_{ji}, \qquad h^i_j = 0 \qquad h^i_{j,i} = 0. \tag{1.24}$$

Solving the Einstein Equation at first perturbation order $\delta G^j_i = \delta R^j_i$ (the Ricci scalar is unperturbed by tensor modes) and performing the definition of Einstein tensor and Ricci tensor, we obtain an equation for the dynamic of $h_{ij}(t, \vec{x})$

$$\ddot{h}_{ij} + 3\frac{\dot{a}}{a}\dot{h}_{ij} - \frac{\nabla^2}{a^2}h_{ij} = 0. \tag{1.25}$$

It is pretty clear that equations (1.20) and (1.25) have exactly the same form, the only crucial difference is that the equation of the Inflaton field, or *Scalar modes*, have a source term $\partial_\phi V$, instead, the equation of the metric perturbations, or *Tensor modes*, does not.
In other words, the standard Inflation theory predicts the formation of tensor perturbations, which are noting else that *Primordial Gravitational Waves*, which evolve independently by the field itself.
It is important to specify that the coordinates t and $\mathbf{x}$ for an homogeneous description of spacetime are defined by the symmetry of the space itself, and this is no longer true for a perturbed spacetime, the *gauge choice* is indeed crucial. The choice of some coordinates rather than others can introduce fictitious perturbations or, on the contrary, remove real perturbations, therefore, a full treatment of the so-called *Cosmological perturbation theory* is required.

Primordial Perturbations
Concerning the Scalar mode, we only mention the standard procedure in order to solve the equation (1.20) at first perturbation order: (i) we introduce some gauge-invariant quantities, as the *Sasaki-Mukhanov variable*, (ii) move to Fourier space and (iii) quantize the field. It ends up that the Scalar modes evolve independently till they become larger than the horizon scale and at this point they *freeze out*. However, the inflaton field dominates the energy density of the Universe during Inflation

$$\delta\phi \;\longrightarrow\; \delta\rho \simeq \partial_\phi V \;\delta\phi \simeq -3H\dot{\phi}\;\delta\phi \tag{1.26}$$

thus, fluctuations of the field produce fluctuations in the Universe expansion from place to place. Each region in the Universe goes through the same expansion history but at slightly different times

$$\delta t = -\frac{\delta\phi}{\dot{\phi}}. \tag{1.27}$$

Let define the *uniform energy density curvature perturbation*, which is in general a gauge-invariant quantity, but takes the following form in the so-called uniform curvature gauge

$$\zeta = H\delta t = -H\frac{\delta\phi}{\dot{\phi}} = -H\frac{\delta\rho}{\dot{\rho}} \tag{1.28}$$

because the field fluctuations freeze out, it remains constant on super-horizon scale till inflation ends, radiation dominance epoch occurs and the modes renter the horizon.
To summarize: (i) quantum fluctuations of the inflaton field at the time of inflation evolve mode by mode independently; (ii) when a mode becomes larger of the horizon, or more exactly the horizon decreases because of the exponential expansion and becomes smaller than the mode, the fluctuations freeze out; (iii) the Universe expansion proceed, inflation ends and radiation dominates the Universe; (iv) the expansion slows down and the modes re-enter the horizon. At this last point, modes re-enter not as field quantum fluctuations but as physical energy density fluctuations (1.28) of the main Universe component at that time, i.e. radiation.
These fluctuations evolved in time, as we will see in the next chapter, and characterized radiation till the recombination era and finally they imprinted a signature on the surface of last scattering. This is the Inflationary explanation of the CMB temperature *anisotropy*, which we observe nowadays.
Concerning the Tensor Mode, a completely analogous computation is performed, only difference is that it is not required any further definitions because tensor perturbations are gauge-invariant by construction. Exactly as for the scalar modes, the simple metric perturbations will lead to observable nowadays, but only when the polarization of the CMB is considered, this will be presented in full details in the following sections.

1.3 Scalar and Tensor Modes

Primordial scalar fluctuations, parameterized by the comoving curvature pertubation ζ (1.28), and primordial tensor fluctuations, parameterized by the two polarization modes $h_{ij}^{+}, h_{ij}^{\times}$ are conventionally treated with a Statistical approach. [3]

Power Spectra
First of all, we recall the definition of the two-point correlation function

$$\xi(r) = \left\langle \delta(\mathbf{x})\delta(\mathbf{x}+\mathbf{r}) \right\rangle \tag{1.29}$$

where: $\delta(t, \mathbf{x})$ is a general field, which can stand for our inflaton field fluctuations $\delta\phi$ or metric fluctuations $h_{ij}^{+,\times}$, and $\langle\cdot\rangle$ represents the ensemble average which is function only of the distance r between two points.
Let move to Fourier space

$$\delta_{\mathbf{k}} = \int \mathrm{d}^3x \ \delta(\mathbf{x}) e^{-i\mathbf{k}\cdot\mathbf{x}} \tag{1.30}$$

we define the *power spectrum* $\mathcal{P}$ by mean of the equivalence

$$\left\langle \delta_{\mathbf{k}} \delta_{\mathbf{k}'} \right\rangle = (2\pi)^3 \mathcal{P}(k) \delta^{(3)}(\mathbf{k} + \mathbf{k}') \tag{1.31}$$

where $\delta^{(3)}$ is the three-dimensional Dirac function. It is easy to prove that the power spectrum is noting more than the Fourier transform of the two-point correlation function

$$\mathcal{P}(k) = \int \mathrm{d}^3 r \; \xi(r) e^{-i\mathbf{k}\cdot\mathbf{r}}. \tag{1.32}$$

A very useful and important parameter in statistical analysis is the *variance*

$$\sigma^2 = \left\langle \delta^2(x) \right\rangle = \int \mathrm{d}^3 k \; \mathcal{P}(k) = \int \mathrm{d} \ln k \; \Delta^2(k) \tag{1.33}$$

where in the last equivalence we performed a redefinition of the power spectra which is commonly used in Cosmology

$$\Delta^2(k) = \frac{k^3}{2\pi^2} \mathcal{P}(k). \tag{1.34}$$

In the inflationary context, we can distinguish two different power spectra: the scalar power spectrum Δ_s, for the inflaton field or energy density, and the tensor power spectrum Δ_t, for the gravitational waves.
The power spectrum could be in general any function of the scale k, but it is typically thought to be a polynomial function, therefore the scale dependence of the scalar power spectrum is parameterized by the *scalar spectral index*, or *tilt*,

$$n_s - 1 \doteq \frac{\mathrm{d} \ln \Delta_s^2}{\mathrm{d} \ln k} \tag{1.35}$$

instead, the scale dependence of the tensor power spectrum is parameterized by the *tensor spectral index*

$$n_t \doteq \frac{\mathrm{d} \ln \Delta_t^2}{\mathrm{d} \ln k}. \tag{1.36}$$

Finally, we can define the *tensor-to-scalar ratio* which mostly will return in the next sections, it is a measure of the ratio between the power spectrum of tensor over the scalar one

$$r \doteq \frac{\Delta_t^2(k)}{\Delta_s^2(k)} \tag{1.37}$$

it is an extremely important quantity in Cosmology.

Inflation predictions
Till now, we kept things very general, but now let focus on the Slow-roll models. It is possible to perform the full computation (1.20-1.25) analytically, the final solutions for the scalar and tensor power spectra are

$$\Delta_s^2(k) = \frac{H^2}{(2\pi)^2} \frac{H^2}{\dot{\phi}^2} \Big|_{aH=k} \quad \Delta_t^2 = \frac{2}{\pi^2} \frac{H^2}{M_{pl}^2} \Big|_{aH=k} \tag{1.38}$$

where M_{pl}^2 is the reduced Planck mass and the parameters H and $\dot{\phi}$ have to be evaluated at the horizon crossing i.e. when the k-mode is equal to the inverse comoving Hubble radius aH. The tensor-to-scalar ratio is then

$$r = 16\epsilon \; _{|aH=k} = -8 n_t. \tag{1.39}$$

These results are telling us two very important things, which hold besides the inflationary model itself:

- The tensor-to-scalar ratio is of the order of the slow-roll parameter at the horizon crossing, thus, recalling the slow-roll condition (1.17), it is supposed to be very small. For some models, as the so-called *chaotic*, it is expected to be $r \geq 10^{-2}$, but, for other models, especially *hybrid* models, it can be very small, up to $r \sim 10^{-10}$; anyway, a direct measure of r is a very challenging experimental goal.

- Slow-roll conditions lead to a linear relation between tensor-to-scalar ratio r and the tensor spectral index n_t, this is what we call *consistency relation*. No other physical mechanism can provide such relation, thus, a possible experimental probe is a unequivocal evidence of the Inflationary theory.

Finally, recalling the order of CMB temperature anisotropy 10^{-5}, we know that $\Delta_s \sim 10^{-10}$, thus we can some put constraints

$$V^{1/4} \sim \left(\frac{r}{0.01}\right)^{1/4} 10^{16}\ GeV \tag{1.40}$$

the tensor-to-scalar ration is directly related to the inflaton potential so to the inflationary energy, $H^2 \sim V$, and gives us an hint of the physics at these extreme energies.

In conclusion, we summarize the reasons why it is very important to measure the the tensor-to-scalar ratio: (i) it is a direct evidence of the Inflationary theory, (ii) its value is directly related to the energy of the Inflation, (iii) it would pick the right inflationary model among the several proposed ones, (iv) it would give us an important clue on the physics of fundamental interactions at very early times.

Chapter 2

CMB Polarization Modes and Evolution

Polarization, also called wave polarization, is an expression of the orientation of the lines of electric flux in an electromagnetic field. [4, 5]
In the following chapter, we will give some useful definitions and a formal mathematical approach to treat the polarization problem. In conclusion, through the Radiation Transport equation we will present some very important result related to the CMB observable.

2.1 Stokes parameters

The polarization state of electromagnetic waves is described by a set of variables called the Stokes parameters, they take the name by George Gabriel Stokes, which gave the first definition in 1852. The relationship of the Stokes parameters $S_0,\ S_1,\ S_2,\ S_3$ to intensity and polarization ellipse parameters are

$$\begin{aligned} S_0 &= I \\ S_1 &= Ip\cos 2\psi \cos 2\chi \\ S_2 &= Ip\sin 2\psi \cos 2\chi \\ S_3 &= Ip\sin 2\chi \end{aligned} \tag{2.1}$$

where I is the total intensity of the beam and p is the degree of polarization, constrained by $0 \leq p \leq 1$. $I,\ p,\ 2\psi$ and 2χ are the spherical coordinates of the three-dimensional vector of Cartesian coordinates $(S_1,\ S_2,\ S_3)$, the phase information of the polarized light is not explicitly expressed by the Stokes parameters.
The four Stokes parameters are not a preferred coordinate system of the space, but they can be easily measured or calculated, this make the parameters very useful. In this context, they are usually denoted I, Q, U and V, respectively.
Their physical meaning becomes much more easily understandable if we consider a monochromatic electromagnetic wave propagating in the $\hat{z}$ direction

$$\begin{aligned} E_x &= a_x \cos(\omega t - \xi_x) \\ E_y &= a_y \cos(\omega t - \xi_y) \end{aligned} \tag{2.2}$$

the intensity is defined as usually as

$$I = a_x^2 + a_x^2 \tag{2.3}$$

and the linear-polarization parameters, which we commonly refer as Stokes parameters, are

$$\begin{aligned} Q &= a_x^2 - a_x^2 \\ U &= 2a_x a_y \cos(\xi_x - \xi_y) \end{aligned} \tag{2.4}$$

Q quantifies the polarization in the x-y direction while the U along the axes rotated by 45°.
The last parameter V, which quantifies the circular-polarization, plays no rules in our cosmological context, especially because we will see in next sections that Thomson scattering does not induce circular polarization.
The polarization tensor field is a symmetric trace-free 2×2 tensor which is construct by the two Stokes parameters Q and U

$$P_{ij} = \begin{pmatrix} Q & U \\ U & -Q \end{pmatrix} \tag{2.5}$$

thus, Q and U can be thought as the diagonal and off-diagonal components of the symmetric, traceless, 2 intensity matrix in the polarization plane spanned by $(\hat{e}_\theta, \hat{e}_\phi)$. Under a generic coordinate transformation, P_{ij} transforms as

$$x_i' = A_i^k x_k \longrightarrow P_{ij}' = A_i^k A_j^l P_{kl} \tag{2.6}$$

therefore, it is simple to see that under a rotation of the x-y axes, by an angle α about the line of sight $\hat{z}$, the Stokes parameters (Q, U) transform as

$$\begin{pmatrix} Q' \\ U' \end{pmatrix} = \begin{pmatrix} \cos 2\alpha & \sin 2\alpha \\ -\sin 2\alpha & \cos 2\alpha \end{pmatrix} \begin{pmatrix} Q \\ U \end{pmatrix}. \tag{2.7}$$

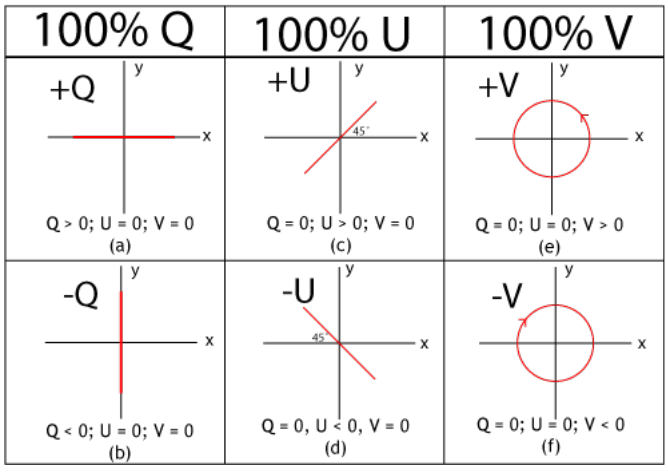

Figure 2.1: Stokes parameters in some degenerate cases. [6]

E-mode and B-mode

From the polarization tensor, we can naturally recognize two different types of polarization: E-mode and B-mode.
Locally, this separation is understand involving the second derivatives of the polarization tensor field. The E-mode is the gradient component

$$\nabla^2 P_{\rm E} = \partial_i \partial_j P_{ij} \tag{2.8}$$

indeed, the name comes from the analogy with electrostatics, in which the electric field, or E-field, has a vanishing curl; instead, the B-mode is the curl components

$$\nabla^2 P_{\rm B} = \epsilon_{ik} \partial_j \partial_k P_{ij} \tag{2.9}$$

in analogy with the magnetic field, or$B$-field, which has a vanishing divergence. Note as in equations (2.8)-(2.9), P_{ij} depends on the angle of θ from which the radiation is coming from, but it is independent from the orientation of the x-y axes, where ϵ_{ij} is the anti-symmetric tensor. Sometimes, E-mode and B-mode are called respectively G-mode and C-mode, because of their local definition.
let move to the Fourier space

$$\tilde{P}_{ij}(\vec{l}) = \int d^2\vec{\theta}\; P_{ij}(\vec{\theta}) e^{i\vec{l}\cdot\vec{\theta}} \tag{2.10}$$

(2.8)-(2.9) take the form

$$\tilde{P}_E(\vec{l}) = \frac{1}{2}\frac{(l_x^2 - l_y^2)\tilde{Q}(\vec{l}) + 2l_x l_y \tilde{U}(\vec{l})}{l_x^2 + l_y^2} \qquad \tilde{P}_B(\vec{l}) = \frac{1}{2}\frac{2l_x l_y \tilde{Q}(\vec{l}) - (l_x^2 - l_y^2)\tilde{U}(\vec{l})}{l_x^2 + l_y^2}. \tag{2.11}$$

The mode decomposition has also a globally property meaning: in a spherical harmonic decomposition, the harmonics of an E-mode have $(-1)^\ell$ parity on the sphere, whereas those of a B-mode have $(-1)^{\ell+1}$ parity. Therefore, under $\hat{n} \to -\hat{n}$ direction transformation, the E-mode remains unchanged for even ℓ, whereas the B-mode changes sign.

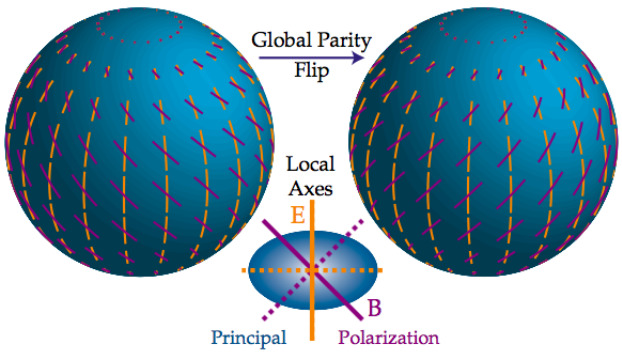

Figure 2.2: Behavior of E-mode and B-mode under a parity transformation. In this case ($\ell = 2, m = 0$): even for the electric mode and odd for the magnetic mode. [7]

Correlation functions

In the previous chapter, we presented the power spectra and their relevance in Cosmology, therefore, it is important to explain how polarization fits in this contest. Here, we present the simple case of *flat sky* which is a very good approximation to use when we are analyzing small fractions of the sky, moreover, this will give a simple flavour on what we will present more formally in the next section on the analysis of the Full Sky. [5]

In analogy with what is conventionally done with temperature, we define the correlation function in general as

$$\left\langle \tilde{X}_1(\vec{l})\ \tilde{X}_2(\vec{l'})\right\rangle = (2\pi)^2\delta(\vec{l}+\vec{l'})\ C_l^{X_1X_2} \tag{2.12}$$

where X_1, X_2 can be T, $P_{\rm E}$ or $P_{\rm B}$, in this way we include single component correlation and cross-correlation, such as the correlation between polarization and temperature. The correlation function of the temperature is simple well-defined because temperature is a scalar and its correlation function only depends on the distance of the points. On the contrary, Q and U are not rotational invariant, therefore the correlation function for polarization is not trivial at all.

We need to introduce two new quantities Q_r and U_r which arise when polarization is defined with respect to the line connecting the two points, in this way, we can find the rotational-invariant correlation functions

$$\begin{aligned}
\left\langle Q_r(\vec{\theta}_1)\ Q_r(\vec{\theta}_2)\right\rangle =& C^{QQ}\left(|\vec{\theta}_1-\vec{\theta}_2|\right)\\
\left\langle U_r(\vec{\theta}_1)\ U_r(\vec{\theta}_2)\right\rangle =& C^{UU}\left(|\vec{\theta}_1-\vec{\theta}_2|\right)\\
\left\langle Q_r(\vec{\theta}_1)\ U_r(\vec{\theta}_2)\right\rangle =& C^{QU}\left(|\vec{\theta}_1-\vec{\theta}_2|\right).
\end{aligned} \tag{2.13}$$

In terms of E and B mode

$$\begin{aligned}
(C^{QQ}+C^{UU})(\theta) =& -\int_0^\infty \frac{l\,dl}{\pi}[C_l^{EE}+C_l^{BB}]J_0(l\theta),\\
(C^{QQ}-C^{UU})(\theta) =& -\int_0^\infty \frac{l\,dl}{\pi}[C_l^{EE}-C_l^{BB}]J_4(l\theta),
\end{aligned} \tag{2.14}$$

where $J_\nu(x)$ are Bessel functions. The mean-square polarization intensity is given by the correlation functions at zero lag

$$\left\langle P^2\right\rangle = \left\langle Q^2+U^2\right\rangle = \int_0^\infty \frac{l\,dl}{2\pi}[C_l^{EE}+C_l^{BB}] = \left\langle P_G^2\right\rangle + \left\langle P_{\rm C}^2\right\rangle. \tag{2.15}$$

2.2 Total Angular Momentum Method

In this section, we introduce the total angular momentum representation for the normal modes of fluctuations in a flat Universe that are used to describe metric and matter perturbations as well as the CMB temperature and polarization.

It is a formal mathematical approach with the purpose of isolate the total angular dependence of the modes which corresponds directly to the angular distribution of temperature and polarization, whereas the radial structure determines how distant

sources contribute to this angular distribution.
This method has the advantage of includes the effect of scalar and tensor perturbations on an equal footing, employing at the end only observable quantities. [7, 8]

Angular modes
The spherical harmonics are a complete set of orthogonal functions on the sphere, and thus, may be used to represent functions defined on the surface of the Sky. For instance, a spin-0 field, which is a scalar function such as the CMB temperature, can be decomposed into spherical modes Y_l^m. Likewise, a spin-s field on the sky can be decomposed into the spin-weighted spherical harmonics ${}_sY_l^m$ and a tensor constructed out by the basis vectors $\hat{e}_\theta \pm \hat{e}_\phi,\ \hat{e}_r$.
Thus, a basis for a spin-2 field as the CMB polarization is

$$\pm_2 Y_\ell^m M_\pm \tag{2.16}$$

where the spherical harmonics can be expressed as

$$\begin{aligned} {}_sY_\ell^m(\theta,\phi) &= \left[\frac{2\ell+1}{4\pi}\frac{(\ell+m)!(\ell-m)!}{(\ell+s)!(\ell-s)!}\right]^{1/2}(\sin\theta/2)^{2\ell} \\ &\times \sum_r \begin{pmatrix} \ell-s \\ r \end{pmatrix}\begin{pmatrix} \ell+s \\ r+s-m \end{pmatrix}(-1)^{\ell-r-s}e^{im\phi}(\cot\theta/2)^{2r+s-m} \end{aligned} \tag{2.17}$$

and $M_\pm$ are 2×2 symmetric traceless tensors

$$M_\pm = \frac{1}{2}(\hat{e}_\theta \pm i\hat{e}_\phi)\otimes(\hat{e}_\theta \pm i\hat{e}_\phi). \tag{2.18}$$

The spin-s spherical harmonics are tightly related to the rotation matrices

$${}_sY_m^\ell(\theta,\phi) = \left(\frac{2\ell+1}{4\pi}\right)^{1/2}\mathcal{D}^\ell_{-s,m}(\phi,\theta,0) \tag{2.19}$$

therefore, they show very interesting and important properties:

- compatibility with simple spherical harmonics and conjugation relation

$${}_0Y_\ell^m = Y_\ell^m, \qquad {}_sY_\ell^{m\star} = (-1)^{m+s}{}_{-s}Y_\ell^{-m} \tag{2.20}$$

- orthonormality relation

$$\int d\Omega\ ({}_sY_\ell^{m*})({}_sY_\ell^m) = \delta_{m,m'}\delta_{\ell,\ell'} \tag{2.21}$$

- completeness relation

$$\sum_{\ell,m}\left[{}_sY_\ell^{m*}(\theta,\phi)\right]\left[{}_sY_\ell^m(\theta',\phi')\right] = \delta(\phi-\phi')\delta(\cos\theta-\cos\theta') \tag{2.22}$$

- parity transformation

$${}_sY_\ell^m \to (-1)^\ell{}_{-s}Y_\ell^m \tag{2.23}$$

- generalized addition relation

$$\sum_m \left[{}_{s_1}Y_{m*}^\ell(\theta',\phi')\right]\left[{}_{s_2}Y_m^\ell(\theta,\phi)\right] = \sqrt{\frac{2\ell+1}{4\pi}}\left[{}_{s_2}Y^\ell_{-s_1}(\beta,\alpha)\right]e^{-is_2\gamma} \tag{2.24}$$

- Clebsch-Gordan relation

$$\begin{aligned}\left({}_{s_1}Y^{m_1}_{\ell_1}\right)\left({}_{s_2}Y^{m_2}_{\ell_2}\right) =& \frac{\sqrt{(2\ell_1+1)(2\ell_2+1)}}{4\pi}\sum_{\ell,m,s}\langle \ell_1,\ell_2;m_1,m_2|\ell_1,\ell_2;\ell,m\rangle \\ & \times\langle \ell_1,\ell_2;-s_1,-s_2|\ell_1,\ell_2;\ell,-s\rangle\sqrt{\frac{4\pi}{2\ell+1}}\ ({}_sY^m_\ell)\,.\end{aligned} \tag{2.25}$$

For the spin-2 harmonics, relevant for our polarization studies, the higher ℓ harmonics are related to the ordinary spherical harmonics as

$${}_{\pm2}Y^\ell_m = \left[\frac{(\ell-2)!}{(\ell+2)!}\right]^{1/2}\left[\partial^2_\theta - \cot\theta\,\partial_\theta \pm \frac{2i}{\sin\theta}(\partial_\theta - \cot\theta)\partial_\phi - \frac{1}{\sin^2\theta}\partial^2_\phi\right]Y^m_\ell. \tag{2.26}$$

m	Y^m_2	${}_2Y^m_2$
2	$\frac{1}{4}\sqrt{\frac{15}{2\pi}}\,\sin^2\theta\, e^{2i\phi}$	$\frac{1}{8}\sqrt{\frac{5}{\pi}}\,(1-\cos\theta)^2\, e^{2i\phi}$
1	$\sqrt{\frac{15}{8\pi}}\sin\theta\,\cos\theta\, e^{i\phi}$	$\frac{1}{4}\sqrt{\frac{5}{\pi}}\sin\theta\,(1-\cos\theta)\, e^{i\phi}$
0	$\frac{1}{2}\sqrt{\frac{5}{4\pi}}\,(3\cos^2\theta-1)$	$\frac{3}{4}\sqrt{\frac{5}{6\pi}}\,\sin^2\theta$
-1	$-\sqrt{\frac{15}{8\pi}}\sin\theta\,\cos\theta\, e^{-i\phi}$	$\frac{1}{4}\sqrt{\frac{5}{\pi}}\,\sin\theta\,(1+\cos\theta)\, e^{-i\phi}$
-2	$\frac{1}{4}\sqrt{\frac{15}{2\pi}}\,\sin^2\theta\, e^{-2i\phi}$	$\frac{1}{8}\sqrt{\frac{5}{\pi}}\,(1+\cos\theta)^2\, e^{-2i\phi}$

Table 2.1: Quadrupole ($\ell = 2$) harmonics for spin-0 and spin-2 field.

Note as the property (2.23) shows as the spin flips with parity transformations, therefore, besides the $s = 0$ spherical harmonics, the higher spin harmonics are not parity-invariant. Orthonormal parity states can be constructed as

$$\frac{1}{2}({}_sY^m_\ell M_+ \pm {}_{-s}Y^m_\ell M_-) \tag{2.27}$$

which have 'electric' $(-1)^\ell$ and 'magnetic' $(-1)^{\ell+1}$ type parity for the $(\pm)$ states respectively.

Radial modes

Up to now, we have seen the properties and some explicit forms of the generalized spherical harmonics, which, in some sense, represent the angular dependence of a spin-s fields. To find a compete basis we need to explore the 'position' dependence.
In the case of a scalar field, we know that in flat space plane waves form a complete basis for the spatial dependence

$$G^m_l = (-i)^\ell\sqrt{\frac{4\pi}{2\ell+1}}\ Y^m_\ell(\hat{n})\ \exp(\vec{k}\cdot\vec{x}) \tag{2.28}$$

In perfect analogy, a basis for a spin-2 field is

$${}_{\pm2}G^m_\ell = (-i)^\ell\sqrt{\frac{4\pi}{2\ell+1}}\ {}_{\pm2}Y^m_\ell(\hat{n})\ \exp(\vec{k}\cdot\vec{x}). \tag{2.29}$$

If we want to isolate the angular dependence of the modes, we have to be careful because plane waves also carry an angular dependence themselves

$$\exp(\vec{k}\cdot\vec{x}) = \sum_{\ell'}(-i)^{\ell'}\sqrt{4\pi(2\ell'+1)}\; j_{\ell'}(kr)\; Y^0_{\ell'}(\hat{n}) \tag{2.30}$$

where $\hat{e}_3 = \hat{k}$ and $\hat{x} = -r\hat{n}$.
Note as equations (2.29) and (2.30) show as the separation in angular and position dependence is essentially a separation into spin (${}_sY^m_{\ell'}$) and orbital (Y^0_l) angular momentum.
We now rearrange (2.29) in order to have a function of the total angular momentum, i.e. the sum of the two angular momenta ℓ and ℓ', which is the only observable quantity. To do so, we use the Clebsch-Gordan relation (2.25) and the recursion properties of spherical Bessel functions; we end up for spin-0 field ($m > 0$)

$$G^m_\ell = \sum_\ell (-i)^\ell \sqrt{4\pi(2\ell+1)}\; j^{(\ell',m)}_\ell(k,r)\; Y^m_\ell(\hat{n}) \tag{2.31}$$

and for spin-2 field ($m > 0$)

$${}_{\pm2}G^m_\ell = \sum_\ell (-i)^\ell \sqrt{4\pi(2\ell+1)}\; (\epsilon^{(m)}_\ell(kr) \pm i\beta^{(m)}_\ell(kr))\; {}_{\pm2}Y^m_\ell(\hat{n}). \tag{2.32}$$

Two different radial functions ϵ_l and β_l, related to the Bessel functions j_l, arise naturally; the analytic form of the lowest order are presented in Appendix A.2. Here we report what will be a fundamental result: the ratio β_l over ϵ_l reaches the asymptotic values of

$$\frac{\sum_\ell\, [\ell\; \beta^{(m)}_\ell]^2}{\sum_\ell\, [\ell\; \epsilon^{(m)}_\ell]^2} = \begin{cases} 0 & m = 0 \\ 6 & m = \pm 1 \\ 8/13 & m = \pm 2 \end{cases}$$

In other words, the addition of spin-2 angular momenta introduces a contribution β_ℓ which is zero for $m = 0$, strongly dominates over ϵ_ℓ for $m = \pm1$ and is slightly smaller than ϵ_ℓ for $m = \pm2$.

As seen in equation (2.27), the angular modes do not mix states of different spin, but, the multiple expansion does mix states of different parity since plane waves do not have definite parity.
The simplest state with electric parity in the intrinsic angular dependence is

$$\begin{aligned} &{}_2G^m_2 M_+ +_{-2} G^m_2 M_- = \sum_\ell (-i)^\ell \sqrt{4\pi(2\ell+1)} \\ &\times \Big\{\epsilon^{(m)}_\ell [{}_2Y^m_\ell M_+ +_{-2} Y^m_\ell M_-] + i\beta^{(m)}_\ell [{}_2Y^m_\ell M_+ -_{-2} Y^m_\ell M_-]\Big\}. \end{aligned} \tag{2.33}$$

Thus, the angular momentum addiction generates 'magnetic' B-type parity of amplitude β_ℓ out of an intrinsically 'electric' E-type source as well as E-type parity of amplitude ϵ_ℓ. The behavior of the two radial functions has significant consequences for the polarization.

Moments and Power Spectra
Finally we can expand temperature and polarization fluctuations into the normal

modes

$$\begin{aligned}\Theta(\eta,\vec{x},\hat{n}) &= \int \frac{d^3k}{(2\pi)^3}\sum_{\ell}\sum_{m=-2}^{2}\Theta_\ell^{(m)}G_\ell^m \\ (Q\pm iU)(\eta,\vec{x},\hat{n}) &= \int \frac{d^3k}{(2\pi)^3}\sum_{\ell}\sum_{m=-2}^{2}(E_\ell^{(m)}\pm iB_\ell^{(m)})_{\pm2}G_\ell^m.\end{aligned} \tag{2.34}$$

where $\Theta = \Delta T/T$.
Equation (2.34) is showing clearly what we anticipated in the previous section: $E_\ell^{(m)}$ and $B_\ell^{(m)}$ represent polarization with electric $(1)^\ell$ and magnetic $(1)^{\ell+1}$ type parities respectively, moreover, $B_\ell^{(m)}$ and $E_\ell^{(m)}$ represent polarization with Q and U interchanged, therefore, they are polarization patterns rotated by 45°.
The power spectra of temperature anisotropies today are defined as $C_\ell^{\Theta\Theta} \equiv \langle |a_{\ell m}|^2 \rangle$ for $\Theta = \sum a_{\ell m}Y_\ell^m$ with the average being over the $(2\ell+1)$ m-values, similarly we can generalize (2.12) as

$$(2\ell+1)^2 C_\ell^{XY} = \frac{2}{\pi}\int \frac{dk}{k}\sum_{m=-2}^{2} k^3\ X_\ell^{(m)*}(k)\ Y_\ell^{(m)}(k) \tag{2.35}$$

with X, $Y = \Theta$, E, B.
Note that, by parity property (2.23), $C_\ell^{\Theta B}$ and C_ℓ^{EB} are zero.

2.3 CMB Radiation Transport

In the previous section we have showed the mathematical tools to describe temperature and polarization of the CMB, we can finally employ this techniques to obtain a simple derivation and form of the *Radiation Transport* equation. It is the Boltzmann equation which describe the transport of photons under Thomson scattering with electrons and, at the end, show how CMB temperature fluctuation and polarization arise from primordial perturbations.

Thomson Scattering
The Thomson scattering is the elastic scattering of radiation by a charged particle, it is the low-energy limit of Compton scattering, indeed, the kinetic energy of the particle and the photon frequency are conserved.
Considering an incoming radiation hitting an electron from the left and from the top (Figure 2.3), it will be scattered by 90° out of the page. If the incoming radiations have equal intensity, the resulting radiation is unpolarized, instead, if the two intensity are not the same, namely the radiation varies at 90°, the scattered radiation is linear polarized.
In other words, the incident unpolarized light shakes the electrons, then, this shaking re-radiates the outgoing reflected light and the final radiation will be polarized only if the initial photon distribution has a *quadrupole* pattern.

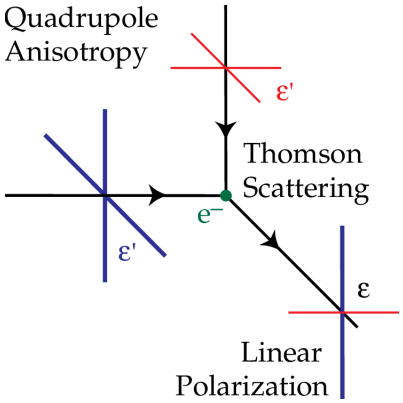

Figure 2.3: Polarization of radiation by Thomson Scattering. [7]

This last statement is simple proved. First, consider the differential cross section of the Thomson scattering for an incident wave with linear polarization $\hat{\epsilon}'$, into a scattered wave with linear polarization $\hat{\epsilon}$

$$\frac{d\sigma}{d\Omega} = \frac{3\sigma_T}{8\pi}|\hat{\epsilon}' \cdot \hat{\epsilon}|^2. \tag{2.36}$$

Second, consider the decomposition in spherical harmonics of the intensity of the incoming radiation in a frame in which: $\hat{x}$-$\hat{z}$ is in the scattering plane, the line of sight is the $\hat{z}$ direction and Q and U are measured with respect to the x and y axes

$$I'(\theta, \phi) = \sum_{lm} a_{lm} Y_{lm}(\theta, \phi). \tag{2.37}$$

Performing the full computation [4], we end up with the Stokes parameters related to the scattered radiation

$$\begin{aligned} I &= \frac{3\sigma_T}{16\pi}\left[\frac{8}{3}\sqrt{\pi}\ a_{00} + \frac{4}{3}\sqrt{\frac{\pi}{5}}\ a_{20}\right] \\ Q &= \frac{3\sigma_T}{4\pi}\sqrt{\frac{2\pi}{15}}\text{Re}\ a_{22} \\ U &= -\frac{3\sigma_T}{4\pi}\sqrt{\frac{2\pi}{15}}\text{Im}\ a_{22} \end{aligned} \tag{2.38}$$

where a_{22} is the coefficient of the spherical harmonic $Y_{22}(\theta, \phi)$ i.e. the radiation quadrupole moment incident on the electron.
The magnitude and orientation of the polarization of the scattered radiation is proportional, respectively, to the magnitude and orientation of the *quadrupole* of the incident radiation. In terms of a multipole decomposition into spherical harmonics presented in the previous section, the five quadrupole moments are represented by $Y_\ell^m(\theta, \phi)$ with $\ell = 2$ and $m = 0, \pm 1, \pm 2$.

Perturbations

The problem of understanding the polarization pattern of the CMB, translates into understanding the quadrupolar temperature fluctuations at last scattering. If we assume that at the end of inflation the Universe is at first order isotropically filled with radiation, thermal fluctuations are only produced by primordial perturbations which act as sources. [7]
We have seen how these source terms can be geometrically distinguishable:

- *Scalar* perturbations, or compression-like, are perturbations in the energy density of the cosmological fluid. This source lead to potential fluctuations that will dominate at large scales and will generate photons bulk flows, or dipole anisotropies, from hot to cold temperature regions, respectively called crests and troughs. The quadrupole pattern has an $m = 0$ structure and is described by a local quadrupole modulated by a plane wave in space $-Y_2^0(\hat{n}) \exp(i\vec{k} \cdot \vec{x})$.

- *Vector* perturbations are vortical motions of the matter, there are not associated density perturbations. In general, the vorticity is not enhanced by gravity, thus, it is damped by the expansion of the Universe. The quadrupole pattern has an $m = 1$ structure and is described by $-iY_2^{\pm 1}(\hat{n}) \exp(i\vec{k} \cdot \vec{x})$ component.

- *Tensor* fluctuations are transverse-traceless perturbations to the metric, they are actually plane gravitational waves, representing a quadrupolar stretching of space in the plane of the perturbation.
  The wavelength stretching of photons produces a quadrupolar temperature variation with an $m = \pm 2$ pattern.

Note that in the previous chapter we did not mentioned vector perturbations, but we do here just for geometrical completeness. From now on, we will not consider them because, as already anticipate, they are damped by the Universe expansion, moreover, Thomson scattering does not produce vector fluctuations, so we do not expect to see them in the CMB.

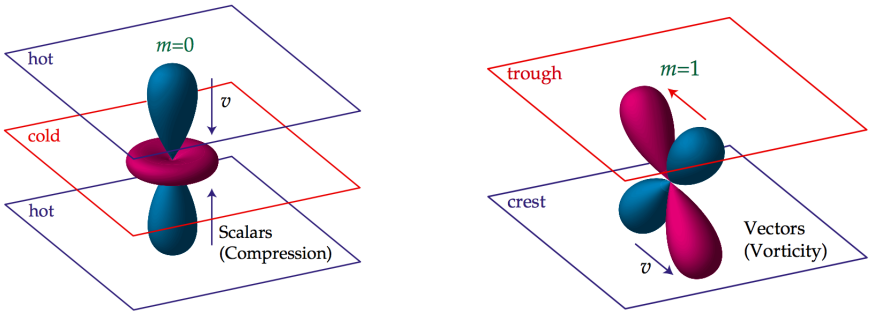

Figure 2.4: Left: Scalar quadrupole moment ($l = 2, m = 0$): flows from hot into cold regions. Right: Vector quadrupole moment ($l = 2, m = 1$): the Doppler effect generates a quadrupole pattern with lobes 45°. [7]

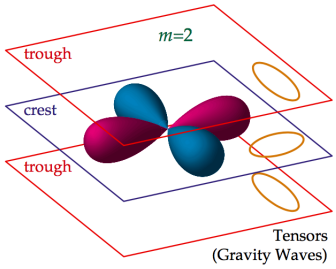

Figure 2.5: Tensor quadrupole moment ($l = 2, m = 2$): gravity waves distort space in the plane of the perturbation, changing a circle of test particles into an ellipse. [7]

Boltzmann Equation

With all the ingredients presented so far, we can show a simple derivation and form of the Radiation Transport of the CMB, including polarization. [8]
For our purposes, it is convenient to describe the polarization in temperature fluctuation units, in particular we define the matrix

$$\mathbf{T} = (\mathbf{I}\Theta + V\sigma_2 + (Q + iU)\mathbf{M}_+ + (Q - iU)\mathbf{M}_- \tag{2.39}$$

where $\Theta = \Delta T/T$ is the temperature perturbation summed over polarization states, Q, U and V are the usual Stokes parameters and, we recall, $\mathbf{M}_\pm = (\sigma_3 \pm i\sigma_1)/2$ (2.18). This form is very convenient because under rotation $Q \pm iU$ transforms into itself and, as we showed in (2.34), $Q \pm iU$ can be decomposed into spin-(± 2) harmonics (2.16). Again, we neglect V term, so we express (2.39) with a simpler vector

$$\mathbf{T} = (\Theta, Q + iU, Q - iU). \tag{2.40}$$

The Radiation Transport equation is nothing but the Boltzmann equation which describes the evolution of $\mathbf{T}$ under the Thomson scattering term and gravitational redshift

$$\frac{D}{D\eta}\mathbf{T}\ (\eta, \vec{x}, \hat{n}) = \frac{\partial}{\partial\eta}\mathbf{T} + n^i\nabla_i\mathbf{T}\ =\ \mathbf{C}[\mathbf{T}] + \mathbf{G}[h_{\mu\nu}] \tag{2.41}$$

η is the conformal time, $(\vec{x}, \hat{n})$ represent position and direction, and at the right hand side $\mathbf{C}$ is the Thomson collision term, which is functional of $\mathbf{T}$ itself and $\mathbf{G}$ represents the gravitational effects in a perturbed metric $h_{\mu\nu}$.
The analytic expression of the Thomson scattering, including polarization, was first performed by Chandrasekhar [4], here we report the final result

$$\mathbf{C}[\mathbf{T}] = -\dot{\tau}\mathbf{I}(\Omega) + \frac{1}{10}\dot{\tau}\int d\Omega' \sum_{m=-2}^{2} \mathbf{P}^{(m)}(\Omega, \Omega')\ \mathbf{T}(\Omega') \tag{2.42}$$

the differential optical depth $\dot{\tau} = n_e\sigma_T a$ is simply the collision rate in conformal time and $\mathbf{I}(\Omega)$ is a vector which describes the isotropization of distribution in the electron rest frame. The matrix $\mathbf{P}^{(m)}(\Omega, \Omega')$ accounts for the anisotropic nature of Thomson scattering

$$\mathbf{P}^{(m)} = \begin{pmatrix} Y_2^{m'}\ Y_2^m & -\sqrt{\frac{3}{2}}\ {}_2Y_2^{m'}\ Y_2^m & -\sqrt{\frac{3}{2}}\ {}_{-2}Y_2^{m'}\ Y_2^m \\ -\sqrt{6}\ Y_2^{m'}\ {}_2Y_2^m & 3\ {}_2Y_2^{m'}\ Y_2^m & 3\ {}_{-2}Y_2^{m'}\ {}_2Y_2^m \\ -\sqrt{6}\ Y_2^{m'}\ {}_{-2}Y_2^m & 3\ {}_2Y_2^{m'}\ {}_{-2}Y_2^m & 3\ {}_{-2}Y_2^{m'}\ {}_{-2}Y_2^m \end{pmatrix} \tag{2.43}$$

the presence of just Y_2 and ${}_{\pm 2}Y_2$ terms shows, again, how polarization is generated through quadrupole anisotropies.
The Gravitational redshift in (2.41) is

$$\mathbf{G}[h_{\mu\nu}] = \left(\frac{1}{2}n^i n^j \dot{h}_{ij} + n^i \dot{h}_{0i} + \frac{1}{2}n^i \nabla_i h_{00}\,, 0\,, 0\right) \tag{2.44}$$

the first component, the first term is due to stretching of the expanding spatial metric, the second is the frame dragging and the third terms is due to time dilation effects.
It is important to emphasize that when radiation free streams, photons from different regions and temperature intersect, these gradients in the distribution produce anisotropies. the free stream effect becomes more evident when the gradient term in (2.41) is evaluate in Fourier space

$$\hat{n}\cdot\vec{\nabla}\mathbf{T} \;\longrightarrow\; i\hat{n}\cdot\vec{k}\;\mathbf{T} = i\sqrt{\frac{4\pi}{3}}k\;Y_1^0\;\mathbf{T} \;\longrightarrow\; \sqrt{\frac{4\pi}{3}}Y_1^0({}_sY_\ell^m) \tag{2.45}$$

recall that we can always expand $\mathbf{T}$ in terms of Y_ℓ^m and ${}_{\pm 2}Y_\ell^m$.
The free stream term can be evaluate involving again the Clebsch-Gordan relation (2.25) which couples the ℓ to $\ell+1$ moments of the distribution. Thus, we expect as result of the free streaming an infinite herarchy of coupled ℓ moments that passes power from sources at low multipoles up to the ℓ-chain.

Solutions
Finally, we can write the explicit form of the Boltzmann equation (2.41) for temperature which meanly arises from the Clebsch-Gordan relation

$$\dot{\Theta}_\ell^{(m)} = k\left[\frac{{}_0c_\ell^m}{(2\ell-1)}\Theta_{\ell-1}^{(m)} - \frac{{}_0c_{\ell+1}^m}{(2\ell+3)}\Theta_{\ell+1}^{(m)}\right] - \dot{\tau}\Theta_\ell^{(m)} + S_\ell^{(m)}. \tag{2.46}$$

The term in the square brackets is the effect of the free streaming which is telling us that, in absence of scattering, power is transferred to the ℓ-modes hierarchy. The term $\dot{\tau}\Theta_\ell$ is the mean effect of the scattering and S_ℓ is a source term which accounts for gravitational and residual scattering effects.
Similarly, we can write the explicit Boltzmann equations for the polarization recalling the definitions (2.34), for $(\ell \geq 2, m \geq 0)$

$$\begin{aligned}
\dot{E}_\ell^{(m)} &= k\left[\frac{-2c_\ell^m}{(2\ell-1)}E_{\ell-1}^{(m)} - \frac{2m}{\ell(\ell+1)}B_\ell^{(m)} - \frac{{}_2c_{\ell+1}^m}{(2\ell+3)}E_{\ell+1}^{(m)}\right] - \dot{\tau}[E_\ell^{(m)} + \sqrt{6}P^{(m)}\delta_{\ell,2}] \\
\dot{B}_\ell^{(m)} &= k\left[\frac{{}_2c_\ell^m}{(2\ell-1)}B_{\ell-1}^{(m)} + \frac{2m}{\ell(\ell+1)}E_\ell^{(m)} - \frac{{}_2c_{\ell+1}^m}{(2\ell+3)}B_{\ell+1}^{(m)}\right] - \dot{\tau}B_\ell^{(m)}
\end{aligned} \tag{2.47}$$

where the scattering term

$$P^{(m)} = \frac{1}{10}\left[\Theta_2^{(m)} - \sqrt{6}E_2^{(m)}\right] \tag{2.48}$$

only involves the quadrupole moments of the temperature and E-polarization distribution.
Notice as the polarization source $P^{(m)}$ in (2.47) does not enters as source on the B-mode quadrupole because of the opposite parity of Θ_2 and B_2, which is telling us how

Thomson scattering can only produce E-mode locally, B-mode cannot be generated by scattering, it arises from the photons free streaming.

The Boltzmann equation for temperature (2.46) has a formal integral solution that arises considering the properties of source projections and the angular decomposition of G_ℓ^m (2.31)

$$\frac{\Theta_\ell^{(m)}(\eta_0,k)}{2\ell+1} = \int_0^{\eta_0} d\eta\; e^{-\tau} \sum_{\ell'}\; S_{\ell'}^{(m)}(\eta)\; j_\ell^{(\ell' m)}(k(\eta_0-\eta)). \tag{2.49}$$

Similarly, from the radial decomposition of the source

$$-\sqrt{6}\dot{\tau}\; P^{(m)}\; [{}_2G_2^m \mathbf{M}_+ + {}_{-2}G_2^m \mathbf{M}_-] \tag{2.50}$$

and the radial decomposition of ${}_{\pm 2}G_\ell^m$ (2.31), for the polarization we have

$$\begin{aligned} \frac{E_\ell^{(m)}(\eta_0,k)}{2\ell+1} &= -\sqrt{6}\int_0^{\eta_0} d\eta\; \dot{\tau}e^{-\tau}\; P^{(m)}(\eta)\; \epsilon_\ell^{(m)}(k(\eta_0-\eta)) \\ \frac{B_\ell^{(m)}(\eta_0,k)}{2\ell+1} &= -\sqrt{6}\int_0^{\eta_0} d\eta\; \dot{\tau}e^{-\tau}\; P^{(m)}(\eta)\; \beta_\ell^{(m)}(k(\eta_0-\eta)). \end{aligned} \tag{2.51}$$

The temperature Θ_ℓ and the polarization modes E_ℓ and B_ℓ are tightly related to the behaviors of the functions j_ℓ, ϵ_ℓ and β_ℓ respectively. Therefore, from the properties of these, we learn that sources with different geometrical nature: scalar, vector and tensor, generate different amount of E and B mode.

E-mode and B-mode conclusions

In this section, we have learned some very important lessons, first of all that Scalar and Tensor primordial fluctuations may have both generated the CMB polarization. Thomson scattering only produced local $\ell = 2$ E-mode since the spherical harmonics that describe the temperature anisotropy have $(1)^\ell$ electric parity. However, this local signature from scattering is modulated over the last scattering surface by the plane wave spatial dependence of the perturbation, generating B-mode pattern.
We have seen that: (i) for tensor perturbations, Q and U components of the local pattern are comparable, this lead to a comparable distribution of E and B modes; (ii) for scalars, the modulation is of a pure Q-field and thus its E-mode nature is preserved, with not generation of B-modes; (iii) for vectors, U-mode dominates the pattern and generate mainly B-modes.
The reason of these defferences is that the angular momentum summation takes the $\ell = 2$ local angular dependence to higher ℓ and splits the signal into E and B components which ratio is related to Clebsch-Gordan coefficients. At short wavelengths, we expect

	scalar	vector	tensor
B/E	0	6	8/13

These statements are independent of the dynamics and underlying spectrum of the perturbations themselves.

All these results are suggesting that, in principal, the detection of the CMB B-mode is the ultimate evidence of the presence of primordial Tensor modes, which is one of the fundamental prediction of the Inflation theory.

Therefore, the detection of primordial CMB B-mode is one of the most challenging Cosmological actual experimental objective.

Chapter 3

CMB Experiments and the QUIJOTE Project

Observational cosmology is the study of the evolution and the structure of the Universe through observation, using instruments such as telescopes and cosmic ray detectors. In the following chapter, we go back through history, from first instruments to the latest results obtained with the *Planck* collaboration. In conclusion, we will present the *QUIJOTE* CMB Experiment and the future of CMB polarization observation.

3.1 Experimental Legacy

Since the first detection in 1964, there have been designed and built several experiments with the aim of measure the CMB anisotropies and polarization, including: ground-based, balloon-based and space-based receivers.

Detection History
Here, we report a list of some very important experiments:

- *COBE*, Cosmic Background Explore: it was a satellite developed by NASA and launched in 1989 and operated till 1993. It carried three instruments: Diffuse Infrared Background Experiment, or *DIRBE*, to search for the cosmic infrared background radiation, Differential Microwave Radiometer, or *DMR* to map the cosmic radiation sensitively and Far Infrared Absolute Spectrophotometer, or *FIRAS* to compare the spectrum of the cosmic microwave background radiation with a precise black body.
  The FIRAS results showed a perfect fit of the CMB and the theoretical curve for a black body at $T = 2.725\,\mathrm{K}$ and with DMR results they managed to generate first full sky maps of the CMB anisotropy by subtracting out galactic emissions and dipole. [9]

- *DASI*, Degree Angular Scale Interferometer: it was a compact interferometer built in 1999-2000 at the South Pole. The DASI was made up of 13 small telescope elements, each carrying a corrugated horn working at the frequencies 26–36 GHz, in 2001 the telescope was reconfigured with achromatic polarizers.
  The DASI team discovered the second and third acoustic peaks in the CMB's

power spectrum, the fist had been discovered by earlier experiments, moreover, in 2002, the DASI team reported the first detection of polarization anisotropies in the CMB. [10]

- *CBI*, Cosmic Background Imager: a 13-element interferometer installed at Llano de Chajnantor Observatory in the Chilean Andes. It operated from 1999 till 2008, conducting high-resolution measurements, about 6 amin, at frequency range 26–36 GHz.
  It obtaining the first detailed E-mode polarization spectrum of the CMB. [11]

- *WMAP*, Wilkinson Microwave Anisotropy Probe: a NASA spacecraft launched in 2001 and operational until 2008. It was 45 times more sensitive of its COBE satellite predecessor, about 13.2 amin beam, and operate in five radio frequency bands, from 23 GHz to 94 GHz.
  The WMAP results have played a fundamental role in establishing the accepted standard cosmological model and in refining important cosmological parameter. It marked the beginning of the era of "precision cosmology". [12]

- *Plank*: it was a European Space Agency (ESA) spacecraft operated from 2009 to 2013, improving and extending its predecessor WMAPâs results. It carried two instruments: the Low Frequency Instrument, or LFI, observing at 30, 44 and 70 GHz, and the High Frequency Instrument, or HFI, observing at 100, 143, 217, 353, 545 and 857 GHz, with resolution up to 5 amin. [13]

Legacy of Planck

The Planck experiment provided the strongest constraints on the parameters of the standard 6-parameter Λ-CDM cosmological model (Table 3.1). In Figure 3.1 the TT, TE, and EE spectra are plotted with the best-fit base-ΛCDM theoretical spectrum fitted to the combined temperature and polarization.
Note as the spectrum is expressed in terms of the quantity

$$\mathcal{D}_\ell^{XY} = \frac{\ell(\ell+1)C_\ell^{XY}}{2\pi} \tag{3.1}$$

which is called angular power spectrum.
Planck has determined the angular power spectrum of the temperature anisotropies to very-high and ultimate precision across all of the relevant scales.
From Figure 3.1 we clearly see some fundamental features of our Universe: the fundamental mode is at $\ell \sim 220$ which reveals a flat Universe and that the size of the horizon at recombination is today $\sim 1^\circ$ on the sky. The secondary peaks reveal the underlying physics of oscillating sound waves in the coupled photon-baryon fluid, driven by gravitational potential perturbations. At high ℓ's, i.e. a very small physical scales, we see an exponential dumping due to the photon diffusion which wash out fluctuations. Instead, at $\ell \leq 50$ the spectrum could be in principle a direct measure of the primordial fluctuation, but an important consideration should be taken in account: the cosmic variance.
It is important to mention that an analysis of all data taken by the *BICEP2/Keck* CMB polarization experiments combined with *WMAP* and *Planck* data yields the actual most stringent constraint on the tensor-to-scalar ratio: $r_{0.05} < 0.07$ at 95 % confidence. [14]

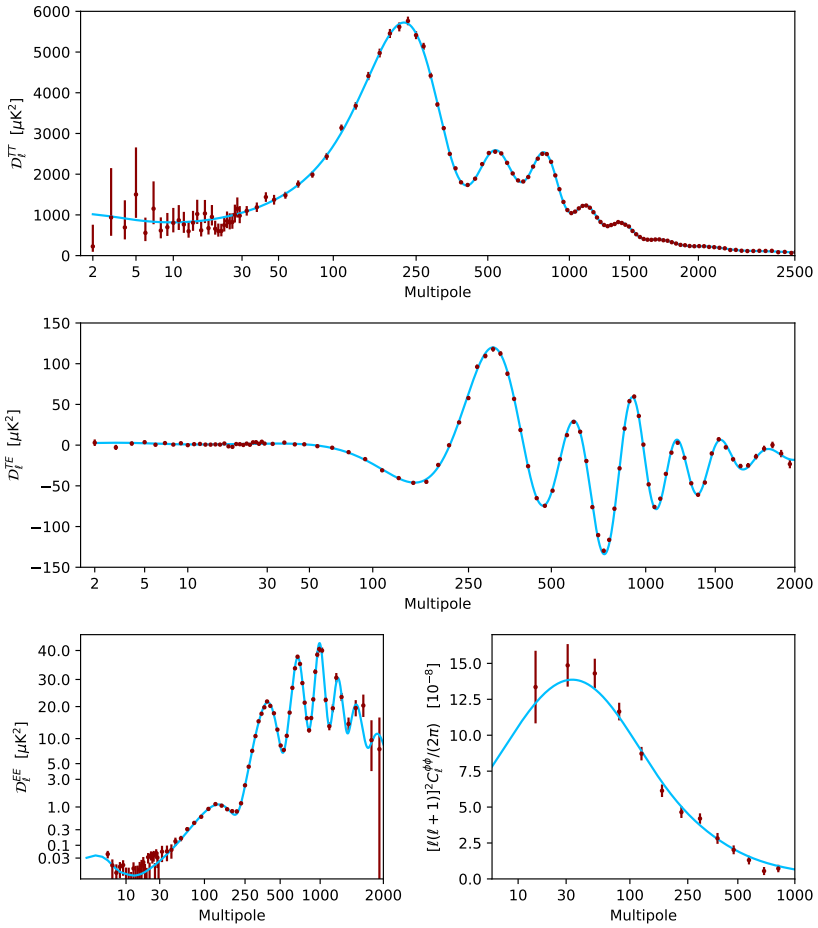

Figure 3.1: CMB foreground-subtracted and frequency-averaged power spectra for: temperature (top), the temperature-polarization cross-spectrum (middle), the E mode of polarization (bottom left) and the lensing potential (bottom right). [13]

	Planck	*Planck* + *BAO*
$\Omega_{\rm b}h^2$	0.022383	0.022447
$\Omega_{\rm c}h^2$	0.12011	0.11923
$n_{\rm s}$	0.96605	0.96824
H_0 $[km/sMpc]$	67.32	67.70
Ω_Λ	0.6842	0.6894
$\Omega_{\rm m}$	0.3158	0.3106
$\Omega_{\rm m}h^2$	0.1431	0.1424
$z_{\rm re}$	7.68	7.90
Age [Gyr]	13.7971	13.7839

Table 3.1: The 6-parameter Λ-CDM model that best fits the combination of data from *Planck* CMB temperature and polarization power spectra, with and without *BAO*, baryon acoustic oscillations, data. [13]

Cosmic Variance

When a comparison between theoretical predictions and observations is performed, it is important to keep in mind that the CMB anisotropies resulting from inflation are stochastic, because of the quantum nature of the process by which they are generated. Therefore, only observations over an ensemble of different configurations of the Universe could allow the unambiguous measurement of fundamental microphysical parameters. However, we are constrained to observe only one configuration, so, it remains an irremovable uncertainty, which we call *cosmic variance*, no matter how precise we measure CMB anisotropy.

In formulas, because of isotropy and ergodicity, we can approximately relate angular power spectrum and harmonic coefficients as

$$C_\ell = \left\langle |a_{\ell m}(\mathbf{r})|^2 \right\rangle = \left\langle \frac{\sum_m |a_{\ell m}(\mathbf{r})|^2}{2\ell+1} \right\rangle_{space} \simeq \frac{\sum_m |a_{\ell m}(\mathbf{r})|^2}{2\ell+1} = \tilde{C}_\ell \tag{3.2}$$

what we measure, from a single realization of the Universe, is the quantity $\tilde{C}_\ell$, which is simple an approximation of C_ℓ. The error we make considering this approximation is the variance

$$\begin{aligned} var(\tilde{C}_\ell) &= \frac{1}{(2\ell+1)^2} \sum_m var(|a_{\ell m}(\mathbf{r})|^2) \\ &= \frac{1}{(2\ell+1)^2} \sum_m \left[\left\langle |a_{\ell m}(\mathbf{r})|^4 \right\rangle - \left\langle |a_{\ell m}(\mathbf{r})|^2 \right\rangle^2 \right] \\ &= \frac{1}{(2\ell+1)^2} \sum_m 2\ C_\ell^2 = \frac{2}{2\ell+1} C_\ell^2 \end{aligned} \tag{3.3}$$

where, in the first line we used the fact that the $a_{\ell m}$ coefficients are uncorrelated and that $\left\langle |a_{\ell m}(\mathbf{r})|^4 \right\rangle = 3 \left\langle |a_{\ell m}(\mathbf{r})|^2 \right\rangle^2$ according the Wick's theorem. The dependence from ℓ suggests that the cosmic variance decreases with ℓ, indeed, the observation of the CMB spectra in Figure 3.1 at low ℓ are largely affected by the cosmic variance, which represent a unseasonable uncertainty.

3.2 CMB Foregrounds

The CMB is the most distant source of radiation, therefore, it is a backlight to all other sources of radiation between the surface of last scattering and the observer.

Those sources of contamination are known as *CMB foregrounds*.

When CMB measures in intensity and polarization are performed, foregrounds must be removed, thus, it is required a prior knowledge of: intensity and polarization maps, statistical spatial fluctuations, and principally, spectral information about all the contamination sources. [15]

Table 3.2 shows the most common types of foregrounds, their impact on the CMB polarization and on the angular scale. In general, only a few astrophysical foregrounds are significantly polarized, but their relative importance compared to CMB fluctuations is large.

In Figure 3.2 are shown the *Planck* temperature maps from 30 GHz to 857 GHz, the foregrounds are clearly visible in all the frequencies, especially in the Galactic region, and dominate at lowest and highest frequencies. Figure 5.3 shows the Planck spectra

of important foregrounds, both in temperature and polarization, we clearly distinguish four foregrounds in temperature and two in polarization, which represent the main components.
In the following, we will discuss about the most important Galactic foregrounds.

Foreground	Polarization	Angular scales
Atmosphere	$\approx 0\,\%$	Large
Ground	Varies	Large
Radio Freq. Interference (RFI)	$0 - 100\,\%$	All
Sun/Moon	Low	All
Planets/solar system objects	Low	Small
Zodiacal light	Low	Large scales
Galactic synchrotron radiation	$\approx 10 - 40\,\%$	Large
Galactic free-free radiation	Low	Large
Galactic thermal dust radiation	$\approx 2 - 20\,\%$	Large
Galactic spinning dust radiation	Low	Large
Galactic magnetic dust radiation	$0 - 35\,\%$	Large
Galactic line emission (e.g. CO)	Low	Large
Radio galaxies	Few	Small
Sub-mm/IR galaxies	Low	Small
Infrared Background (CIB)	Low	Small/interm.
Secondary Anisotropies	Low	All

Table 3.2: Examples of the various types of CMB foregrounds. 'Low' polarization typically means $< 1\,\%$. [15]

Synchrotron radiation
When relativistic charged particles are accelerated radially, they emit an electromagnetic radiation which is called Synchrotron radiation, or magnetobremsstrahlung radiation. In an astrophysical context, the particles are the Cosmic Ray electrons which are accelerated by the Galactic magnetic field.
The radiated energy depends on number and energy of the CR and strength of the Galactic field, the spectrum depends directly on the CR electrons energy spectrum which is well-approximated by a power-law. The spectrum is steeply falling with frequency, the spectral index is about $\beta \sim 2,7$ at few GHz and it is even stepper at higher frequencies because of radiative losses, at *Planck* frequencies the spectral index is about $\beta \sim 3.0$.
The polarization properties of the Galactic Synchrotron radiation are not well-known. In general, it becomes important at frequencies above a few GHz. Moreover, the precise values of polarized fractions are difficult to quantify because of the presence of free-free and anomalous microwave emission in total intensity at few GHz. Nevertheless, Synchrotron emission is expected to be polarized at a level of 10-40 %.

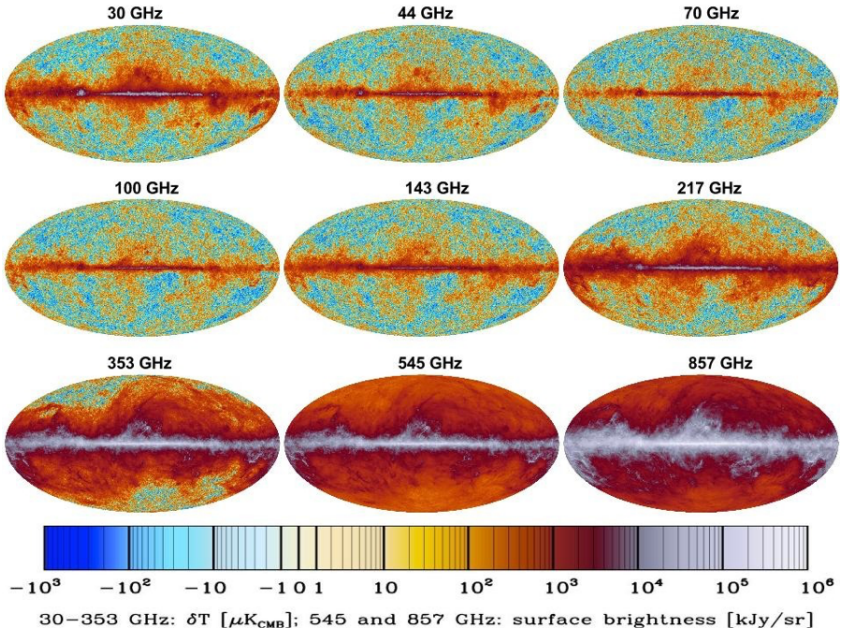

Figure 3.2: Planck temperature maps, covering frequencies from 30 GHz to 857 GHz. [16]

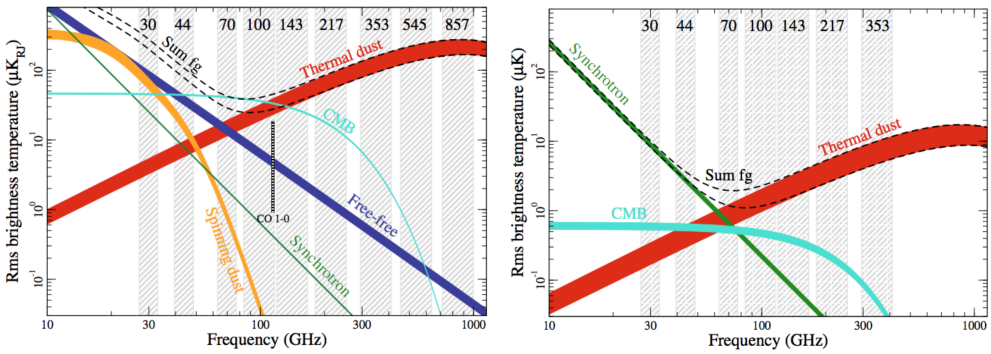

Figure 3.3: Spectral characteristics of foregrounds and CMB in temperature (left) and polarization (right). [16]

Free-free radiation
Bremsstrahlung, i.e. 'deceleration radiation', or free-free radiation, is the electromagnetic radiation emitted by the deceleration of a charged particle when deflected by another charged particle. In our case, it is produced by free electrons interacting with ionized gases.
Bremsstrahlung has a well-known continuous spectrum. As the change of the energy of the decelerated particles increases, it becomes more intense and whose peak intensity shifts toward higher frequencies. At frequencies of few GHz, the spectrum has a temperature spectral index of $\beta \sim -2.1$, and it becomes slightly steeper at higher frequencies, about $\beta \sim -2.13$ approaching 100 GHz. According to Figure 5.3, because of its spectral nature, free-free radiation is the dominant foreground around the foreground minimum ~ 70 GHz.
Coulomb interactions have random orientations, with no significant alignment with the magnetic field, therefore, the free-free radiation is expected to be unpolarized. A small residual contribution can arise on sharp edges due to Thomson scattering. At high Galactic latitudes, the measured polarization free-free contribution is expect to be less than 1-3%, therefore, it is usually not considered in CMB polarization studies.

Thermal dust radiation
Thermal radiation is electromagnetic radiation produced by the thermal motion of particles, in this case interstellar dust grains with temperature $T_d \sim 20\,\mathrm{K}$.
Its emission law can be described by a black body emission modified by opacity effects

$$T(\nu) = \tau \nu^{\beta_d} B(\nu, T_d)$$

where $B(\nu, T_d)$ is the conventional black body spectrum, the term ν^{β} represents the dependence of the grains emissivity on wavelength and so $\beta_d \in [1, 2]$ is the emissivity index. *Planck* data are reasonably well-modelled by this single modified black body spectrum with $T_d \simeq 19\,\mathrm{K}$ and $\beta_d \simeq 1.6$ [13].
Elongated dust grains emit principally along their shortest axes while large dust grains can align efficiently by the Galactic magnetic field, these effects generate a net significant polarization. *Planck* data analysis have suggest dust polarization fractions up to 20 %.
The power spectrum of thermal dust anisotropies appears to follow a power-law with a slope $\alpha \sim -0.4$, leading to larger fluctuations on large angular scales [13].

Spinning dust radiation
Small interstellar dust grains and molecules can rotate at GHz frequencies, and if they happen to have an electric dipole moment, they emit by electric dipole radiation. The spectrum is not well-understood, but from the previous description, it is expected to be highly peaked, some Galactic clouds spectra analysis show a peak at frequency $\sim 30\,\mathrm{GHz}$.
Theory predicts that spinning dust radiation is slightly polarized at few GHz, at level of few per cent, this argument support the thesis that *Anomalous Microwave Emission*, or AME, is due to spinning dust.
AME has been observed by a range of experiments and in a variety of environments at frequencies in the range 10-60 GHz, it cannot be simply explained by Synchrotron or free-free emission mechanisms, indeed, the most natural explanation is spinning dust. As anticipated, AME appears to be very weakly polarized, latest observational constraints show a polarization fraction of less than 1%, therefore, may be neglect for future CMB polarization studies. Nevertheless, even a small amount of AME po-

larization could be problematic for component separation with future ultra-high sensitivity data that aim to constrain the tensor-to-scalar ratio at very low level, $r \leq 10^{-3}$.

3.3 The QUIJOTE Experiment

The *QUIJOTE* (*Q-U-I JOint TEnerife*) experiment is a collaboration between the Instituto de Astrofisica de Canarias (IAC), the Instituto de Fisica de Cantabria (IFCA), DICOM company and Universities of Cantabria, Cambridge and Manchester. [17, 18]
The experiment is located at *Izaña*, in the Tenerife island, Spain, at an altitude of 2400 m over the sea level at longitude, latitude position 28.3° N, 16.5° W. Previous experiments hosted in this site, proved that the atmospheric conditions are optimal for CMB observations in the microwave range.
The experiment consists of two telescopes, both telescopes are altazimuth-mount type composed of a parabolic mirror as primary, aperture of 2.25 m, and hyperbolic mirror as secondary, aperture of 1.89 m, they are disposed in an offset Gregorian Dracon scheme, which provides optimal cross-polarization properties and symmetric beams. Each telescope is mounted on its own platform that can rotate around the azimuth axis at a maximum frequency of 36 deg/s and can point at a minimum elevation of 30°.
The telescopes enclosure and the building hosting the control room were finished in June 2009. The development of the project includes two phases: in the first phase the first *QUIJOTE* telescope (*QT1*) was installed in November 2012 and has been operating for almost 7 years now, in the current and second phase the second telescope (*QT2*) that was installed on July 2014 has been tested and is operational.
Each telescope is mounted on its own platform that can rotate around the azimuth axis at a maximum frequency of 36 deg/s.

Figure 3.4: QUIJOTE Telescopes

The Instruments

The *QUIJOTE* experiment consists of three instruments: the Multi-Frequency Instrument or *MFI*, mounted on the *QT1*, the Thirty-Gigahertz Instrument, or *TGI*, and Forty-Gigahertz Instrument, or *FGI*, both mounted on the *QT2*.

- *Multi-Frequency Instrument (MFI)*
  The first QUIJOTE instrument is a multichannel instrument providing the frequency coverage between 10 and 20 GHz, in particular, it is operating in four frequency bands centred at 11.2, 12.9, 16.7 and 18.7 GHz.
  It consists of four conical corrugated feedhorns, designed by the University of Manchester, each of which feeds a novel cryogenic on-axis rotating polar modulator. Two of them operate in the frequency range 10-14 GHz and the other two operate in the frequency range 16-20 GHz. Each horn has four channels operating at one of the two frequencies and their combinations permits to recover the I, Q and U Stokes parameters at each frequency.

- *Thirty-Gigahertz Instrument (TGI)*
  The second QUIJOTE instrument consists of 31 polarimeters operating at 30 GHz with a 8 GHz bandwidth, each of them is made of 4 channels providing data to the acquisition system. At this commission phase, only four pixels are operational. Unlike the *MFI*, the *TGI* polarization modulation does not rely in the mechanical movement of polar modulators, it employs a fixed polariser with the combination of two phase-switches, generating four polarisation states. This configuration has the advantage that it does not involve movement of mechanical parts and provide directly the Stokes parameters I, Q and U as output, about this argument we will provide further information in next chapters.

- *Forty-Gigahertz Instrument (FGI)*
  The third QUIJOTE instrument will consist of 31 polarimeters working at 42 GHz, with a 12 GHz bandwidth. At this commission phase, only three pixels are operational. The *FGI* has a design similar to the one of the *TGI* and shares a common cryostat with this, indeed, the *QT2* acquisition system has been designed to be operational with the two type of pixels.

	MFI	TGI	FGI
Nominal Frequency [GHz]	11-19	30	42
Bandwidth [GHz]	2	8	12
Number of horns	8	31	31
Channels per horn	4	4	4
Beam FWHM [°]	0.60-0.92	0.37	0.28
T_{sys} [K]	25	35	45
Sensitivity [Jy s$^{1/2}$]	0.30-0.42	0.065	0.074

Table 3.3: Nominal characteristics of the three QUIJOTE instruments.

Scientific goals

The *QUIJOTE* Experiment has been design to achieve two primary scientific goals:

- CMB B-mode polarization detection and tensor-to-scalar ratio constrain down to $r = 0.05$
- Provide detailed information of the CMB Galactic foregrounds polarization at low frequencies, mainly: Synchrotron emission and the Anomalous Microwave Emission.

QUIJOTE is expected to conduct two large surveys in polarization: a shallow *Galactic survey*, with the goal of reaching final sensitivities of 25 μK, 4 μK and 6 μK per beam respectively for the three instruments, and a deep *Cosmological survey*, with the goal of reaching final sensitivities of 5 μK per beam for the first instrument, and 1 μK per beam for the other two.

- The wide survey is part of the Radioforeground Project [19]. One of the MFI aim is to characterize some properties of the Synchrotron emission: the large scale magnetic field, spectral index, curvature of the index and polarization properties, and some properties of AME. This information will constitute a unique low frequency complement to the maps delivered by *Planck*, moreover, they would be particularly useful for future sub-orbital or satellite CMB experiments which work at same or higher frequencies.

- The deep Cosmological survey, covering a sky area of 3000 deg^2, is obtained with raster scan mode toward three fields dedicated to cosmology. Given the expected nominal sensitivities, a constrain on the tensor-to-scalar ratio of r = 0.1 (at 95 % C.L.) should be obtained after one effective year of observations with the *TGI*. The final sensitivity of $r = 0.05$ (at 95 % C.L.) will be obtained with combined of three and two effective years of observations with, respectively, the *TGI* and the *FGI*.

In addition, *QUIJOTE* is also dedicated to the observations of specific sky regions of Cosmological interest with the aim of characterizing their emission, including: Galactic region as the Fan region, a region toward which a not well-known large uniform magnetic field is present, a series of molecular clouds that are sources of high AME emissivity, such as Taurus, Perseus, W43 and W47, and finally Super Novae Remnants (SNRs), for instance W44, W51, IC443 and W63.

First Scientific Results

The first maps released by the *QUIJOTE* collaboration confirmed the potential of this experiment to get precise measurements of the CMB polarisation and of the diffuse low-frequency foregrounds, reaching sensitivities between 30 and 80 μK per beam, in both Q and U. [20, 21]

The first results obtained with the *QUIJOTE* experiment in 2014 were based on AME analysis of observations of the Perseus molecular complex. Observations of two molecular complexes, W43 and W47, and one Supernova Remnant W44, were then released in 2016.

Data confirmed the presence of AME in all the regions, in particular, with a significance of $21.2\,\sigma$, $10.2\,\sigma$ and $7.7\,\sigma$ respectively for W43, W47 and W44 at the frequency of 18.7 GHz. This result confirmed as the new low frequencies QUIJOTE data give a huge contribution in modelling the AME.
At time of writing, the final maps obtained with the MFI are almost complete and will be released soon, moreover, several papers based on these new data are quite advanced and will be presented in near future.

Chapter 4

The Pointing Model of the QUIJOTE Second Telescope

Observations of celestial objects through a telescope are possible if we properly point the telescope itself. However, any real telescope is a non-ideal system and therefore it is affected by instrumental non-idealities which make this task not trivial.
The pointing model is a mathematical implementation with the aim of correcting these pointing non-idealities for an altazimuth telescope. The full treatment, plus its linearized version, will be presented. B because of computational effort, only the linearized version will be actually used in practice, supported by the fact that the corrections are expected small. [22]
In conclusion, we will present the pointing model parameters obtained for the second *QUIJOTE* telescope.

4.1 The Pointing Model

When we want to look at a specific point in the sky, the Pointing Model is a model which describes the relation between the *nominal coordinates* (A, E), i.e. the real horizon coordinates associated to the point, and the so-called *encoder coordinates* (A', E') i.e. the coordinates we have to encode in our instrument to look at that point

$$\mathcal{P}: \ (A, E) \longmapsto (A', E'). \tag{4.1}$$

where A is the *azimuth* angle and E is the *elevation* angle (see B.1).
In principle, encoding the nominal coordinates to an ideal telescope, it will point to the right direction, therefore, equation (4.1) is a simple equality. Instead, a real telescope is affected by some shifts, thus, when the nominal coordinates are inserted in the telescope, it will point to a different direction, or vice versa, when we point to the right direction, the encoder coordinates of the instrument will be different to the nominal ones. In other words, the function (4.1) is not an equality anymore, but a complicated function we will try to describe.

Encoder function
First, let define the so-called *Encoder function* Φ, the map which relates angular coordinates to pointing unit vectors, in our case, the encoder function relates the

encoder coordinates to the unit vector $\mathbf{r}$ and the nominal coordinates to the unit vector $\mathbf{r}'$

$$\begin{aligned} \mathbf{r}' &\doteq \Phi(A, E) \\ \mathbf{r} &\doteq \Phi(A', E') \end{aligned} \tag{4.2}$$

at practical level, it is telling us that if we want to look at the direction $\mathbf{r}$ we have to insert in our telescope the coordinates (A', E'), instead, when input coordinates are imposed on (A, E), our telescope points to $\mathbf{r}'$.
In case of an ideal instrument, there is not a difference between encoder and nominal coordinates, thus, the two unit vectors are the same $\mathbf{r}' = \mathbf{r}$ and the encoder function takes the simple form ($\Phi = \phi$)

$$\mathbf{r} = \phi(A, E) = \begin{pmatrix} -\cos E \cos A \\ \cos E \sin A \\ \sin E \end{pmatrix}. \tag{4.3}$$

For a real instrument, the equality does not hold anymore ($\Phi \neq \phi$) and the two unit vectors are linked by a not trivial function, which is in general a *rotation*

$$\mathcal{R} : \ \mathbf{r}' \longmapsto \mathbf{r}. \tag{4.4}$$

By mean of few manipulations, we can see that

$$\begin{aligned} (A', E') = \Phi^{-1}(\mathbf{r}) = \Phi^{-1}(\mathcal{R}\ \mathbf{r}') = \Phi^{-1}(\mathcal{R}\ \Phi(A, E)) \ &= \mathcal{P}(A, E) \\ (A, E) = \phi^{-1}(\mathbf{r}) = \phi^{-1}(\mathcal{R}\ \mathbf{r}') \ &= \Phi^{-1}(\mathbf{r}') \end{aligned} \tag{4.5}$$

where in the top equation we used (4.2), (4.4), again (4.2) and (4.1), and in the bottom we used (4.2), (4.4) and again (4.2), respectively at each step. These two relations have a much simple form if the arguments are understood

$$\begin{aligned} \mathcal{P} &= \Phi^{-1} \circ \mathcal{R} \circ \Phi \\ \Phi^{-1} &= \phi^{-1} \circ \mathcal{R} \end{aligned} \tag{4.6}$$

therefore, we can find a explicit expression of the function (4.1) in terms of quantities (4.3) and (4.4)

$$\mathcal{P} = (\phi^{-1} \circ \mathcal{R}) \circ \mathcal{R} \circ (\phi^{-1} \circ \mathcal{R})^{-1} = \phi^{-1} \circ \mathcal{R} \circ \phi \tag{4.7}$$

this is a very useful relation because it tells us that, in order to compute the encoder coordinates, we can compute the versor components associated to the nominal coordinates of a particular direction, apply the rotations to correct the versor direction, and re-compute its coordinates, the encoder coordinates, after the rotation. Thus, we have moved the problem of finding a map between coordinates, to the problem of finding the rotation, or angular shifts, between directions.
In principle, we know that the right rotation between the unit vectors $\mathbf{r}'$ and $\mathbf{r}$ can be very complicated, we will present the analytic result, but, because we expect the difference in the two directions not so large, we can treat the rotations as linear corrections $\Delta\mathcal{R}$ to the identity function

$$\mathbf{r} = \mathcal{R}\ \mathbf{r}' = (\mathbb{1} + \Delta\mathcal{R})\ \mathbf{r}' = \mathbf{r}' + \Delta\mathbf{r}. \tag{4.8}$$

The model
When dealing with a real telescope a series of effects need to be taken into account. We

will consider the telescope non-idealities described by Denis Tramonte [23], the model is based on a number of pointing parameters, the ones employed by the TPOINT software, which have a clear physical intuition. The set of all the parameters is what we roughly call the *Pointing Model* of the telescope.
In the following all the non-idealities.

- The *Hooke's Law* vertical flexure
  The effect is related to the flexure of the telescope structure due to gravity, which leads to a lowering of the real elevation. Thus, the correction consists in a rotation upward in elevation, which can be quantified by ζ, the so called the bending angle, between the nominal direction and the real one.
  At computational level, the correction will depend on the coordinates toward which the telescope is pointing, indeed, the correction is described by the combination
  $$\mathbf{r} = \mathcal{R}_H \ \mathbf{r}' = \mathcal{R}^z_{A'}{}^{-1} \ \mathcal{R}^y_\zeta \ \mathcal{R}^z_{A'} \ \mathbf{r}' \tag{4.9}$$
  where $\mathcal{R}_A$ is the rotation around the z-axis of an angle equal to the azimuth A', in order to bring the telescope direction parallel to the zero-azimuth direction, and $\mathcal{R}_\zeta$ is the actual rotation around the y-axis of the bending angle ζ
  $$\mathcal{R}^z_{A'} = \begin{pmatrix} \cos A' & -\sin A' & 0 \\ \sin A' & \cos A' & 0 \\ 0 & 0 & 1 \end{pmatrix} \quad \mathcal{R}^y_\zeta = \begin{pmatrix} \cos\zeta & 0 & -\sin\zeta \\ 0 & 1 & 0 \\ -\sin\zeta & 0 & \cos\zeta \end{pmatrix}. \tag{4.10}$$
  Performing the products, we end up with a quite complicated matrix
  $$\mathcal{R}_H = \begin{pmatrix} \cos^2 A' \cos\zeta + \sin^2 A' & \cos A' \sin A'(1-\cos\zeta) & \cos A' \sin\zeta \\ \cos A' \sin A'(1-\cos\zeta) & \cos^2 A' + \sin^2 A' \cos\zeta & -\sin A' \sin\zeta \\ -\cos A' \sin\zeta & \sin A' \sin\zeta & \cos\zeta \end{pmatrix} \tag{4.11}$$
  which represent the complete rotation. As anticipated, we expect the effect, so the bending angle, to be small
  $$\begin{aligned} \cos\zeta &\approx 1 \\ \sin\zeta &\approx \zeta \end{aligned} \tag{4.12}$$
  thus, we can expand the matrix (4.11) to first order in ζ
  $$\mathcal{R}_H = \mathbb{1} + \Delta\mathcal{R}_H = \mathbb{1} + \begin{pmatrix} 0 & 0 & \zeta\cos A' \\ 0 & 0 & -\zeta\sin A' \\ -\zeta\cos A' & \zeta\sin A' & 0 \end{pmatrix}. \tag{4.13}$$
  In general the flexure depends on the telescope initial tilt, i.e. on the pointed elevation, in particular, it makes the telescope droop in proportion to the cosine of the elevation; because of this effect, according to the W08, we define the parameter
  $$P_f = \frac{\zeta}{\cos E'} \tag{4.14}$$
  which quantifies the telescope vertical flexure. In conclusion, the correction to the flexure of the telescope can be described by the term
  $$\Delta\mathbf{r}_H = \Delta\mathcal{R}_H \ \mathbf{r}' = \begin{pmatrix} -P_f \ z'x' \\ -P_f \ z'y' \\ P_f \ (x'^2 + y'^2) \end{pmatrix}. \tag{4.15}$$

- The *roll-axis misalignment*
  This non-ideality refers to the misalignment of the azimuth axis with respect to the vertical, or, from a different point of view, it is a tilt of the telescope basis with respect to the horizontal xy-plane. As the previous case, the correction is performed by mean of three rotations

$$\mathbf{r} = \mathcal{R}_M \ \mathbf{r}' = \mathcal{R}_\Omega^{z\ -1} \ \mathcal{R}_\theta^y \ \mathcal{R}_\Omega^z \ \mathbf{r}', \tag{4.16}$$

  $\mathcal{R}_\Omega$ is a rotation around the z-axis of an angle Ω and $\mathcal{R}_\theta$ is a rotation around the y-axis of an angle θ, the two angles parameterize the magnitude θ and the direction Ω of the tilt

$$\mathcal{R}_\Omega^z = \begin{pmatrix} \cos\Omega & -\sin\Omega & 0 \\ \sin\Omega & \cos\Omega & 0 \\ 0 & 0 & 1 \end{pmatrix} \quad \mathcal{R}_\theta^y = \begin{pmatrix} \cos\theta & 0 & -\sin\theta \\ 0 & 1 & 0 \\ -\sin\theta & 0 & \cos\theta \end{pmatrix}. \tag{4.17}$$

  The resulting matrix will be perfectly analogues to the vertical flexure's one, simply replacing $A' \leftrightarrow \Omega$ and $\zeta \leftrightarrow \theta$ in (4.11). We skip some steps and show directly the approximated version, in this case we assume the magnitude θ to be small and so we linearize (4.12) with respect to it

$$\mathcal{R}_M = \mathbb{1} + \Delta\mathcal{R}_M = \mathbb{1} + \begin{pmatrix} 0 & 0 & \theta\cos\Omega \\ 0 & 0 & -\theta\sin\Omega \\ -\theta\cos\Omega & \theta\sin\Omega & 0 \end{pmatrix}. \tag{4.18}$$

  We now have two degrees of freedom, thus, we need to define two pointing parameters

$$\begin{aligned} P_x &= \theta\cos\Omega \\ P_y &= -\theta\sin\Omega \end{aligned} \tag{4.19}$$

  note as both the parameters contribute to the tilt magnitude $P_x^2 + P_y^2 = \theta^2$, indeed, when $\Omega = 0$: $P_y = 0$ and $P_x = \theta$, so P_x represents the tilt component along the x axis, and when $\Omega = 1/2$: $P_x = 0$ and $P_y = \theta$, so P_y represents the tilt component along the y axis.
  In conclusion, the correction to the misalignment of the azimuth axis can be described by the term

$$\Delta\mathbf{r}_M = \Delta\mathcal{R}_M \ \mathbf{r}' = \begin{pmatrix} -P_x \ z' \\ -P_y \ z' \\ -P_f x' - P_y y' \end{pmatrix}. \tag{4.20}$$

- *Non-perpendicularities*
  This non-ideality can be of two types: (i) non-perpendicularity between the mount axes and the azimuth and (ii) non-perpendicularity between the telescope and the "pitch" axis. The first is related to the fact the telescope that at $(A, E) = (0, \pi/2)$ does not point towards the zenith, but it is displaced in elevation by an angle Δ. The second is related to the fact that at $(A, E) = (0, \pi)$ the telescope

does not point towards the x-axis, but it is shifted in azimuth by an angle Δ' with respect to it.
In this case the computation is a bit longer, but the steps, taken separately, are simple. Let begin calling $\mathbf{e}$ the unit vector associated to the nominal coordinates $(A, E) = (0, \pi)$, it is related to $\mathbf{r}'$ and $\mathbf{r}$ by mean of the rotations

$$\begin{aligned} \mathbf{r}' &= \mathcal{R}'_\pi \ \mathbf{e} \\ \mathbf{r} &= \mathcal{R}_\pi \ \mathbf{e}. \end{aligned} \tag{4.21}$$

We can invert the first equation and insert in the second one (4.21), such that

$$\mathbf{r} = \mathcal{R}_\pi \ {\mathcal{R}'_\pi}^{-1} \ \mathbf{r}' = \mathcal{R}_P \ \mathbf{r}' \tag{4.22}$$

$\mathcal{R}_P$ is the final rotation, associated to the non-perpendicularities, that we are trying to parameterize. In equations (4.21), the rotation $\mathcal{R}'_\pi$ is the simple projection of the vector $\mathbf{r}'$ along the vector $\mathbf{e}$, which is parallel and inverse to the x-axis, in formulas, $\mathcal{R}'_\pi$ is computed considering a first rotation around the y-axis of the elevation angle E and then a rotation around the z-axis of the angle π-A

$$\mathcal{R}'_\pi = \mathcal{R}^z_{\pi-A}\mathcal{R}^y_E = \begin{pmatrix} -\cos A \cos E & -\sin A & \cos A \sin E \\ \sin A \cos E & -\cos A & -\sin A \sin E \\ \sin E & 0 & \cos E \end{pmatrix}. \tag{4.23}$$

The rotation $\mathcal{R}_\pi$ in (4.21) is also a projection, but it is a bit more complicated because of the presence of the non-idealities, indeed, besides the two rotations $\mathcal{R}^z_{\pi-A}$ and $\mathcal{R}^y_E$, there are other two rotations

$$\mathcal{R}_\pi = \mathcal{R}^z_{\pi-A} \ \mathcal{R}^x_\Delta \ \mathcal{R}^y_E \ \mathcal{R}^z_{\Delta'} \tag{4.24}$$

where $\mathcal{R}^x_\Delta$ and $\mathcal{R}^z_{\Delta'}$ are exactly rotation around the x-axis and z-axis of respectively an angle Δ and Δ', which represent the corrections due to the two non-perpendicularities. The resulting $\mathcal{R}_\pi$ is a very large matrix.
The next step is to invert $\mathcal{R}'_\pi$ and multiply by $\mathcal{R}_\pi$, we skip the mathematical details which lead to a very complex matrix to be linearized. At the end the resulting correction to the non-perpendicularities can be described by the term

$$\Delta\mathbf{r}_P = \Delta\mathcal{R}_P \ \mathbf{r}' = \begin{pmatrix} w \ (y' - w \ x') \\ -w \ (x' + w \ y') \\ 0 \end{pmatrix} \tag{4.25}$$

note as this first-order derivation of the non-ideality correction does not affect the z component. The quantity

$$w = \frac{P_c + P_n \ z'}{\sqrt{x'^2 + y'^2}} \tag{4.26}$$

is a combination of the two parameters P_c and P_n which enter in our model, the relation of these with the angles Δ and Δ' is

$$\begin{aligned} P_c &= -\Delta' \\ P_n &= \Delta. \end{aligned} \tag{4.27}$$

- *Encoder index errors*
  The last non-ideality is different from the previous ones because it applies directly at coordinates level and may be due to offset error in handling the input coordinates. It is require the corrections are considered after the transformation, vector to coordinates, with the encoder function, by adding two parameters to the coordinates themselves

$$\begin{aligned} A' &\longrightarrow A' + P_a \\ E' &\longrightarrow E' - P_b. \end{aligned} \tag{4.28}$$

  A' and E' are the coordinates we shall finally input to the telescope encoder to ensure it points to the required direction.

To summarize, we have seven parameters: five to apply at vector level and two at coordinates level, which parametrize four different non-idealities. All together, they represent our *Pointing Model* $\mathcal{P}$ $(P_f, P_x, P_y, P_c, P_n, P_a, P_b)$.
The equation have been double checked analytically and computationally, we implemented the Python code and compared it with the previous IDL implementation at the IAC.

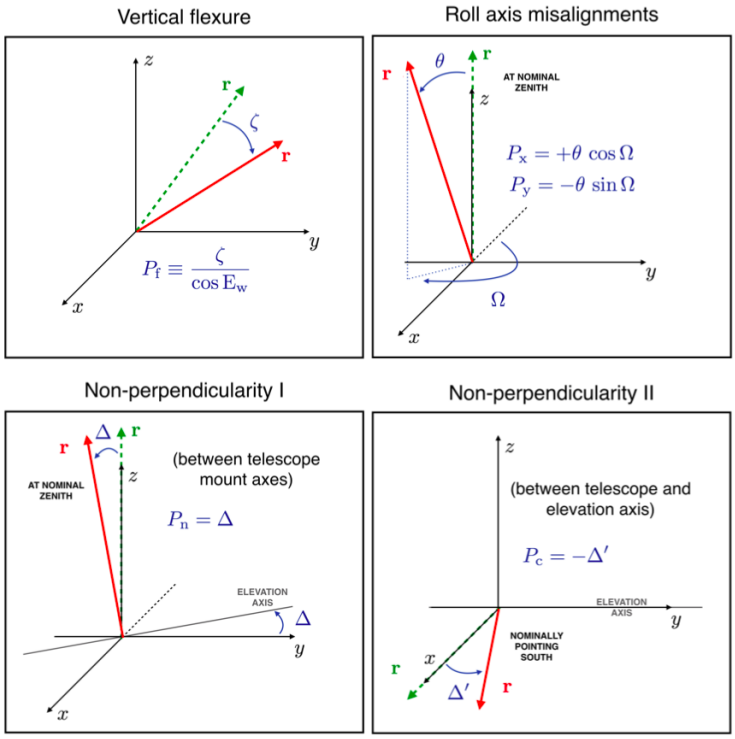

Figure 4.1: Telescope non-idealities. The green **r** is the unit vector related to the encoder coordinates (A', E') and the red **r** is the unit vector related to the nominal coordinates (A, E). The parameters P_i with $i = f, x, y, n, c$ are part of the Pointing Model. [23]

Pointing the Sky

Till now, we have described a model which is telling us how to find the encoder horizon coordinates from the nominal horizon coordinates, i.e. by knowing where the telescope is actually pointing we can find the corresponding encoder coordinates.
This is only part of the whole set of coordinate transformations that are useful for observations because our telescope is pointing the sky, thus, at the end, we want a procedure to relate the position of celestial objects on the sky to the encoder horizon coordinates given by our instrument, or vice versa

$$(\alpha, \delta) \longleftrightarrow (A', E'). \tag{4.29}$$

α and δ are respectively the right ascension (RA) and the declination (Dec), the so-called *celestial coordinates* which characterize the equatorial J2000 frame (see B.1). The general relation between celestial and horizon coordinates is not trivial, it depends on the Earth location (latitude, longitude and height) of the telescope and the observation time, moreover, as stressed different times, the horizon coordinates which we obtain by mean of this transformation are the nominal ones (see B.2).
Therefore, the real relation (4.29) needs an intermediate step

$$(\alpha, \delta) \longleftrightarrow (A, E) \xrightarrow{\mathcal{P}} (A', E') \tag{4.30}$$

where $\mathcal{P}$ is the function (4.1) defined by our *Pointing Model*.
The prescription to obtain the encoder horizon coordinates starting from the celestial coordinates is

- find the nominal coordinates (A, E) from the celestial coordinates (α, δ) by mean of coordinates transformation
- find the direction of the unit vector $\mathbf{r}'$ from the nominal coordinates (A, E) by mean of ϕ (4.3)
- apply the vertical flexure, azimuth tilt and non-perpendicularities first order corrections to $\mathbf{r}'$

$$\mathbf{r} = (\mathbb{1} + \Delta\mathcal{R}_P\ (\mathbb{1} + \Delta\mathcal{R}_M\ (\mathbb{1} + \Delta\mathcal{R}_H)))\ \mathbf{r}' \tag{4.31}$$

- find the encoder coordinates (A', E') from the direction of the unit vector $\mathbf{r}$ by mean of ϕ^{-1} (4.3)
- apply the encoder index errors to the encoder coordinates

$$(A', E') \longrightarrow (A' + P_a,\ E' - P_b). \tag{4.32}$$

The inverse process, i.e. getting the celestial coordinates starting from the encoder coordinates, is in principal simply achieved inverting the listed steps, but, in reality, the task is non trivial because the linear corrections (4.31) are computed on the vector $\mathbf{r}'$. In the inverse process we start with the vector $\mathbf{r}$ and we apply the inverse corrections, but this could lead to increasing errors.
To prevent this problem we can use an iteration mechanism: starting from $\mathbf{r}$, we compute a first linear correction ($\Delta\mathbf{r}_1$), we apply the correction to $\mathbf{r}$ obtaining $\mathbf{r}_1 = \mathbf{r} - \Delta\mathbf{r}_1$, then, we repeat the recipe with $\mathbf{r}_1$ obtaining $\mathbf{r}_2 = \mathbf{r} - \Delta\mathbf{r}_2$ and so on, till the corrections become stable.

In formulas, at each n-step, we compute the model correction $\Delta\mathbf{r}_n$, we subtract it directly from $\mathbf{r}$ and define the resulting vector $\mathbf{r}_{n+1}$

$$\begin{aligned} \mathbf{r}_n &\longrightarrow \Delta\mathbf{r}_n \\ \mathbf{r}_{n+1} &= \mathbf{r} - \Delta\mathbf{r}_n \end{aligned} \tag{4.33}$$

we stop the procedure when the correction is smaller than a limit we impose

$$|\Delta\mathbf{r}_n - \Delta\mathbf{r}_{n+1}| \leq 10^{-6}. \tag{4.34}$$

Again, we implemented the Python code and compared it with the previous implementation and we checked the consistency of the procedure just described.

4.2 Parameter Estimation for QT2

In the previous section we kept things more general as possible in order to describe the Pointing Model with seven parameters without specify their values. The main goal of this section is to find the best estimation of the model parameters for a particular case: the second QUIJOTE telescope (QT2). The prescription and methodology we will present in the following, in principle, can be generalized to any altazimuth telescope.
The basic idea in order to perform the estimation is: we look on real observations from our instruments (TGI and FGI) of two known point radiosources, in particular two *Supernova Remnant (SR)*: *Cassiopea A* and *Crab Nebula*, which have well known celestial coordinates (α, δ) in J2000

$$\begin{aligned} Crab &: (83.633^\circ,\ 22.014^\circ) \\ Cas\ A &: (350.850^\circ,\ 58.815^\circ). \end{aligned} \tag{4.35}$$

We transform these in the nominal horizon coordinates, plus, we look at which encoder horizon coordinates, given by the instruments, are associated and finally we fit the best function which relates the two pair of coordinates: nominal and encoder. The resulting function is our Pointing Model.
It is important to underlying that the choice of sources is not random, we selected them because: first, they are two bright well-known polarized point sources, but also, they are in the two opposite north quadrants of the celestial sphere, this feature is important if we want to set a good pointing of the full celestial north hemisphere.
In the following, the parameters estimation procedure will be described in full details.

Data Preselection
The fit is going to be performed on 64 observations: 39 of Crab and 25 of Cas A, taken during February and March 2019

CRAB-190219-1847	CRAB-190304-2251	CRAB-190316-2205	CASS-190226-1716
CRAB-190219-2343	CRAB-190305-1606	CRAB-190317-1705	CASS-190227-1129
CRAB-190220-1842	CRAB-190305-1709	CRAB-190317-2201	CASS-190302-1118
CRAB-190220-2338	CRAB-190307-1558	CRAB-190318-2157	CASS-190304-1653
CRAB-190221-1838	CRAB-190307-1701	CRAB-190319-1657	CASS-190305-1123
CRAB-190221-2334	CRAB-190308-1726	CRAB-190319-2153	CASS-190309-1050
CRAB-190222-1834	CRAB-190309-2232	CRAB-190320-1653	CASS-190311-1043
CRAB-190222-2330	CRAB-190310-1732	CASS-190219-1744	CASS-190313-1020
CRAB-190223-1830	CRAB-190310-2228	CASS-190220-1157	CASS-190313-1123
CRAB-190223-2326	CRAB-190311-2224	CASS-190220-1740	CASS-190314-0741
CRAB-190224-2322	CRAB-190312-2203	CASS-190221-1736	CASS-190314-0945
CRAB-190225-1822	CRAB-190313-1919	CASS-190223-1145	CASS-190317-1603
CRAB-190225-2318	CRAB-190313-2130	CASS-190223-1728	CASS-190318-1016
CRAB-190226-1818	CRAB-190315-1911	CASS-190224-1141	CASS-190318-1559
CRAB-190226-2314	CRAB-190315-2017	CASS-190225-1137	CASS-190319-1012
CRAB-190302-2259	CRAB-190315-2225	CASS-190226-1133	CASS-190319-1555

Table 4.1: Observations list. File name format is: source name - date (year, month, day) - time (hour, minute)

Each observation given by the instruments is encoder in huge files containing few minutes of observation, but, the crossing of the source is encoder in just few seconds. Thus, the main part of the observational data is useless for our propose and can be removed by mean of a first smart data preselection.

- *Smoothing*: the typical time stamp of the instrument is of 4 ms, the crossing of the source is of order of few seconds, therefore we can smooth data taking the mean value every 10 consecutive acquisitions. At the end, this will speed up computations, but also decrease the noise.

- *Baselines*: the output of the instrument is in Volt, and as every real electronic output is effected by systematic noise which slightly changes with time and shifts the voltage *zero-level*. Therefore, we remove this baseline computing the median every 150 consecutive acquisitions (about every 6 seconds) and subtracting it from the data.

- *Selection*: the prior, on which the model is based on, is that the pointing corrections are supposed to be small. Thus, we take the encoder coordinates given by our instrument, transform them in celestial coordinates (4.3) without pointing model corrections, and we discard all points separated by more than 3 degrees from the nominal coordinates of the sources (4.35). This selection will remove a huge useless amount of data.

Once the preselection is done, we remain with only the set of meaningful data.

Output Response

After the preselection, our set of data is composed of lists of observations, each list is composed by almost instantaneous acquisitions and for each acquisition we report the associated encoder horizon coordinates and the output measure, as given directly by the instruments. From these acquisition data, knowing the encoder horizon coordinates we can simulate the output measure, i.e. we build an ideal response of our instruments to the source crossing.

To do so, first we have to transform the encoder coordinates in celestial coordinates, here comes the pointing model correction

$$(A', E') \xrightarrow{\mathcal{P}^{-1}} (A, E) \longrightarrow \mathbf{r}(\alpha, \delta) \tag{4.36}$$

in truth, we apply the inverse procedure of the Pointing model (4.33-4.34). The seven model parameters are picked with a *Monte Carlo* simulation that we will explain in the following. Then, assuming that the telescope output, at least at first order, is an unnormalized *Gaussian* function, we write the ideal simulated instrument output as

$$\mathcal{S}\ (\mathbf{r}, \mathbf{r_s}) = A\ \exp\Big[-\frac{1}{2}\frac{\theta(\mathbf{r}, \mathbf{r_s})^2}{\sigma_s^2}\ \Big] \tag{4.37}$$

A is normalize factor, in the exponential numerator, the function $\theta(\mathbf{r}, \mathbf{r_s})$ is the *angular separation* between the nominal celestial position of the source $\mathbf{r_s} = (\alpha_s, \delta_s)$ and a general point on the sky $\mathbf{r} = (\alpha, \delta)$

$$\theta(\alpha, \delta, \alpha_s, \delta_s) = \cos^{-1}\left[\sin(\delta)\sin(\delta_s) + \cos(\delta)\cos(\delta_s)\cos(\alpha - \alpha_s)\right] \tag{4.38}$$

thus, the simulated ideal instrument output peaks when $\mathbf{r} = \mathbf{r_s}$, i.e. at the exact nominal position of the source. In the exponential denominator, the variable σ_s is related to the Full Width High Maximum, or $FWHM$, of the real instrument beam

$$\sigma_s = \frac{FWHM}{\sqrt{8\log 2}}\ , \tag{4.39}$$

with $FWHM \sim 0.37^\circ$ (Table 3.3).
After the data selection, the encoder to nominal to celestial coordinates transformation and the ideal response construction, we end up with two set of data associated to the same encoder coordinates: the real data measured by the instrument and the simulated data computed as explained.
If the Pointing model is correct, the peak of the real data would perfectly match with the ideal peak at the nominal source position, otherwise a consistence difference would arise. To quantify the goodness of the applied model, we define the *Chi-squared* as

$$\chi^2 = \sum_{i=1}^{k} \frac{(\mathcal{O}\ (\mathbf{r_i}, \mathbf{r_s}) - \mathcal{S}\ (\mathbf{r_i}, \mathbf{r_s}))^2}{\sigma_{_{RMS}}^2} \tag{4.40}$$

where $\mathcal{O}$ represents the set of real data, $\mathcal{S}$ the ideal response and $\sigma_{_{RMS}}$ is the *root mean squared* (or *standard deviation*) of the noise, i.e. what remain removing the significant peak from the real data.
To summarize, the described steps are:

(i) Select the seven Pointing model parameters;

(ii) Apply the inverse pointing procedure to the encoder coordinates;

(iii) Transform the coordinates from horizon to celestial;

(iv) Construct the ideal response;

(v) Compare the real data with the ideal response;

If the comparison is not giving consistency between data e ideal output, we discard the seven initial parameters and pick new ones till we find the best fit. In few worlds, we are solving a problem of *Chi-squared minimization* with a *Monte Carlo Simulation*.

Monte Carlo Simulation
Last important thing to discuss is how the seven parameters are peaked (i).
We suppose that the main correction for a telescope, in term of angular offsets, comes from the Encoder index errors (4.28), therefore, we decide to devide the pointing parameters estimation in two parts.

- First, we fix the five parameters $P_f,\ P_x,\ P_y,\ P_c,\ P_n$ to zero and pick random values for the two shifts P_a and P_b from a truncated Gaussian distribution centered in 0, with standard deviation of 1° and range between $[-3^\circ, 3^\circ]$. We run the simulation (i-v) 2 000 times, and we accept the couple (P_a, P_b) which best minimized the chi squared.
  At computational level, at each step $i \in [1, 2\,000]$, we:

  - Pick $(P_a, P_b)_i$ from truncated Gaussian;
    $(center = 0,\ \sigma = 1^\circ,\ range = [-3^\circ, 3^\circ])$
  - Compute the Pointing model corrections and the Chi-squared χ_i^2;
  - If $\chi_i^2 < \chi_j^2$, accept the new parameters;

  where the j-th step was the one related to the best fit until the $(i-1)$-th step.

- Then, we pick random values for all the seven parameters $P_f,\ P_x,\ P_y,\ P_c,\ P_n,\ P_a,\ P_b$ from truncated Gaussian distributions with standard deviation of 0.1° and range between $[-3^\circ, 3^\circ]$. In the first step, we pick values for the first five from Gaussian centered in zero, instead, for the shifts P_a and P_b, we pick values from Gaussian centered in the best values estimated in the previous part. Then, recursively, if the chi squared computed at one step is smaller than the one computed at the previous step, the new parameters are used as the center of the distributions for the next steps.
  At computational level, at each step $i \in [2\,000, 12\,000]$, we:

  - Pick $(P)_i$ from truncated Gaussian;
    $(center = (P)_j,\ \sigma = 0.1^\circ,\ range = [-3^\circ, 3^\circ])$
  - Compute the Pointing model corrections and the chi squared χ_i^2;
  - If $\chi_i^2 < \chi_j^2$ accept the new parameters;

  where the j-th step was the one related to the best fit until the $(i-1)$-th step.

4.3 Focal Plane

The Thirty-Gigahertz Instrument (TGI) and Forty-Gigahertz Instrument (FGI) are been designed to carry 31 polarimeters each, sharing the same common cryostat. Nevertheless, at the moment of writing, only six feedhorns, three per instrument, are actually been installed and in operation.

Feedhorns position

We call *horn 1* the TGI feedhorn located at the center of the focal place, the others are arranged equidistant in a ring at a distance of $\sim 86.6\,\text{mm}$ from the center (Table 4.2).

The experimental acquisition system is built to give measurements of all the operative feedhorns, but, it also associates them to the same set of encoder horizon coordinates, whatever the feedhorn number is. This procedure is not correct in principle, because the position on the focal plane, by simple projection rules, will effects the coordinates in local and celestial frame.

Thus, we can assume that the encoder coordinates are only the ones associated to the central feedhorn, or *horn 1*, and we compute the coordinates associated to the other feedhorns by mean of the *gnomonics* projection formalism.

	horn	x [mm]	y [mm]
TGI	1	0.0	0.0
	2	86.6	0.0
	3	43.3	75.0
FGI	4	-43.3	75.0
	5	-86.6	0.0
	6	-43.3	-75.0

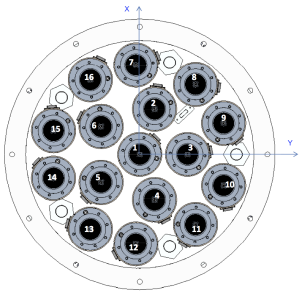

Table 4.2: Left: feedhorn position on the focal plane, right: focal plane structure

Horn projection

The horizon coordinates are nothing else than spherical coordinates, thus, they generate an half sphere centered in the telescope position and with radius equal to the focal length. From this geometrical view, the focal plane can be seen as the plane tangent to this sphere and its center would coincide with the local coordinates of the central feedhorn, i.e. our encoder coordinates (A, E).

We define the *standard* coordinates, as the local frame of the focal plane (x,y) in Table 4.2, and the *differential* coordinates, the angular displacements with respect to the encoder coordinates $(\Delta A, \Delta E)$ in Figure 4.2. The transformation from differential coordinates to standard coordinates is called *gnomonic* or *central* projection. [24]

In the following, we will present the main steps of the full computation to get the final projection transformation.

In Figure 4.2, let define B, a point on the sphere, and B' its projection on the plane tangent to the sphere in position P. In our case P is the central horn location and the point B' will represent the position of a different horn. Let call r the angle POB and θ the angle between the plane POB and the meridian plane, counted clockwise. Thus, we can expressed the standard coordinates of B' on the tangent plane as functions of these two angles and the focal length f

$$\begin{aligned} x &= f\ \tan r\ \sin\theta \\ y &= f\ \tan r\ \cos\theta \end{aligned} \tag{4.41}$$

the two angles r and θ are related to the differential coordinates through the following

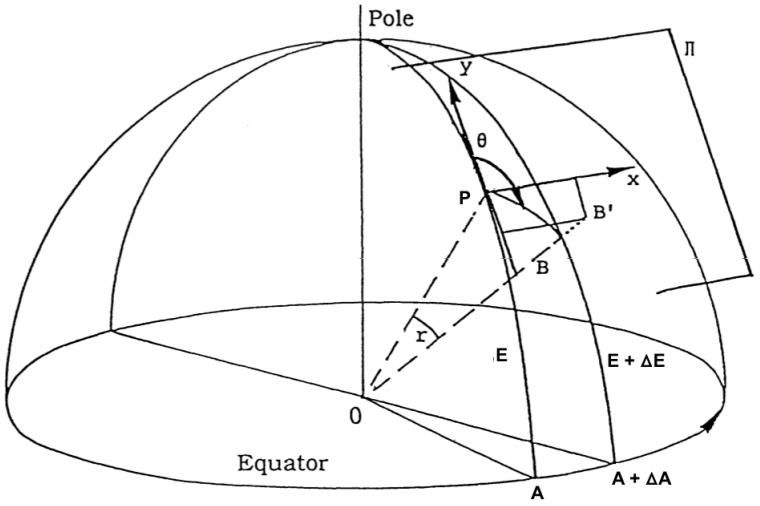

Figure 4.2: Horizon and differential coordinates [24]

trigonometric relations

$$\begin{aligned} \cos r &= \sin E \sin(E+\Delta E) + \cos E \cos(E+\Delta E)\cos\Delta A \\ \sin r \sin\theta &= \cos(E+\Delta E)\sin\Delta A \\ \tan\theta &= \frac{\sin\Delta A}{\cos E \tan(E+\Delta E) - \sin E \cos\Delta A} \ . \end{aligned} \tag{4.42}$$

Inserting the relations (5.18) in the equations (4.41), we end up with the analytic form of the general transformation between the standard coordinates and the differential coordinates

$$\begin{aligned} x &= -f \ \frac{\sin\Delta A}{\cos E \ (\tan E \tan(E+\Delta E) + \cos\Delta A)} \\ y &= f \ \frac{\tan(E+\Delta E) - \tan E \cos\Delta A}{\tan E \tan(E+\Delta E) + \cos\Delta A} \ . \end{aligned} \tag{4.43}$$

The transformation are quite complicated, but in principle we know that the distances between the central horn and the others are small, order of few centimeters, thus, we can expand (4.43) at fist order with respect to the corrections ΔA and ΔE

$$\begin{aligned} x &= -f \ \tan\Delta A \cos E \\ y &= f \ \tan\Delta E \end{aligned} \tag{4.44}$$

this form seem much simpler and intuitive, indeed, at first order, x and y are nothing more than the tangent value of ΔA and ΔE respectively, corrected by the elevation ($\cos E$ factor). However, these approximated expressions are incorrect because the expansion is not valid for angles close to the poles ($E = \pm\ 90°$), therefore, in our final treatment we will use the complete form.
Back to the original problem, knowing the standard coordinates of the horns we would

like to find their associated differential coordinates, thus, we need the inverse of equation (4.43), we skip all the tedious mathematical passages and present the final result [23]

$$\begin{aligned} \tan \Delta A &= x' \cos E \ \frac{1+\tan^2 E}{1-y' \tan E} \\ \tan \Delta E &= \frac{K - \tan E}{1 + K \tan E} \end{aligned} \tag{4.45}$$

with $x' = -x/f$, $y' = y/f$ and

$$K = \cos \Delta A \ \frac{y' + \tan E}{1 - y' \tan E} \ . \tag{4.46}$$

Focal plane correction
In the first section of this chapter we showed the steps, in both directions, we have to follow to related the celestial coordinates to the encoder horizon coordinates (4.30). At this point we have learned that the encoder coordinates we find in this way are only the ones associated to the central feedhorn, thus, the general relation which holds whatever horn we consider is

$$(\alpha, \delta) \longleftrightarrow (A_h, E_h) \xrightarrow{\mathcal{H}} (A, E) \xrightarrow{\mathcal{P}} (A', E') \tag{4.47}$$

where, when the transformation from celestial to horizon coordinates is performed, we end up with the nominal coordinates associated to the particular horn. Thus in order to go back to the central nominal coordinates and encoder coordinates, which at the end are the ones given bu the instrument, we have to pass through to another step, the *focal plane* correction $\mathcal{H}$

$$(A_h, E_h) = \mathcal{H}(A, E) = (A + \Delta A, E + \Delta E) \tag{4.48}$$

where ΔA and ΔE are given by the equations (4.45).
The focal plane correction is, in principle, independent to the Pointing model itself, because all the non-idealities presented in the first section are related to the telescope issues and not to the single feedhorns. Therefore, the prescription we presented in the second section to estimate the model parameters still holds for all the feedhorns simply applying the intermediate horn position step (4.48).
According to the geometry of the system, we can proceed with the instruments pointing calibration in two different ways

- We construct an unique Pointing Model for the whole instrument, i.e. we completely ignore the focal plane correction in the parameter estimation simply considering observations from the central feedhorn (4.30), then, we test if our model fits for all the horns applying the focal position correction (4.47).
- We construct a different Pointing Model for each feedhorn, i.e. we run the parameters estimation procedure for each feedhorn applying the focal plane correction (4.47).

At the end, both the ways are been tested and compared, the results are presented in the next section.

4.4 Results and Discussion

In the following, we will present the pointing model parameter estimation results of the second QUIJOTE telescope (QT2). First, we will present the results obtained from the analysis of the central feedhorns, then, we will discuss about all the others.

Central horn
The parameter estimation has been performed with two Monte Carlo simulations, as described in the previous section.
The first simulation seems to minimize the Chi-squared very quickly, indeed, it will turn out that the main correction is from the encoder index error in the Azimuth angle P_a, almost 3°, the encoder error in the Elevation angle is much smaller (Figure 4.3 Left), as we would expect for an altazimuth telescope.
The second simulation lead to values, for all the parameters, much smaller than the Azimuth encoder error. However, the parameters related to the non-perpedicularities are of order of $\sim 0.5°$ with inverse sign, recalling the definition (4.27), it is consistent with the fact that the telescope is affected by a shift in the Azimuth angle. At the end, the vertical flexure and roll-axis misalignment related parameters are much smaller, of order of few asec.

non-ideality	parameter	Value [asec]
vertical flexure	P_f	-270.6
x roll-axis misalignment	P_x	-1.7
y roll-axis misalignment	P_y	-11.2
non-perpendicularity I	P_c	1877.6
non-perpendicularity II	P_n	-1894.1
Azimuth index error	P_a	10680.7
Elevation index error	P_b	-593.5

Table 4.3: Best fit parameters of the central feedhorn Pointing Model. Main contribution comes from the Azimuth index error, plus a significant contribute from non-perpendicularity.

Looking at the maps generated without pointing model correction (Figures 4.5-4.6 Left), we note as each source, Crab and Cas A, mainly appears in two different positions, this is reasonable because our telescope is following raster scanning patterns, i.e. it sweeps in Azimuth left-to-right at steady elevation, thus the telescope can detect the source crossing when it is rising and it is setting. Thus, roughly speaking, our model has to shift these two positions till they match in the nominal source locations. The seven corrections, as defined, are not independent, indeed we apply them in sequence, for example, the non-perpencularities correction is applied to the coordinates already corrected by the vertical flexure and roll-axis misalignment.
The conclusion to these two remarks is that we expect correlations between the seven parameter values, and a degeneracy of possible solutions to the pointing problem. Thus, the simple Chi-squared minimization, obtained with the described Monte Carlo simulations, is not enough to determine the accuracy of our model, because it could happen that the solution we have found is simple a local minimum in the solution space. We need an independent way to test our result.
The maps produced with the pointing model correction (Figures 4.5-4.6 Right) pro-

vide us the independent test we required, indeed, we can compute a 2-dimensional Gaussian fit to the maps and compare the $FWHM$ and ellipticity, defined as

$$e = 1 - \frac{FWHM_x}{FWHM_y} \tag{4.49}$$

of the fitted Gaussian with the instrumental beam

	α $[deg]$	δ $[deg]$	$FWHM_x$ $[deg]$	$FWHM_y$ $[deg]$	e
Crab	83.63	22.01	0.354	0.373	0.050
Cas A	350.85	58.82	0.362	0.384	0.054

Table 4.4: 2-dim Gaussian fit parameters of central horn maps. FWHM and ellipticity (4.49) are reported.

The $FWHM$ of the fitted Gaussian are in very good agreement with the beam $FWHM$ (Table 3.3) and the ellipticity is quite small, as we expected for our circular beam. Thus, we can claim that the seven pointing model parameters found with the previously described parameters estimation (Table 4.3) provide a good model for the second QUIJOTE telescope pointing and can be used for future map-making procedure.
In the following, we will show some plots and maps related to the central horn observations and simulation.

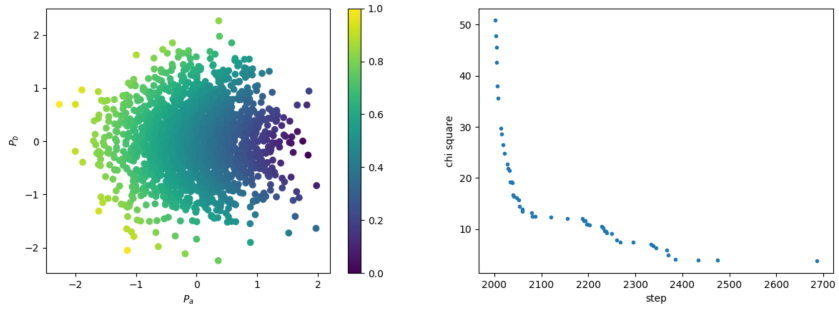

Figure 4.3: Monte Carlo simulation Results. Left: scatter plot of the first simulation, on the axis there are the two encoder index errors (P_a, P_b) and the points color is determined by the normalized Chi-squared. Right: plot of the second simulation, on the x-axis the simulation step number and on the y-axis the normalized Chi-squared.

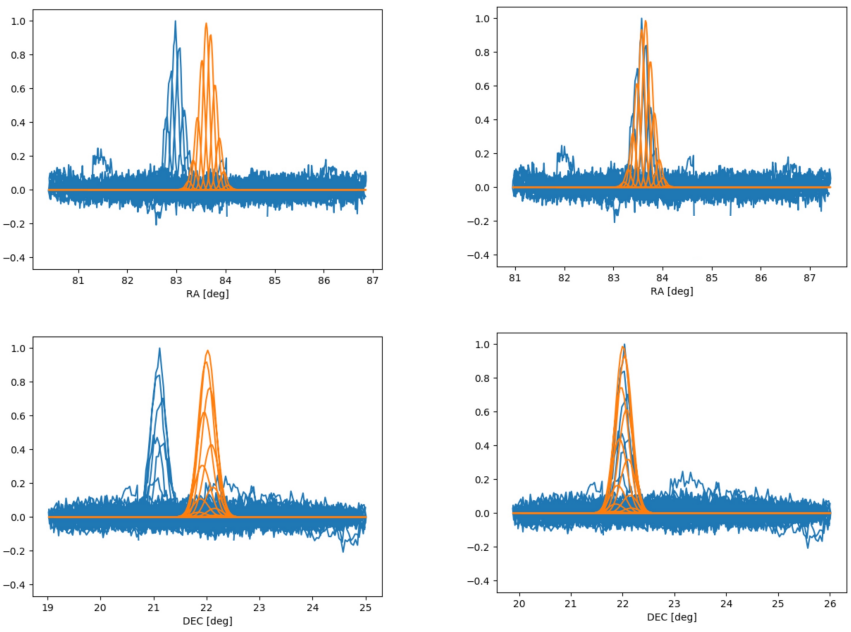

Figure 4.4: Real data (in blue) and ideal output (in orange) plots. Left: on the y-axis the real and ideal data, on the x-axis the right ascension (top) and declination (down) computed transforming the encoder horizon coordinates without the pointing model correction. Right: same as left, but with celestial coordinates computed transforming the encoder horizon coordinates applying the pointing model correction.

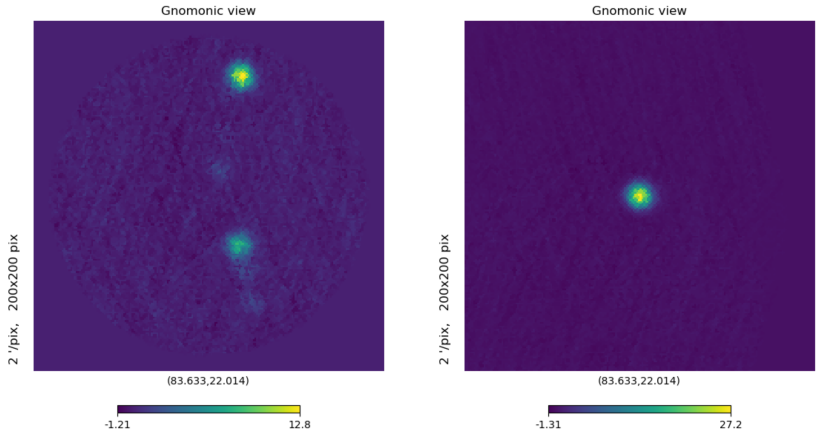

Figure 4.5: Central feedhorn maps of Crab co-adding all the 39 observations used for the simulation in the parameter estimation. Left: Map generated transforming horizon to celestial coordinates without the Pointing Model correction, two points are evident: the source raising and setting. Right: Map generated transforming the horizon coordinates with the Pointing Model correction; only one point at the source nominal position.

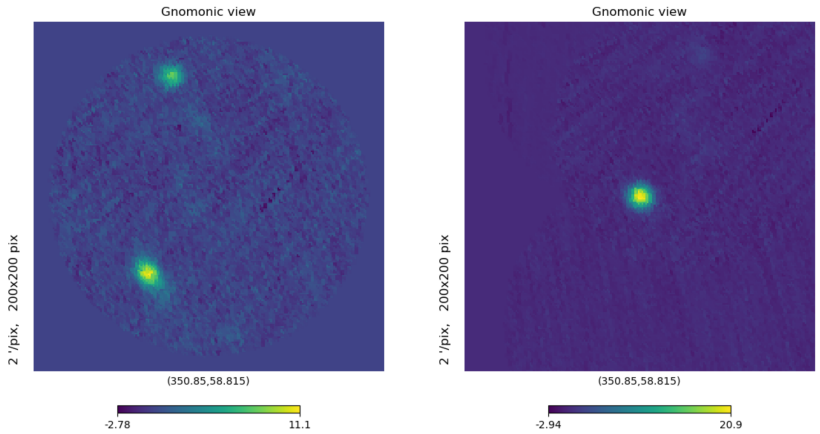

Figure 4.6: Central feedhorn maps of Cass A co-adding all the 25 observations used for the simulation in the parameter estimation. Left: Map generated transforming horizon to celestial coordinates without the Pointing Model correction, two points are evident: the source raising and setting. Right: Map generated transforming the horizon coordinates with the Pointing Model correction; only one point at the source nominal position.

Other horns

Concerning the pointing calibration of the other five feedhorns of the QT2, we have already discussed the two possible strategies: the first consists of using an unique Pointing Model, defined for the central horn, but corrected by the position of each horn in the focal plane, the second consists of finding a different Pointing Model per each horns. The maps in Figures 4.7 - 4.10 are suggesting that the first method, so a unique model, gives reasonable results, but to test the goodness of the model, further test are reacquired.

The first goodness test is given by the Chi-squared: we ran the parameters estimation procedure horn by horn. In this case, we ran only the second Monte Carlo simulation starting from the central horn pointing model (4.3) and slightly varying the seven parameters, which is a reasonable assumption because we expect small changes.

At the end, the simulations did not menage to find better solutions, showing as the parameters in Table 4.3 are already a minimum, at least local, in the solution space for all the six horns (Table 4.5).

	horn	χ^2	$FWHM_x$ [deg]	$FWHM_y$ [deg]	e
TGI	1	1.00	0.354	0.373	0.050
	2	1.01	0.361	0.381	0.052
	3	1.04	0.359	0.376	0.045
FGI	4	0.88	0.296	0.323	0.082
	5	1.07	0.269	0.318	0.153
	6	1.03	0.285	0.302	0.054

Table 4.5: Pointing Model results of the six feedhorns, The Chi-squared is normalized with respect to the consolidated chi squared of the central horn (Table 4.3). FWHM and ellipticity (4.49) are reported.

As for the central horn case, the simple Chi-squared test is not enough to test the goodness of our model, because of possible model degeneracy; thus, we computed a 2-dimensional Gaussian fit to the maps horn by horn, in Table 4.5 are reported the $FWHM$ values: the TGI's are in good agreement with the beam $FWHM$ and FGI's are a bit larger (Table 3.3).

The last column in Table 4.5 represents the ellipticity which plays an important role for the goodness of our model because we know the beam is circular with very good approximation. Thus, if the ellipticity is small, it means our model perfectly recovers the source, which should be unresolved. Looking at TGI results, the ellipticity is small for all the three feedhorns, instead, FGI results are very peculiar, *horn* 6 is in agreement with TGI's, *horn* 4 is slightly worse and *horn* 5 shows a quite large ellipticity.

However, it is important to mention that TGI observations are in general much better than FGI ones, thus, the source crossing is well distinguishable for the 30 GHz instrument and as consequence, Gaussian fit of TGI maps are more reliable, explaining the difference in the results.

The values refereed to *Cas A* observations are not reported because this source is much less bright than *Crab*, therefore it is difficult to find observations where the source crossing is well distinguishable for all the six *horns*, but from a rough estimation, the results seems compatible with the ones found for *Crab*.

In the following, we will show some the maps for each feedhorn, generated with and without the Pointing Model correction.

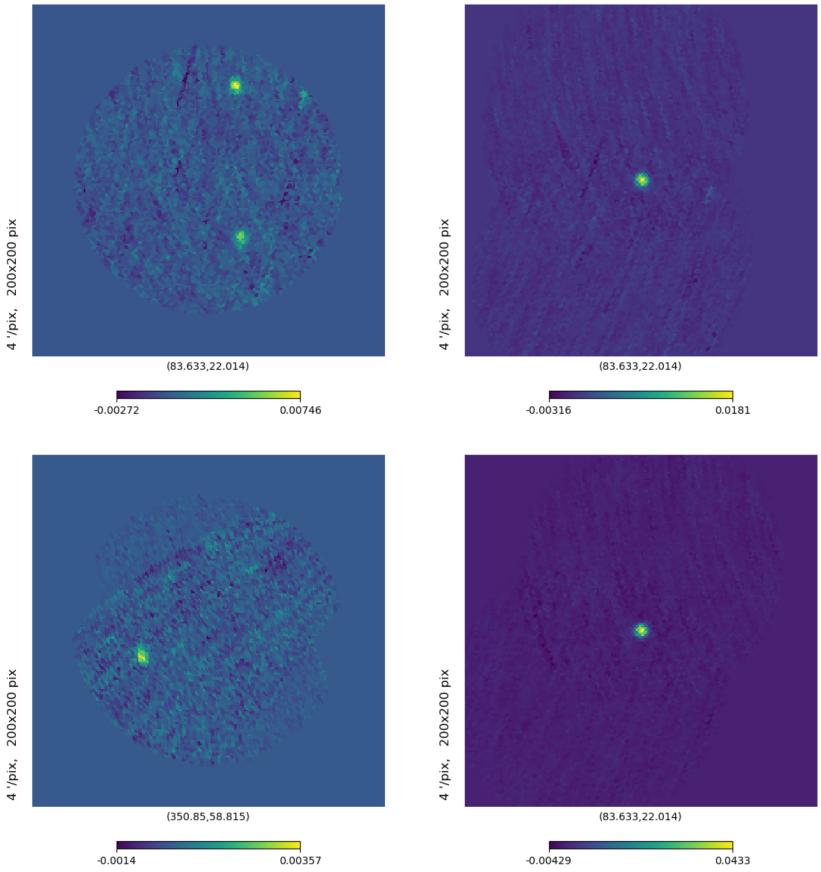

Figure 4.7: TGI horn 2 (top) and horn 3 (bottom) maps of Crab co-adding all the observations used for the simulation in the parameter estimation. Left: Map generated transforming horizon to celestial coordinates without the Pointing Model correction. Right: Map generated with the Pointing Model correction.

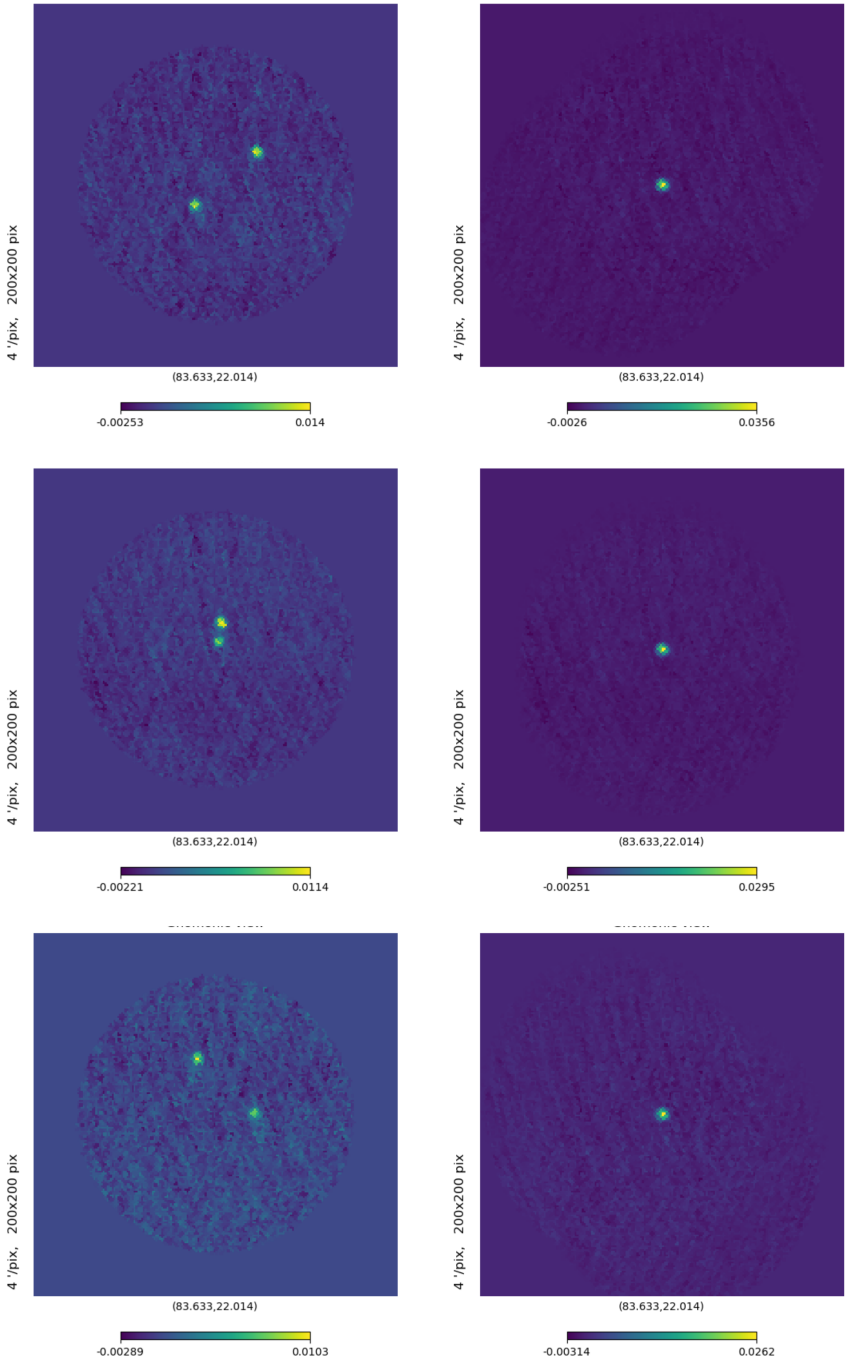

Figure 4.8: FGI horn 4 (top), horn 5 (middle) and horn 6 (bottom) maps of Crab co-adding all the observations used for the simulation in the parameter estimation. Left: Map generated transforming horizon to celestial coordinates without the Pointing Model correction. Right: Map generated with the Pointing Model correction.

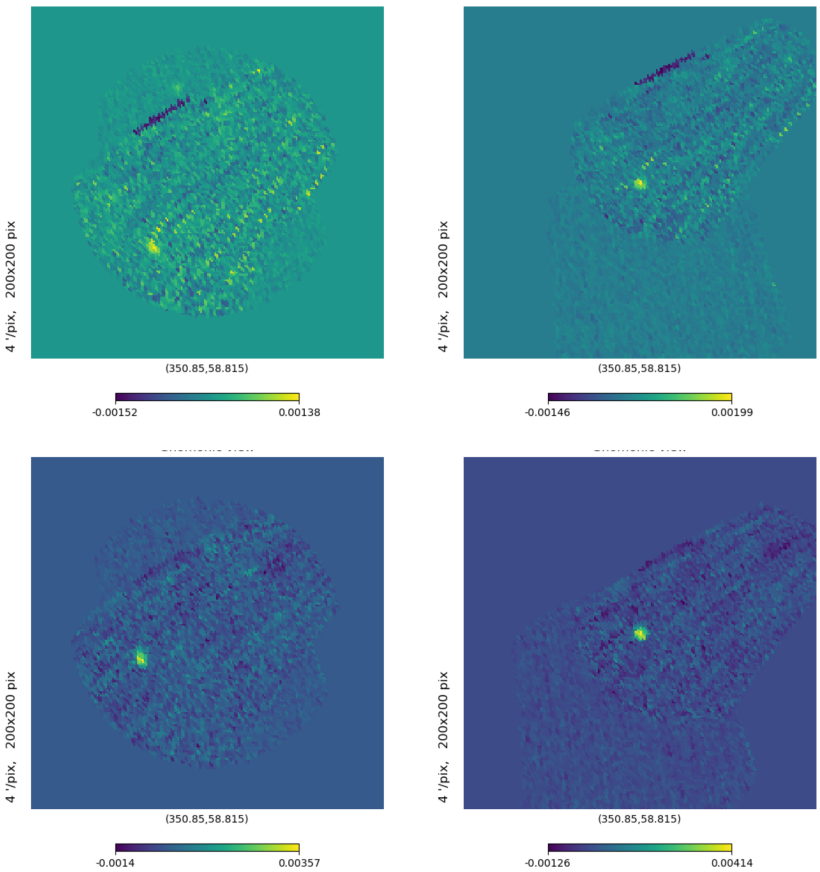

Figure 4.9: TGI horn 2 (top) and horn 3 (bottom) maps of Cass A co-adding all the observations used for the simulation in the parameter estimation. Left: Map generated transforming horizon to celestial coordinates without the Pointing Model correction. Right: Map generated with the Pointing Model correction.

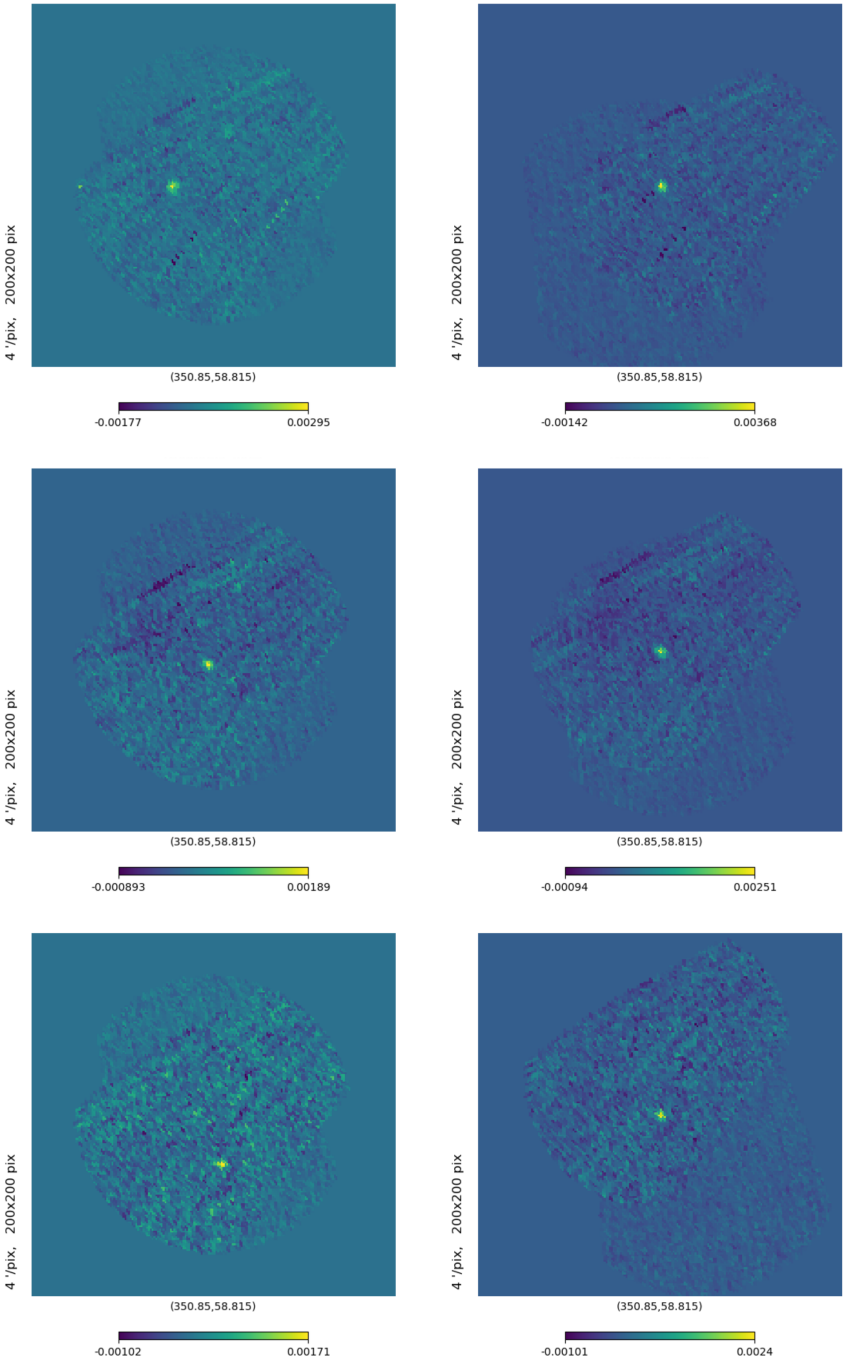

Figure 4.10: FGI horn 4 (top), horn 5 (middle) and horn 6 (bottom) maps of Cass A co-adding all the observations used for the simulation in the parameter estimation. Left: Map generated transforming horizon to celestial coordinates without the Pointing Model correction. Right: Map generated with the Pointing Model correction.

Chapter 5

The Instrumental Response of the QUIJOTE TFGI

The aim of the *QUIJOTE* instruments is to measure the polarization of the CMB. The polarization modulation for the Thirty and Forty instruments is obtained by combining two phase-switches, each of them having two different possible phase states. High frequency modulation allows to get almost simultaneous measurements of I, Q and U on the sky. In the following, we will present the full ideal instrumental response of the two instruments, moreover, a detailed discussion about non-idealities that could occur and how they affect outputs and measurements.

5.1 Ideal Response

The general TGI channel instrument scheme, reported in Figure 5.1, shows all the electric element at which the light signal pass through from its detection in the feed-horn till his digital lecture. In this section we will compute the ideal output of the instrument with the help of the *Jones formalism*. We will represent the input polarized light by a Jones vector and the linear optical elements by Jones matrices.
We take as input signal a monochromatic electromagnetic plane wave travelling in the positive z-direction, which we impose to be the instrument direction, as

$$\mathbf{E}_{in} = \begin{pmatrix} \mathcal{E}_1 \\ \mathcal{E}_2 \end{pmatrix} \tag{5.1}$$

where $\mathcal{E}_1$, $\mathcal{E}_2$ are in general complex numbers.

Ideal Elements
In the following, we will introduce all the elements which compose the TGI channel response, moreover, for each component we will give the associated ideal Jones matrix.

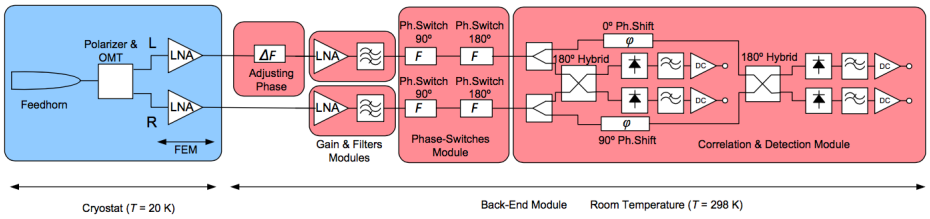

Figure 5.1: TGI ideal channel response scheme

- *Polarizer*
  A beam-splitter linear polarizer is an optical filter, where the unpolarized beam is split into two beams with opposite polarization states. It consists of a 90° retarder in the y-component, rotated of 45° with respect to the axes of the OMT. The associated Jones matrix is computed by the product of three matrices: the two rotational matrices and the retarder Jones matrix

$$\begin{aligned}\mathbf{J}_{Pol} &= \mathcal{R}(\pi/4)\ \mathbf{J}_{Ret}(\pi)\ \mathcal{R}^{-1}(\pi/4) \\ &= \frac{1}{2}\begin{pmatrix}1 & -1\\ 1 & 1\end{pmatrix}\begin{pmatrix}1 & 0\\ 0 & i\end{pmatrix}\begin{pmatrix}1 & 1\\ -1 & 1\end{pmatrix} = \frac{1}{2}\begin{pmatrix}1+i & 1-i\\ 1-i & 1+i\end{pmatrix}.\end{aligned} \tag{5.2}$$

- *OMT*
  The Orthomode Transducer is a waveguide component and serves in general either to combine or to separate two orthogonally polarized microwave signal paths. OMTs are used with feedhorns, as in our case, to isolate orthogonal polarizations. We suppose its Jones matrix ideally behaves simply as an identity matrix

$$\mathbf{J}_{OMT} = \begin{pmatrix}1 & 0\\ 0 & 1\end{pmatrix}. \tag{5.3}$$

- *Adjusting Phase*
  An Adjusting Phase is a circuit element with the aim, as the name suggest, to adjust the phase signal. Ideally, it adds a phase ΔF to one branch and leave unchanged the other, thus the associated Jones matrix would be a diagonal

$$\mathbf{J}_{Adj.Ph} = \begin{pmatrix}e^{i\Delta F} & 0\\ 0 & 1\end{pmatrix}. \tag{5.4}$$

- *LNA*
  A Low-Noise Amplifier is an electronic amplifier that amplifies very low-power signals, without significantly degrading the signal-to-noise ratio. Ideally it behaves as a Gain module which add two independent amplitude factors to the two branches, thus the Jones matrix is diagonal

$$\mathbf{J}_{LNA} = \begin{pmatrix}g_1 & 0\\ 0 & g_2\end{pmatrix}. \tag{5.5}$$

- *Phase Switches*
  A Switch is an electrical component that can "make" or "break" an electric activity, in our case we have four switches, two per branch. When one on them

is on, it adds a known phase to the branch it is connect. We call $\phi_1 = 0\,/\,180°$ the one on top right, $\phi_2 = 0\,/\,90°$ on top left, $\varphi_1 = 0\,/\,180°$ on bottom right and $\varphi_2 = 0\,/\,90°$ on bottom left. Moreover, we can sum up in twos, in order to deal only with two phases: $\phi = \phi_1 + \phi_2$ and $\varphi = \varphi_1 + \varphi_2$, in the Jones matrix formalism

$$\mathbf{J}_{Ph.Sw} = \begin{pmatrix} e^{i\phi} & 0 \\ 0 & e^{i\varphi} \end{pmatrix}. \tag{5.6}$$

- 180°-*hybrid*
  The 180°-hybrid is a directional couplers which takes as input the beams from the two branches and returns as output other two beams, one giving the sum and the other the difference of the initial beams. In terms of Jones matrices it has inverse off-diagonal elements and ideally it is normalized to one

$$\mathbf{J}_{hyb} = \frac{1}{\sqrt{2}} \begin{pmatrix} 1 & 1 \\ -1 & 1 \end{pmatrix}. \tag{5.7}$$

Response Computation

According to Jones calculus, when light crosses an optical element the resulting polarization of the light is found by taking the product of the Jones matrix of the optical element and the Jones vector of the incident light. Thus, in principle, we can compute the output signal directly by mean of the matrix product

$$\mathbf{E}_{fin} = \mathbf{J}_{TGI}\ \mathbf{E}_{in} \tag{5.8}$$

where $\mathbf{J}_{TGI}$ can be seen as the Jones matrix associated to the full system in Figure 5.1. It is obtained by the product of all the Jones matrices just presented, thus, we can write equation (5.8) as

$$\mathbf{E}_{fin} = \mathbf{J}_{hyb}\ \mathbf{J}_{Ph.Sw}\ \mathbf{J}_{LNA}\ \mathbf{J}_{Adj.Ph}\ \mathbf{J}_{OMT}\ \mathbf{J}_{Pol}\ \mathbf{E}_{in} \tag{5.9}$$

although this is the fastest way, we prefer to proceed step by step, multiplying each Jones matrix to the light vector, because this turns out to be much simpler.
First, we compute the output signal resulting after the first elements, the Polarizer and OMT, by mean of the product of their matrices and the input signal, and we call it $\mathbf{E}'$

$$\begin{aligned} \mathbf{E}' &= \mathbf{J}_{OMT}\ \mathbf{J}_{pol}\ \mathbf{E}_{in} \\ &= \frac{1}{2} \begin{pmatrix} 1 & 0 \\ 0 & 1 \end{pmatrix} \begin{pmatrix} 1+i & 1-i \\ 1-i & 1+i \end{pmatrix} \begin{pmatrix} \mathcal{E}_1 \\ \mathcal{E}_2 \end{pmatrix} = \frac{1}{2} \begin{pmatrix} (1+i)\mathcal{E}_1 + (1-i)\mathcal{E}_2 \\ (1-i)\mathcal{E}_1 + (1+i)\mathcal{E}_2 \end{pmatrix} \end{aligned} \tag{5.10}$$

the rotation in equation (5.2) is the cause of the shuffle between the two initial components $\mathcal{E}_1$, $\mathcal{E}_2$ in the resulting vector $\mathbf{E}'$.
Then, we consider the next elements: Adjusting Phase, LNA and Phase Switches, which have diagonal Jones matrices, therefore, they add different amplitudes and phases at the two components independently. We call the resulting signal $\mathbf{E}$, in order to simplify further computations

$$\begin{aligned} \mathbf{E} &= \mathbf{J}_{Ph.Sw}\ \mathbf{J}_{LNA}\ \mathbf{J}_{Adj.Ph}\ \mathbf{E}' \\ &= \frac{1}{2} \begin{pmatrix} e^{i\phi} & 0 \\ 0 & e^{i\varphi} \end{pmatrix} \begin{pmatrix} g_1 & 0 \\ 0 & g_2 \end{pmatrix} \begin{pmatrix} e^{i\Delta F} & 0 \\ 0 & 1 \end{pmatrix} \begin{pmatrix} (1+i)\mathcal{E}_1 + (1-i)\mathcal{E}_2 \\ (1-i)\mathcal{E}_1 + (1+i)\mathcal{E}_2 \end{pmatrix} \\ &= \frac{1}{2} \begin{pmatrix} g_1 e^{i(\Delta F+\phi)}[(1+i)\mathcal{E}_1 + (1-i)\mathcal{E}_2] \\ g_2 e^{i\varphi}[(1-i)\mathcal{E}_1 + (1+i)\mathcal{E}_2] \end{pmatrix} = \begin{pmatrix} E_1 \\ E_2 \end{pmatrix}. \end{aligned} \tag{5.11}$$

Last element is the 180°-hybrid, which shuffles again the two components, the final result for the output vector of the two internal branches

$$\begin{aligned}\mathbf{E}_{fin} &= \mathbf{J}_{hyb}\ \mathbf{E} \\ &= \frac{1}{2\sqrt{2}}\begin{pmatrix}1 & 1\\ -1 & 1\end{pmatrix}\begin{pmatrix}E_1\\ E_2\end{pmatrix} = \frac{1}{2\sqrt{2}}\begin{pmatrix}E_1+E_2\\ E_1-E_2\end{pmatrix} \\ &= \frac{1}{2\sqrt{2}}\begin{pmatrix}g_1 e^{i(\Delta F+\phi)}[(1+i)\mathcal{E}_1+(1-i)\mathcal{E}_2] \ + \ g_2 e^{i\varphi}[(1-i)\mathcal{E}_1+(1+i)\mathcal{E}_2]\\ g_1 e^{i(\Delta F+\phi)}[(1+i)\mathcal{E}_1+(1-i)\mathcal{E}_2] \ - \ g_2 e^{i\varphi}[(1-i)\mathcal{E}_1+(1+i)\mathcal{E}_2]\end{pmatrix}.\end{aligned} \tag{5.12}$$

To compute the vector of the final external output, we also have to take into account the effects of other two Phase Shifts, which simply add two independent phases at the two branches. However, the result is quite the same, thus, we skip the computation and we will present the results at the end.
So far, we have computed the final ideal Jones vector, which is in general complex, but, in reality, what we measure are real quantities as electrical potentials, thus, let focus only on one output, that we call $\mathbf{V_{d1}}$. It is given by the module squared of the first component of $\mathbf{E}_{fin}$

$$\mathbf{V_{d1}} = \frac{1}{8}|E_1+E_2|^2 = \frac{1}{8}[E_1E_1^* + E_1E_2^* + E_1^*E_2 + E_2E_2^*] \tag{5.13}$$

in the following we explain all the individual products

$$\begin{aligned}E_1E_1^* &= g_1^2\ [(1+i)\mathcal{E}_1+(1-i)\mathcal{E}_2]\ [(1-i)\mathcal{E}_1^*+(1+i)\mathcal{E}_2^*] \\ &= 2g_1^2\ (\mathcal{E}_1\mathcal{E}_1^* + i\mathcal{E}_1\mathcal{E}_2^* - i\mathcal{E}_1^*\mathcal{E}_2 + \mathcal{E}_2\mathcal{E}_2^*) \\ E_1E_2^* &= g_1g_2\ e^{i\delta}\ [(1+i)\mathcal{E}_1+(1-i)\mathcal{E}_2]\ [(1+i)\mathcal{E}_1^*+(1-i)\mathcal{E}_2^*] \\ &= 2g_1g_2\ e^{i\delta}\ (i\mathcal{E}_1\mathcal{E}_1^* + \mathcal{E}_1\mathcal{E}_2^* + \mathcal{E}_1^*\mathcal{E}_2 - i\mathcal{E}_2\mathcal{E}_2^*) \\ E_1^*E_2 &= g_1g_2\ e^{-i\delta}\ [(1-i)\mathcal{E}_1^*+(1+i)\mathcal{E}_2^*]\ [(1-i)\mathcal{E}_1+(1+i)\mathcal{E}_2] \\ &= 2g_1g_2\ e^{-i\delta}\ (-i\mathcal{E}_1\mathcal{E}_1^* + \mathcal{E}_1\mathcal{E}_2^* + \mathcal{E}_1^*\mathcal{E}_2 + i\mathcal{E}_2\mathcal{E}_2^*) \\ E_2E_2^* &= g_2^2\ [(1-i)\mathcal{E}_1+(1+i)\mathcal{E}_2]\ [(1+i)\mathcal{E}_1^*+(1-i)\mathcal{E}_2^*] \\ &= 2g_2^2\ (\mathcal{E}_1\mathcal{E}_1^* - i\mathcal{E}_1\mathcal{E}_2^* + i\mathcal{E}_1^*\mathcal{E}_2 + \mathcal{E}_2\mathcal{E}_2^*)\end{aligned} \tag{5.14}$$

we called $\delta = \phi - \varphi + \Delta F$ which is the only phase in the results. This is suggesting us that at the end the output will only depends on the difference between the phases of the upper branch (ϕ) and the bottom branch (φ).
The resulting potential is a complex function of the initial signal components $\mathcal{E}_1$, $\mathcal{E}_2$, the phase δ and the amplitudes g_1,g_2

$$\begin{aligned}\mathbf{V_{d1}} = \frac{1}{4}\ &[(g_1^2+g_2^2)\ (\mathcal{E}_1\mathcal{E}_1^*+\mathcal{E}_2\mathcal{E}_2^*)\ +\ i(g_1^2-g_2^2)\ (\mathcal{E}_1\mathcal{E}_2^*-\mathcal{E}_1^*\mathcal{E}_2)\ + \\ &ig_1g_2(e^{i\delta}-e^{-i\delta})(\mathcal{E}_1\mathcal{E}_1^*-\mathcal{E}_2\mathcal{E}_2^*)\ +\ g_1g_2(e^{i\delta}+e^{-i\delta})(\mathcal{E}_1\mathcal{E}_2^*+\mathcal{E}_1^*\mathcal{E}_2)].\end{aligned} \tag{5.15}$$

Despite the intricate shape, the output is simply physically understood, it can be written as

$$\mathbf{V_{d1}} = \frac{1}{2}\Big[\frac{g_1^2+g_2^2}{2}\mathbf{I} - \frac{g_1^2-g_2^2}{2}\mathbf{V} - g_1g_2\mathbf{Q}\sin\delta + g_1g_2\mathbf{U}\cos\delta\Big]. \tag{5.16}$$

where we used the Stokes parameters definitions

$$\begin{aligned}\mathbf{I} &= \mathcal{E}_1\mathcal{E}_1^* + \mathcal{E}_2\mathcal{E}_2^* \\ \mathbf{Q} &= \mathcal{E}_1\mathcal{E}_1^* - \mathcal{E}_2\mathcal{E}_2^* \\ \mathbf{U} &= \mathcal{E}_1\mathcal{E}_2^* + \mathcal{E}_1^*\mathcal{E}_2 \\ \mathbf{V} &= -i(\mathcal{E}_1\mathcal{E}_2^* - \mathcal{E}_1^*\mathcal{E}_2)\end{aligned} \tag{5.17}$$

and the relations between the trigonometric functions, cosine and sine, and the exponential function

$$\begin{aligned}\cos x &= \Re(e^{ix}) = \frac{e^{ix} + e^{-ix}}{2} \\ \sin x &= \Im(e^{ix}) = \frac{e^{ix} - e^{-ix}}{2i}.\end{aligned} \tag{5.18}$$

TGI Ideal Output

The output in equation (5.16) is a combination of the four Stokes parameters which describe the input signal. The main contribution comes from the amplitude $\mathbf{I}$, a small attenuation is present in case of not-null vorticity $\mathbf{V}$ and finally the output get a contribution from the Stokes $\mathbf{Q}$ and $\mathbf{U}$, in case of polarized input signal.
All the other output signals can be easily computed using the same recipe, the results are very similar, the part concerning the amplitude and vorticity is invariant, instead the factor in front of the Stokes parameters $\mathbf{Q}$ and $\mathbf{U}$ change

$$\begin{aligned}\mathbf{V_{d1}} &= \frac{1}{2}\Big[\frac{g_1^2+g_2^2}{2}\mathbf{I} - \frac{g_1^2-g_2^2}{2}\mathbf{V} - g_1g_2\mathbf{Q}\sin\delta + g_1g_2\mathbf{U}\cos\delta\Big]. \\ \mathbf{V_{d2}} &= \frac{1}{2}\Big[\frac{g_1^2+g_2^2}{2}\mathbf{I} - \frac{g_1^2-g_2^2}{2}\mathbf{V} + g_1g_2\mathbf{Q}\sin\delta - g_1g_2\mathbf{U}\cos\delta\Big] \\ \mathbf{V_{d3}} &= \frac{1}{2}\Big[\frac{g_1^2+g_2^2}{2}\mathbf{I} - \frac{g_1^2-g_2^2}{2}\mathbf{V} + g_1g_2\mathbf{Q}\sin\delta + g_1g_2\mathbf{U}\cos\delta\Big] \\ \mathbf{V_{d4}} &= \frac{1}{2}\Big[\frac{g_1^2+g_2^2}{2}\mathbf{I} - \frac{g_1^2-g_2^2}{2}\mathbf{V} - g_1g_2\mathbf{Q}\sin\delta - g_1g_2\mathbf{U}\cos\delta\Big].\end{aligned} \tag{5.19}$$

FGI Ideal Output

The FGI instrument scheme, reported in Figure 5.2, is very similar to the TGI's one, the are only two differences: (i) a second Adjusting Phase in the second block and (ii) in the final part, there are two 90°-*hybrid* instead of one 180°-*hybrid* which shuffle the output signals keeping the form invariant. Therefore, at the end the output are the same

$$\begin{aligned}\mathbf{V_{d1}}^{FGI} &= \frac{1}{2}\Big[\frac{g_1^2+g_2^2}{2}\mathbf{I} - \frac{g_1^2-g_2^2}{2}\mathbf{V} + g_1g_2\mathbf{Q}\sin\delta + g_1g_2\mathbf{U}\cos\delta\Big] = \mathbf{V_{d3}}^{TGI} \\ \mathbf{V_{d2}}^{FGI} &= \frac{1}{2}\Big[\frac{g_1^2+g_2^2}{2}\mathbf{I} - \frac{g_1^2-g_2^2}{2}\mathbf{V} - g_1g_2\mathbf{Q}\sin\delta - g_1g_2\mathbf{U}\cos\delta\Big] = \mathbf{V_{d4}}^{TGI} \\ \mathbf{V_{d3}}^{FGI} &= \frac{1}{2}\Big[\frac{g_1^2+g_2^2}{2}\mathbf{I} - \frac{g_1^2-g_2^2}{2}\mathbf{V} + g_1g_2\mathbf{Q}\sin\delta - g_1g_2\mathbf{U}\cos\delta\Big] = \mathbf{V_{d2}}^{TGI} \\ \mathbf{V_{d4}}^{FGI} &= \frac{1}{2}\Big[\frac{g_1^2+g_2^2}{2}\mathbf{I} - \frac{g_1^2-g_2^2}{2}\mathbf{V} - g_1g_2\mathbf{Q}\sin\delta + g_1g_2\mathbf{U}\cos\delta\Big] = \mathbf{V_{d1}}^{TGI}\end{aligned} \tag{5.20}$$

where we have a slightly different definition of δ which now includes both the adjusting phases. In the following sections, we will continue to refer to the TGI output, but as equations (5.20) suggest, the same arguments apply to the FGI as well.

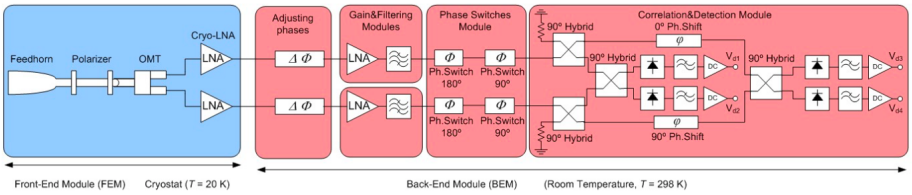

Figure 5.2: FGI ideal channel response scheme

5.2 Measuring Stokes parameters

Let us take the third TGI output, which is the simpler, but keeping in mind that the treatment we will present in this section is perfectly suitable for the other three TGI outputs and the four FGI outputs. We have

$$\mathbf{V_{d3}} = \frac{1}{2}\Big[\frac{g_1^2+g_2^2}{2}\mathbf{I} - \frac{g_1^2-g_2^2}{2}\mathbf{V} + g_1 g_2 \mathbf{Q}\sin\delta + g_1 g_2 \mathbf{U}\cos\delta\Big]. \tag{5.21}$$

The factors in front of the intensity $\mathbf{I}$ and $\mathbf{V}$ only depend on the gains introduced by the LNA elements, which in principle are fixed. Instead, the factors in front of the Stokes $\mathbf{Q}$ and $\mathbf{U}$ still depend on the gains but also on trigonometric function of the angle δ. Thus, the final contribution of $\mathbf{Q}$ and $\mathbf{U}$ in the output depends on the values of ϕ and φ, so on the states of the four phase switches.

Phase States

Our system is composed by four phase switches, each switch has two states: off and on (0/1), thus, in principle, the full system has $2^4 = 16$ states, i.e. all the possible combinations of the switch states, which we call *input states* (Table 5.1);

Binary	ϕ_1 [°]	ϕ_2 [°]	φ_1 [°]	φ_2 [°]	δ [°]	$\sin(\delta)$	$\cos(\delta)$
0000	0	0	0	0	0	0	1
0001	0	0	0	90	270	-1	0
0010	0	0	180	0	180	0	-1
0011	0	0	180	90	90	1	0
0100	0	90	0	0	90	1	0
0101	0	90	0	90	0	0	1
0110	0	90	180	0	270	-1	0
0111	0	90	180	90	180	0	-1
1000	180	0	0	0	180	0	-1
1001	180	0	0	90	90	1	0
1010	180	0	180	0	0	0	1
1011	180	0	180	90	270	-1	0
1100	180	90	0	0	270	-1	0
1101	180	90	0	90	180	0	-1
1110	180	90	180	0	90	1	0
1111	180	90	180	90	0	0	1

Table 5.1: Input States. First column represents the digit combination, from second to fifth are reported the values of the switches, sixth to eighth represent the phase and trigonometric value of the combination angle defined in (5.22).

but we have seen that the final outputs only depends on sine and cosine of a specific combination of the four phases

$$\delta = \phi_1 + \phi_2 - \varphi_1 - \varphi_2 \tag{5.22}$$

we omit for simplicity the term ΔF. This lead to a degeneracy in the input states, indeed, the final output we measure have only four states, which we call *phase states* (Table 5.2).

δ °	$\sin(\delta)$	$\cos(\delta)$
0	0	1
90	1	0
180	0	-1
270	-1	0

Table 5.2: Phase States. The angle in first column is defined in (5.22)

Thus, with particular combinations of the switches states, we can set to zero the **Q** factor and to ± 1 the **U** factor, or vice versa, thus we can disentangle the **Q** and **U** contributions from the final output. The intensity **I** is not effected by the phase states and let forget from now on the **V** contribution, because we learned in second section that CMB has not significant vorticity.
Let consider a simplified version of the TGI output (5.21)

$$\mathbf{V_d}(\delta) = \frac{1}{2}\Big[\mathbf{I} + \mathbf{Q}\sin\delta + \mathbf{U}\cos\delta\Big] \tag{5.23}$$

it simply depends on δ, thus, it can be directly the output $\mathbf{V_{d3}}$ in one of the 16 input states in Table 5.1, or it can be computed taking the average value of the 4 states,

from the 16, which lead at the same value of δ. For example, for the phase state associated to $\delta = 0$, we can consider the two outputs

$$\begin{aligned}\mathbf{A_1}(\delta = 0) &= \mathbf{V_{d3}}(0,0,0,0) \\ \mathbf{A_4}(\delta = 0) &= \frac{1}{4}\big[\mathbf{V_{d3}}(0,0,0,0) + \mathbf{V_{d3}}(0,1,0,1) \\ &\quad + \mathbf{V_{d3}}(1,0,1,0) + \mathbf{V_{d3}}(1,1,1,1)\big].\end{aligned} \tag{5.24}$$

which, in the ideal case, are completely equivalent. Differences will arise in the second section when we will consider possible non-idealities and offset errors.

The Stokes Parameters
Considering the simplified TGI output $\mathbf{V_d}$ 5.23), playing with different phase states, we can compute the intensity $\mathbf{I}$ and the Stokes parameters $\mathbf{Q}$ and $\mathbf{U}$ of the input signal $\mathbf{E}_{in}$ (5.1)

$$\begin{aligned}\mathbf{I}_1 &= \mathbf{A_i}(0^\circ) + \mathbf{A_i}(180^\circ) \\ \mathbf{I}_2 &= \mathbf{A_i}(90^\circ) + \mathbf{A_i}(270^\circ) \\ \mathbf{Q} &= \mathbf{A_i}(0^\circ) - \mathbf{A_i}(180^\circ) \\ \mathbf{U} &= \mathbf{A_i}(90^\circ) - \mathbf{A_i}(270^\circ)\end{aligned} \tag{5.25}$$

where $i = 1, 4$, $\mathbf{I}_1$ and $\mathbf{I}_2$ are two independent measure of the amplitude, which combination gives an unique value for the amplitude $\mathbf{I}$. The total intensity of polarization $\mathbf{P}$ and the rotation angle γ are then computed as

$$\begin{aligned}\mathbf{I} &= (\mathbf{I}_1 + \mathbf{I}_2)/2 \\ \mathbf{P} &= \sqrt{\mathbf{Q}^2 + \mathbf{U}^2} \\ \gamma &= \frac{1}{2}\arctan\Big(\frac{\mathbf{U}}{\mathbf{Q}}\Big).\end{aligned} \tag{5.26}$$

In these simple equations is showed the power of this channel response system: with four phase switches and some optical elements, we can have a direct measurement of the intensity and polarization of the CMB.

5.3 Non-Idealities

In the first section we presented the ideal channel response of the QUIJOTE Thirty and Forty GHz Instruments, but, as experience teaches us, reality is much more complex. In this section, we show some of the possible non-idealities which can effect the instrumens responses. To do so, we will generalize some Jones matrices and add some extra gains or extra phases to the ones already presented. Thus, we must overcome the analytic version and proceed with the numerical calculation by mean of computer simulated responses.
For clarify, we call $\mathbf{I}$, $\mathbf{Q}$, $\mathbf{U}$ and so on, the real parameters of the input signal and $\mathbf{I}'$, $\mathbf{Q}'$, $\mathbf{U}'$ and so on, the parameters as measured by our instruments. Moreover, we will show in the plots y-axis the difference in percentage between them, defined as

$$y_{\mathbf{X}} = \frac{\mathbf{X} - \mathbf{X}'}{\mathbf{X}}\ [\%] \tag{5.27}$$

where $\mathbf{X} = \mathbf{I}$, $\mathbf{Q}$, $\mathbf{U}$, $\mathbf{P}$ or $\mathbf{P/I}$. Only for the rotation angle we will present the simple difference $\gamma - \gamma'$ in degrees.
During the analysis, we will consider as input signal a polarized wave $\mathbf{E}_{in} = (0.92, 0.32)$, whose Stokes parameter values are

I	**Q**	**U**	**P**	**P/I**	γ
1.00	0.69	0.72	1.00	1.00	23.08°

and we will study the difference between the real and measured parameters when the following non-idealities to the system are present:

- Phase Switches offsets
- LNA gains difference
- 180-hybrid offsets and gains
- Polarizer offsets.

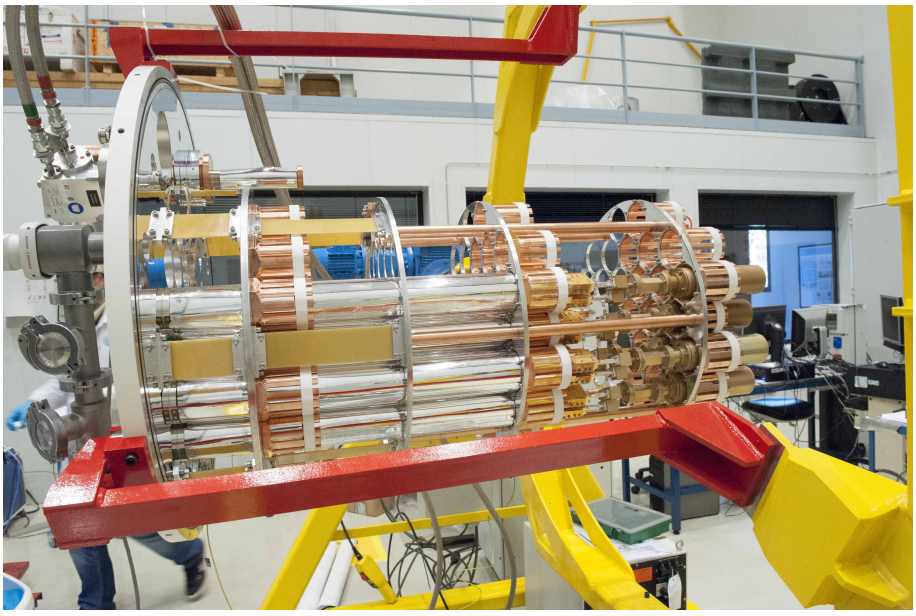

Figure 5.3: The second QUIJOTE Instrument, the TGI.

Phase Switches offsets

Each phase switch has been designed to add a fixed phase to the signal when it is on and leave the signal unchanged when it is off. However, it could happen that the phase the switch adds, when on or off, is not the one required.
Let focus on the first and third phase switches: ideally, $\phi_1 = 0$ when the switch is off and is equal to 180° when the switch is on, exactly the same happen for φ_1. Two kind of non-idealities could occur

- The phase ϕ_1 is not exactly 180° when the switch is on, but, still $\phi_1 = 0$ when the switch is off. Thus the Jones matrix shape is unchanged

$$\mathbf{J}_{Ph.Sw} = \begin{pmatrix} e^{i(\phi_1+\phi_2)} & 0 \\ 0 & e^{i(\varphi_1+\varphi_2)} \end{pmatrix} \tag{5.28}$$

  but, a angular shift $\epsilon \in [-5°, 5°]$ is present when the first switch is on.

switch	ϕ_1 [°]	ϕ_2 [°]	φ_1 [°]	φ_2 [°]
off	0	0	0	0
on	180 + ϵ	90	180	90

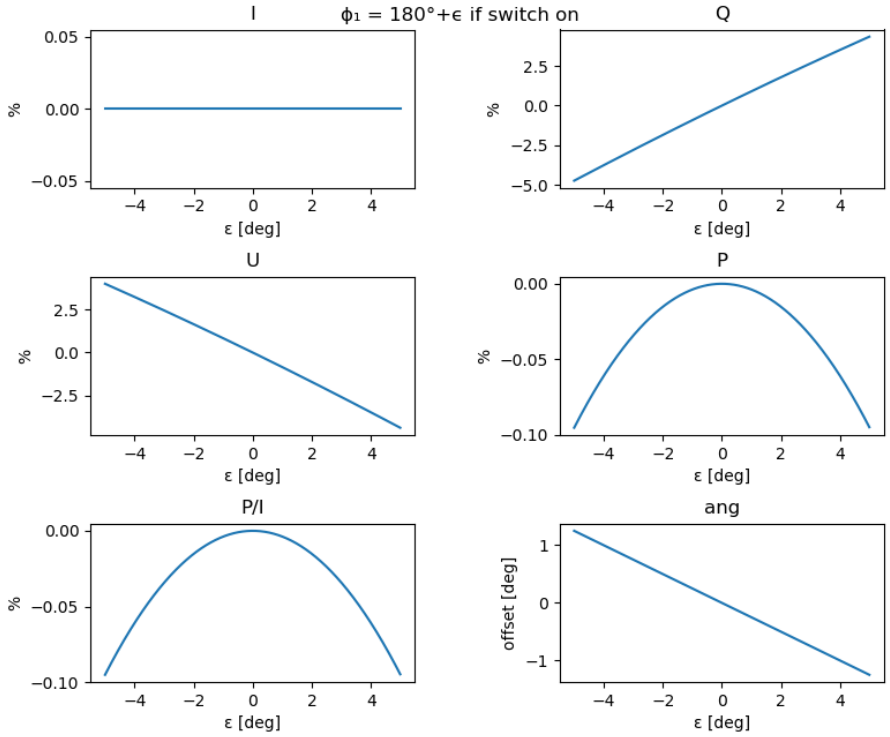

Figure 5.4: Small offset in the first phase switch when on.

An offset in one of the phase switch does not effect the measured intensity, as we expected by the output equations (5.19). The Stokes, Q and U change almost linearly with the offset, but inversely with respect to each other, because Q and

U are exchanging power to each other. As result, the polarization intensity is a little reduced, instead, the polarization angle decreases almost linearly with the offset, an offset of 4 degrees lead to and angle error of about 1 degree.

- The phase ϕ_1 is not exactly 180° when the switch is on and it is not exactly 0° when the switch is off, supposing both suffer from a same offset. The Jones matrix is still unchanged

$$\mathbf{J}_{Ph.Sw} = \begin{pmatrix} e^{i(\phi_1+\phi_2)} & 0 \\ 0 & e^{i(\varphi_1+\varphi_2)} \end{pmatrix} \tag{5.29}$$

but, a angular shift $\epsilon \in [-5°, 5°]$ is present when the first switch is on and off.

switch	ϕ_1 [°]	ϕ_2 [°]	φ_1 [°]	φ_2 [°]
off	$0 + \epsilon$	0	0	0
on	$180 + \epsilon$	90	180	90

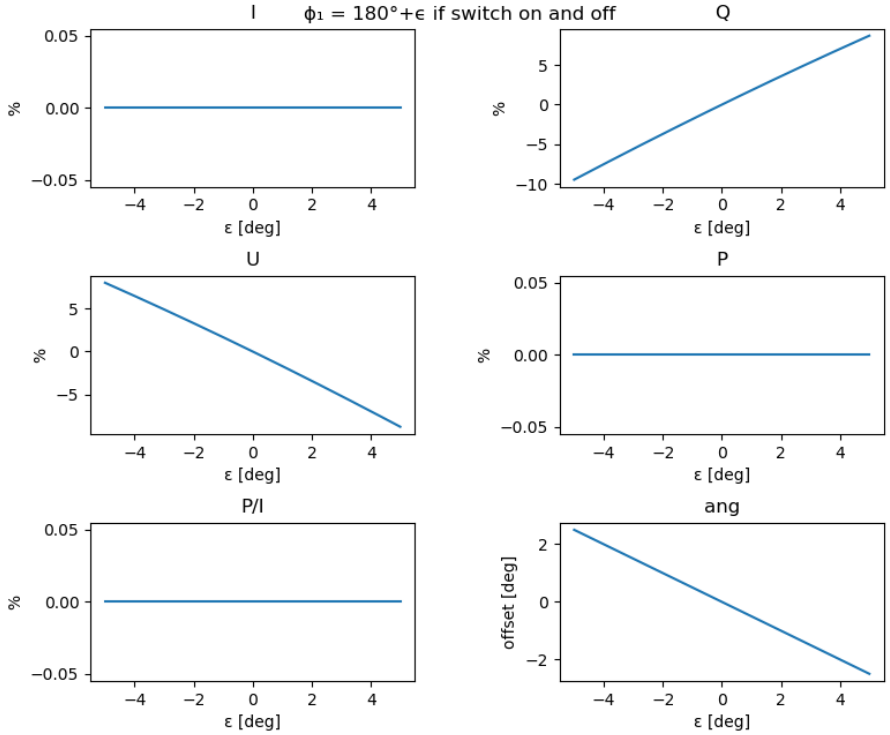

Figure 5.5: Small offset in the first phase switch when on and off.

Almost same argument as for the previous case, the intensity is unchanged, Q and U exchange power, but P is not effected, and the angle linearly increase with the offset.

- The phases ϕ_1 and φ_1 are not exactly 180° when the switches are on, but, still $\phi_1 = \varphi_1 = 0$ when the switches are off, supposing both suffer from a same offset. The Jones matrix shape is still unchanged

$$\mathbf{J}_{Ph.Sw} = \begin{pmatrix} e^{i(\phi_1+\phi_2)} & 0 \\ 0 & e^{i(\varphi_1+\varphi_2)} \end{pmatrix} \tag{5.30}$$

but, a angular shift $\epsilon \in [-5°, 5°]$ is present when the first and third switches are on.

switch	ϕ_1 [°]	ϕ_2 [°]	φ_1 [°]	φ_2 [°]
off	0	0	0	0
on	180 + ϵ	90	180 + ϵ	90

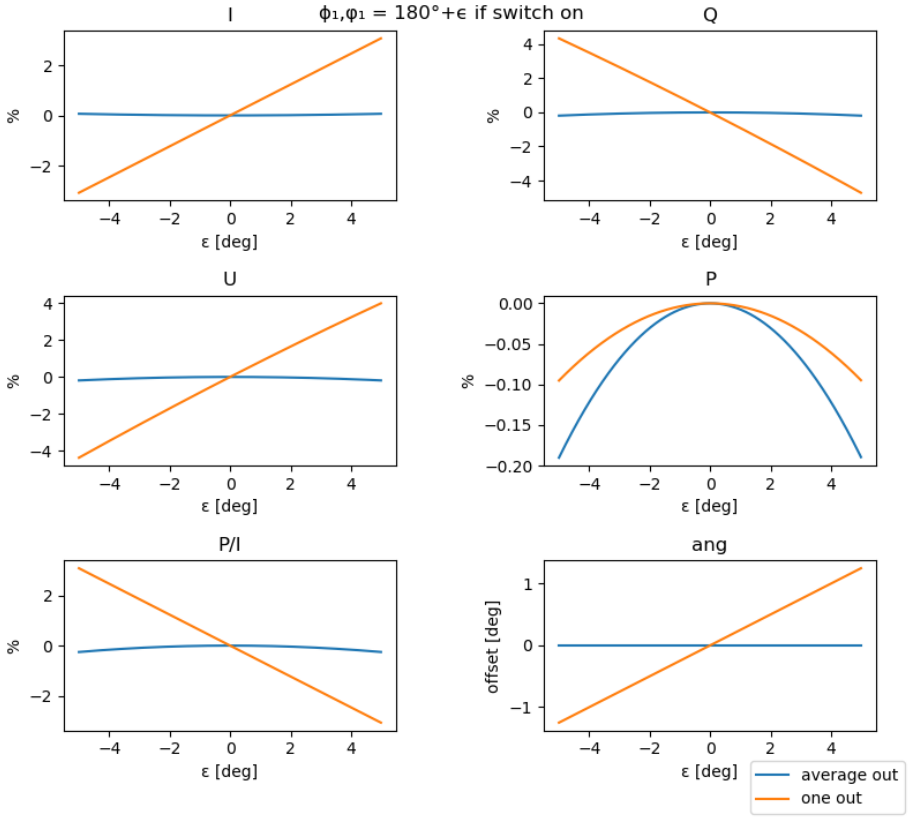

Figure 5.6: Small offset in the first and third phase switches when on

Two cases can be taken into account: when we take as output a single input state or the average between the degenerate four (5.24). If we take simply the output of one input state, the same results as for the previous two cases occur because one of the two switches is off and the other is on. Instead, if the same offsets are applied at the two branches, they are canceled out with the averaging.

LNA gains difference

The LNA are been calibrated to ideally gain the two branches of the same amount, that for simplicity we assum $g_1 = g_2 = 1$. However, it could happen that the two gains are different, thus in this case the measured parameters would feel this unbalance. Two different case are analyzed in the following.

- The upper branch gain is fixed $g_1 = 1$ as required, instead, the second branch gain is slightly larger or small $g_2 = g_1 \cdot \epsilon$. The Jones matrix does change in

$$\mathbf{J}_{LNA} = \begin{pmatrix} g_1 & 0 \\ 0 & g_1 \cdot \epsilon \end{pmatrix} \tag{5.31}$$

  where $\epsilon \in [0.90, 1.10]$, or in other words, g_2 is 90 % – 110 % of g_1.

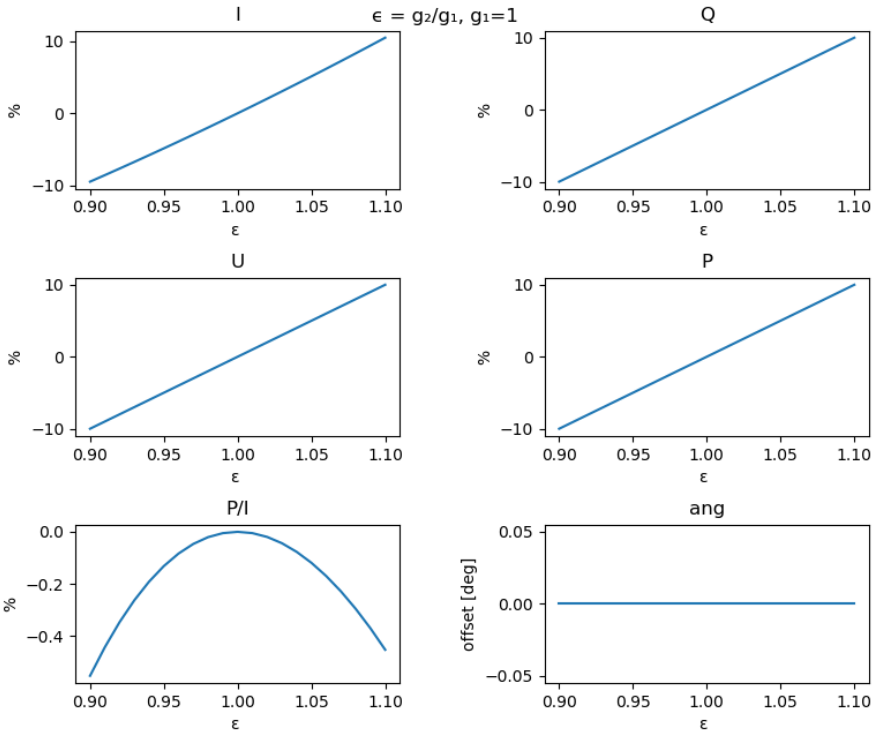

Figure 5.7: LNA gains unbalance, fixing one of them.

When the offset is applied to one of the two gains, all the Stokes parameter I, Q, U and so P increase linearly with the offset itself, indeed: if the second LNA gain is 10% larger than the first, it is simply expected all the parameters to increase of 10%. The polarization angle is not affected because U and Q increase of the same amount, thus the ratio does not change.

- The LNA are calibrate together, thus the sum of the two is fixed, but not the ratio ϵ; for instance, let impose $g_1^2 + g_2^2 = 2$, the associated Jones matrix is

$$\mathbf{J}_{LNA} = \begin{pmatrix} \frac{2}{1+\epsilon} & 0 \\ 0 & \frac{2\cdot\epsilon}{1+\epsilon} \end{pmatrix} \tag{5.32}$$

  where $\epsilon = g_2/g_1$, and $\epsilon \in [0.90, 1.10]$.

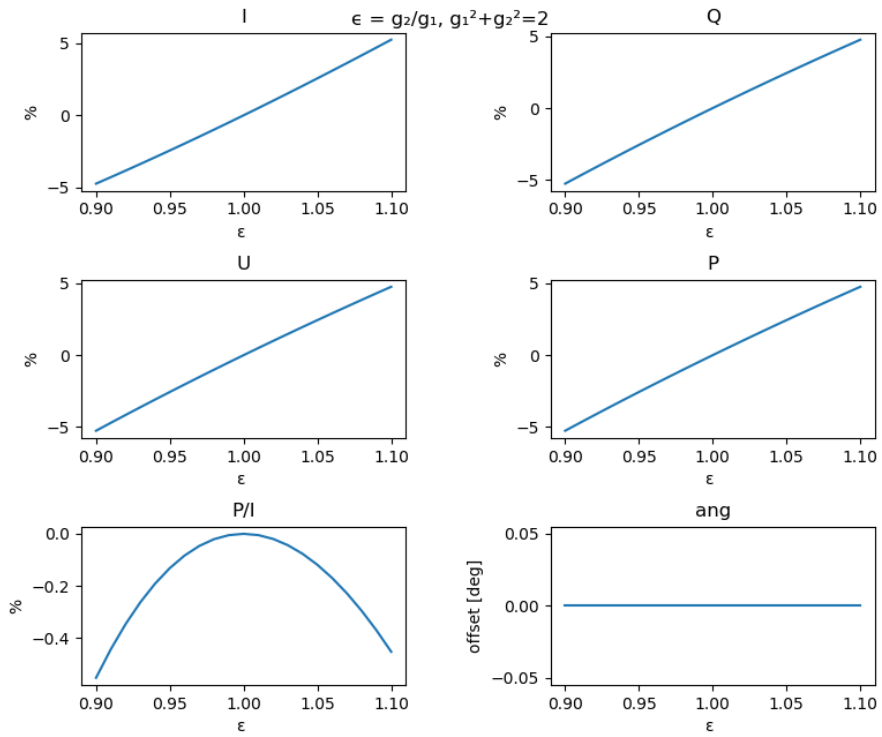

Figure 5.8: LNA gains unbalance, fixing the sum.

In these plots a notable difference between numerical and analytic analysis arise, according the expressions (5.19) the intensity should not change, instead, the simulation shows as it increases, although the slope is smaller than the previous LNA unbalance case. The Stokes Q, U and P increase linearly of the same amount of the intensity, thus, also in this case the polarization angle is not affected.

180-hybrid non-idealities
This element is designed to give as outputs the sum and the difference of the input beams, but in reality some not required gains and phase shifts can be added.
In the following we discuss some cases.

- If the additional gain or phases are added to the output signals or to both the input signals in equal amount, then, at Jones matrix level, the effects is a simple normalization factor, which at the end does not effect our Stokes parameters measurement.

$$\begin{aligned}\mathbf{J}_{hyb} &= \frac{1}{\sqrt{2}}\begin{pmatrix} g_x e^{i\psi} & g_x e^{i\psi} \\ -g_x e^{i\psi} & g_x e^{i\psi}\end{pmatrix} \\ &= \frac{1}{\sqrt{2}} g_x e^{i\psi}\begin{pmatrix} 1 & 1 \\ -1 & 1\end{pmatrix} = g_x e^{i\psi}\mathbf{J}_{hyb}\end{aligned} \tag{5.33}$$

- If the additional gain or phases are added to only one of the input signals, producing an unbalance between the two outputs, the Jones matrix is

$$\mathbf{J}_{hyb} = \frac{1}{\sqrt{2}}\begin{pmatrix} 1 & g_x e^{i\psi} \\ -1 & 1\end{pmatrix}. \tag{5.34}$$

  We cannot factorize the extra contribution, thus the Stokes measurements is compromise. In particular the gain factor g_x will produce an error exactly analogous the one shown in the first LNA case (Figure 5.7). Instead, the phase shift ψ will produce an error equal to the one produced by the first non-ideality we studied, the offset in one phase switch when on (Figure 5.4).

Polarizer offset
Last important case is the non-ideality in the polarizer. This element has been designed to introduce a 90° phase to the second branch with respect to the first, but it could happen that the angle is not exactly the one required, thus the Jones matrix

$$\begin{aligned}\mathbf{J}_{Pol} &= \mathcal{R}(\pi/4)\ \mathbf{J}_{Ret}\ \mathcal{R}^{-1}(\pi/4) \\ &= \frac{1}{2}\begin{pmatrix} 1 & -1 \\ 1 & 1\end{pmatrix}\begin{pmatrix} 1 & 0 \\ 0 & e^{i\lambda}\end{pmatrix}\begin{pmatrix} 1 & 1 \\ -1 & 1\end{pmatrix}\end{aligned} \tag{5.35}$$

where $\lambda = 90° + \epsilon$ and $\epsilon \in [-90°, 90°]$

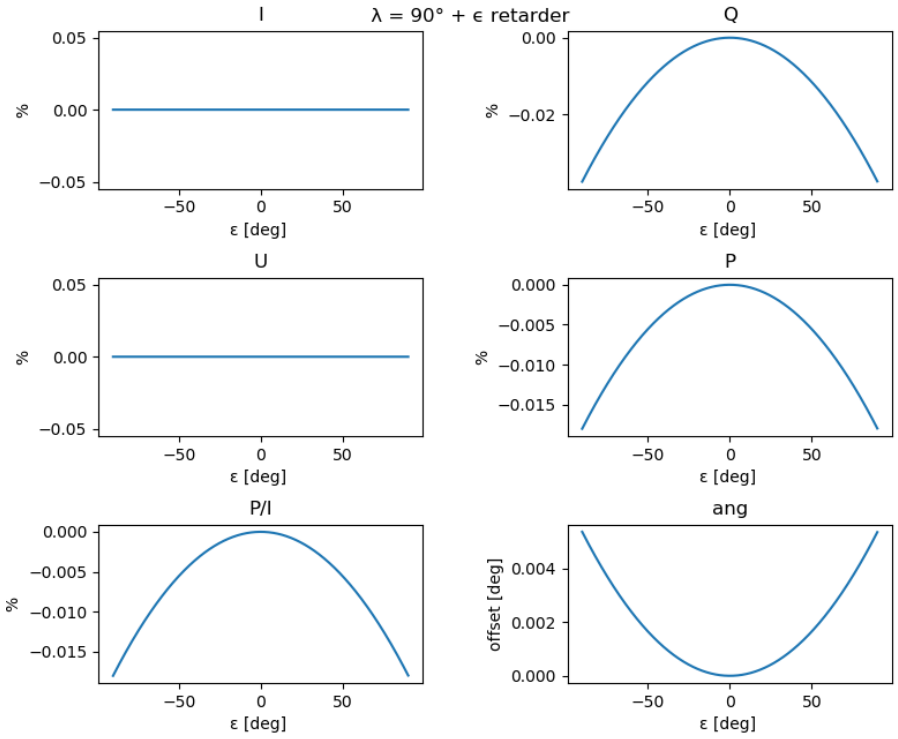

Figure 5.9: Polarizer offset

This non-ideality introduce an overall error which is very small compared to the previous ones, in the limit case $\pm 90°$, the error in the polarization intensity is of 0.02%. Nevertheless, a very peculiar effect occur, i.e. an offset arises only in the Q component and not in U component, thus, a small error in the polarization angle is shown.

5.4 Results and Discussion

The TGI and FGI channel instruments are powerful and consistent experimental set up in order to study the CMB temperature anisotropy and polarization. The ideal schemes allowed us to measure directly from the instruments the Stokes parameters without any further and complicated data processing, but simply with the use of circuit elements as phase switches.
The discussion about the non-idealities that could occur at instrumental level leads to two important conclusion:

- Errors in the elements affect the final outputs and our measurements. Nevertheless, displacements in the Stokes parameters linearly depend on the instrumental error we introduce, thus, we can calibrate them. For example, a possible unbalance gain between the Q and U can be canceled out calibrating the polarization angle γ.
- We showed how the Stokes parameters can be computed in principle in two

different ways (5.24). However, non-idealities simulations show as using average between four states mitigates, or sometimes removes, some errors.

Appendices

Appendix A

Spherical Geometry

A.1 Geometry on the Two-Sphere

The metric, on the two-sphere, expressed in spherical polar coordinates θ, ϕ is

$$g_{ab} = \begin{pmatrix} 1 & 0 \\ 0 & \sin^2\theta \end{pmatrix}. \tag{A.1}$$

In the following, we present a list of some important definitions and properties concerning the geometry on a two-sphere.

- Covariant derivatives of scalar, vector, and tensor fields are

$$\begin{aligned} S_{;a} &= S_{,a} \\ V^a{}_{;b} &= V^a{}_{,b} + V^c\Gamma^a_{bc} \\ T^{ab}{}_{;c} &= T^{ab}{}_{,c} + T^{db}\Gamma^a_{cd} + T^{ad}\Gamma^b_{cd} \end{aligned} \tag{A.2}$$

  where the symbol : denotes the covariant derivative and the comma the simple partial derivative $S_{,a} = (\partial S/\partial x^\alpha)$.

- The Christoffel symbols are

$$\Gamma^a_{bc} = \frac{1}{2} g^{ad}(g_{db,c} + g_{dc,b} - g_{bc,d}) \tag{A.3}$$

- The followings equalities hold

$$\begin{aligned} S^{:ab}{}_{ab} &= \nabla^2\nabla^2 S + R^{db}S_{:db} + \frac{1}{2}R^{:d}S_{:d} \\ \nabla^2 S \equiv S^{:a}{}_a \quad R_{ab} &\equiv R^c{}_{acb} \quad R \equiv R^a{}_a \end{aligned} \tag{A.4}$$

- Since the sphere has no boundary, the following holds

$$\oint d^2\hat{n}\sqrt{g}X^{ab}Y_{:ab} = -\oint d^2\hat{n}\sqrt{g}X^{ab}{}_{:a}Y_{:b} = \oint d^2\hat{n}\sqrt{g}X^{ab}{}_{:ba}Y \tag{A.5}$$

  where $Y(\hat{n})$ is a scalar function and $\oint d^2\hat{n}$ denotes integration over the sphere.

- The antisymmetric tensor is

$$\epsilon_{ab} = \sqrt{g} \begin{pmatrix} 0 & 1 \\ -1 & 0 \end{pmatrix} \tag{A.6}$$

with the properties

$$\begin{aligned} \epsilon_{ca}\epsilon^{c}{}_{b} &= g_{ab} = -\epsilon_{ac}\epsilon^{c}{}_{b} \\ \epsilon_{ab}\epsilon_{cd} &= g_{ac}g_{bd} - g_{ad}g_{bc} \\ \epsilon_{ab:c} &= 0 \\ \epsilon^{ab}T_{ab} &= 0 \end{aligned} \tag{A.7}$$

where $T_{ab} = T_{ba}$ isa symmetric tensor.

- The Riemann tensor is

$$R_{abcd} = \frac{1}{2} R\, \epsilon_{ab}\epsilon_{cd} \tag{A.8}$$

with the following properties

$$\begin{aligned} R_{ab} &= \frac{1}{2} R\, g_{ab} \\ \epsilon^{ab}R_{abcd} &= R\, \epsilon_{cd} \\ \epsilon^{ac}R_{abcd} &= \frac{1}{2} R\, \epsilon_{bd} \end{aligned} \tag{A.9}$$

- For two STF tensors M_{ab}, N_{ab} i.e.

$$g^{ab}M_{ab} = g^{ab}N_{ab} = \epsilon^{ab}M_{ab} = \epsilon^{ab}N_{ab} = 0,$$

the second of Eqs. (A.7) gives us

$$M^{ab}N^{cd}\epsilon_{ac}\epsilon_{bd} = -M^{ab}N_{ab}, \tag{A.10}$$

therefore, the following hold

$$g = |g_{ab}| = \sin^2\theta, \qquad \epsilon^{a}_{b} = \begin{pmatrix} 0 & \sin\theta \\ -\csc\theta & 0 \end{pmatrix}, \tag{A.11}$$

$$\Gamma^{\theta}_{\phi\phi} = -\sin\theta\cos\theta, \qquad \Gamma^{\phi}_{\theta\phi} = \Gamma^{\phi}_{\phi\theta} = \cot\theta, \tag{A.12}$$

and all other components are null.

- Some properties of a scalar function $Y(\hat{n})$ are

$$\begin{aligned} Y_{:\theta\theta} &= Y_{,\theta\theta}, \\ Y_{:\theta\phi} &= Y_{,\theta\phi} - \cot\theta\, Y_{,\phi}, \\ Y_{:\phi\phi} &= Y_{,\phi\phi} + \sin\theta\cos\theta Y_{,\theta}\,. \end{aligned} \tag{A.13}$$

- A symmetric rank-2 tensor M_{ab} has 'divergence' component

$$\begin{aligned} M^{ab}{}_{:ab} = {} & M^{\theta\theta}{}_{,\theta\theta} + 2M^{\theta\phi}{}_{,\theta\phi} + M^{\phi\phi}{}_{,\phi\phi} \\ & - \sin\theta\cos\theta M^{\phi\phi}{}_{,\theta} + 2\cot\theta M^{\theta\theta}{}_{,\theta} + 4\cot\theta M^{\theta\phi}{}_{,\phi} \\ & + (1 - 3\cos^2\theta)M^{\phi\phi} - M^{\theta\theta}, \end{aligned} \tag{A.14}$$

and 'curl' component

$$\begin{aligned} M^{ab}{}_{:ac}\epsilon^{c}{}_{b} = {} & \sin\theta\left(M^{\theta\phi}{}_{,\theta\theta} + M^{\phi\phi}{}_{,\phi\theta}\right) - \csc\theta\left(M^{\theta\theta}{}_{,\theta\phi} + M^{\phi\theta}{}_{,\phi\phi}\right) \\ & - \cot\theta\csc\theta M^{\theta\theta}{}_{,\phi} + 5\cos\theta M^{\theta\phi}{}_{,\theta} + 3\cos\theta M^{\phi\phi}{}_{,\phi} \\ & + 3\left(\cos\theta\cot\theta - \sin\theta\right)M^{\theta\phi}, \end{aligned} \tag{A.15}$$

A.2 Radial Function

In the following, we show how the lowest radial functions $j_\ell^{(\ell',m)}$ are related to the common Bessel functions of the first kind j_ℓ, i.e. the solutions of the Bessel's differential equation.
In particular for $\ell' = 0$ and $m = 0$

$$j_\ell^{(00)}(x) = j_\ell(x) \tag{A.16}$$

for $\ell' = 1$ and $m = 0, 1$

$$\begin{aligned} j_\ell^{(10)}(x) &= j'_\ell(x) \\ j_\ell^{(11)}(x) &= \sqrt{\frac{\ell(\ell+1)}{2}}\frac{j_\ell(x)}{x} \end{aligned} \tag{A.17}$$

for $\ell' = 2$ and $m = 0, 1, 2$

$$\begin{aligned} j_\ell^{(20)}(x) &= \frac{1}{2}[3j''_\ell(x) + j_\ell(x)] \\ j_\ell^{(21)}(x) &= \sqrt{\frac{3\ell(\ell+1)}{2}}\left(\frac{j_\ell(x)}{x}\right)' \\ j_\ell^{(22)}(x) &= \sqrt{\frac{3}{8}\frac{(\ell+2)!}{(\ell-2)!}}\frac{j_\ell(x)}{x^2}. \end{aligned} \tag{A.18}$$

Knowing the relations between $\epsilon_\ell^{(m)}$ and $\beta_\ell^{(m)}$ with the radial functions $j_\ell^{(\ell',m)}$, we can find equations which describe the lowest order of these new two functions in terms on Bessel function j_ℓ. For $\epsilon_\ell^{(m)}$

$$\begin{aligned} \epsilon_\ell^{(0)}(x) &= \sqrt{\frac{3}{8}\frac{(\ell+2)!}{(\ell-2)!}}\frac{j_\ell(x)}{x^2} \\ \epsilon_\ell^{(1)}(x) &= \frac{1}{2}\sqrt{(\ell-1)(\ell+2)}\left[\frac{j_\ell(x)}{x^2} + \frac{j'_\ell(x)}{x}\right] \\ \epsilon_\ell^{(2)}(x) &= \frac{1}{4}\left[-j_\ell(x) + j''_\ell(x) + 2\frac{j_\ell(x)}{x^2} + 4\frac{j'_\ell(x)}{x}\right] \end{aligned}$$

which corresponds to the $\ell' = \ell, \ell \pm 2$ coupling, and for $\beta_\ell^{(m)}$

$$\begin{aligned} \beta_\ell^{(0)}(x) &= 0 \\ \beta_\ell^{(1)}(x) &= \frac{1}{2}\sqrt{(\ell-1)(\ell+2)}\frac{j_\ell(x)}{x} \\ \beta_\ell^{(2)}(x) &= \frac{1}{2}\left[j'_\ell(x) + 2\frac{j_\ell(x)}{x}\right] \end{aligned} \tag{A.19}$$

which corresponds to the $\ell' = \ell \pm 1$ coupling. The m-reversal functions are given by the simply found by the symmetric and antisymmetric properties

$$\begin{aligned} \epsilon_\ell^{(-m)} &= \epsilon_\ell^{(m)} \\ \beta_\ell^{(-m)} &= -\beta_\ell^{(m)}. \end{aligned} \tag{A.20}$$

Appendix B

Astrophysical Coordinates

B.1 Celestial and Horizon Coordinates

In Astronomy and Astrophysics, it is simple to consider all the celestial objects on an ideal sphere, called celestial sphere, centered in the Earth. The celestial equator is then the projection of the Earth equator on the celestial sphere and the Sun trajectory on the celestial sphere is simple called ecliptic.
Let introduce a Cartesian reference frame with origin in the Earth location and with the x- and y-axes in the equatorial plane. The celestial object position is described by means of two angles: the *right ascension* (α), taken counterclockwise from the positive X axes, and the *declination* (δ), taken up from the equatorial plane.
In formulas, if a point on the celestial sphere is identified by a vector $\mathbf{r} = (x, y, z)$, the celestial angular coordinates can be recovered by

$$\alpha = \begin{cases} \arctan(y/x) & x, y > 0 \\ \pi + \arctan(y/x) & x, y < 0 \\ \pi - \arctan(y/x) & x \cdot y < 0 \end{cases} . \quad \text{(B.1)}$$

and

$$\delta = \arcsin \frac{z}{\sqrt{x^2 + y^2 + z^2}}. \quad \text{(B.2)}$$

The problem of this definition is that the Earth itself is moving and its axis is precessing, thus the points where the celestial equator intersects the ecliptic change with time. The Earth-Sun system dynamics can be described by two different rotations: a steady precession, that changes the direction where the Earth axis points, and a residual wobbling called nutation.
Therefore, to have a standard and worldwide used definition we need to refer to a specific reference: the International Celestial Reference Systems (ICRS), i.e. the coordinates are given with respect to the mean equator and equinox of the year J2000, where 'J' refers to the Julian Calendar.
The Julian Date is a common way of expressing absolute time in astronomy, which counts date and hours starting from the 12.00 pm on January 1, 4713 BC in the proleptic Julian Calendar.

In perfect analogy with the celestial coordinates, we introduce a Cartesian reference frame centered on the observer site, where the x-axis is pointing south, the y-axis points east and the z-axis points to the zenith. the x and y axes lie on a plane tangent

to the Earth surface at the observing site, the z axis is perpendicular to this plane and points away to the sky. A point on the sky is aimed by means of two angles: the *azimuth* (A), measured in the horizontal plane starting from north and going through east, and the *elevation* (E), measured up with respect to the horizontal plane. In formulas, if a point on the celestial sphere is identified by a vector $\mathbf{r} = (x, y, z)$, the horizon angular coordinates can be recovered by

$$A = \begin{cases} \pi - \arctan(y/x) & x > 0 \\ 2\pi - \arctan(y/x) & x < 0, y > 0 \\ -\arctan(y/x) & x < 0, y < 0 \end{cases} . \quad \text{(B.3)}$$

and

$$E = \arcsin \frac{z}{\sqrt{x^2 + y^2 + z^2}}. \quad \text{(B.4)}$$

B.2 Coordinates Transformation

In this section, we present how the transformation from celestial to horizon coordinates is performed; in formulas, we are looking in

$$\mathbf{r}_{hor} = \mathcal{R}_{SH} \mathbf{r}_{pm} \quad \text{(B.5)}$$

for the rotation $\mathcal{R}_{SH}$.
Thus, the matrix in equation (B.5) can be performed by the product of two matrices

$$\mathcal{R}_{SH} = \mathcal{R}_{\xi}^{z} \cdot \mathcal{R}_{L}^{y} \quad \text{(B.6)}$$

which represent

- Rotation around the y-axis in order to align the celestial z-axis to the horizon z-axis

$$\mathcal{R}_{L}^{y} = \begin{pmatrix} \cos\left(\frac{\pi}{2} - L\right) & 0 & \sin\left(\frac{\pi}{2} - L\right) \\ 0 & 1 & 0 \\ -\sin\left(\frac{\pi}{2} - L\right) & 0 & \cos\left(\frac{\pi}{2} - L\right) \end{pmatrix} \quad \text{(B.7)}$$

  where L is the latitude of the observing site.

- Rotation around the z-axis in order to align the celestial and horizon (x, y)-plane orientation

$$\mathcal{R}_{\xi}^{z} = \begin{pmatrix} \cos\xi & -\sin\xi & 0 \\ \sin\xi & \cos\xi & 0 \\ 0 & 0 & 1 \end{pmatrix} \quad \text{(B.8)}$$

  where ξ is the *local sidereal time*: the time, expressed in hours, elapsed since the last transit of the Spring Equinox across the local meridian..

This computation is very basic and simplified, in reality we should take into account different effects due to the system dynamics, we simple list some of these in the following:

- Earth precessional motion: rotation of the Earth's rotation axis, due to the gravitational interaction of the Earth with the Moon and the Sun
- Earth nutation motion: variation of the opening angle of the precessional cone, due to the gravitational torque exerted on Earth by the other bodies in the solar system

- Aberration: a relativistic effect, which consist of a variation of the propagation direction of a light ray when observed from two reference frames in relative motion, it is due to the fact that the velocity of light is finite
- Atmospheric refraction: light refraction in the Earth atmosphere, which increases the apparent elevation of the target, the effect being larger at lower elevations.

Bibliography

[1] Scott Dodelson (2003), *Modern Cosmology*. Academic Press, 2^{nd} Edition

[2] Barbara Ryden (2016), *Introduction to Cosmology*. Cambridge University Press, 2^{nd} Edition

[3] Andrew R. Liddle and David H. Lyth (2000), *Cosmological Inflation and Large-Scale Structure*. Cambridge University Press

[4] Arthur Kosowsky, *Cosmic Microwave Background Polarization*. Annals Phys. 246 (1996) 49-85

[5] Paolo Cabella and Marc Kamionkowski, *Theory of Cosmic Microwave Background Polarization*. e-Print: arXiv:astro-ph/0403392

[6] Wikipedia contributors, *Stokes parameters in some degenerate cases*. url: en.wikipedia.org/wiki/Image:Side2.png

[7] Wayne Hu and Martin White, *A CMB Polarization Primer*. New Astronomy 2 (1997) 323

[8] Wayne Hu and Martin White, *CMB anisotropies: Total angular momentum method*. Phys.Rev.D 56:596-615, 1997

[9] C.L. Bennett *et al.*, *Scientific results from COBE*. Advances in Space Research, vol.13, no.12, P.(12)409-(12)423

[10] E. M. Leitch *et al.*, *Experiment Design and First Season Observations with the Degree Angular Scale Interferometer*. The Astrophysical Journal 568(1):28

[11] S. Padin *et al.*, *The Cosmic Background Imager*. Publ.Astron.Soc.Pac. 114 (2002) 83

[12] Goddard Space Flight Center, *Wilkinson Microwave Anisotropy Probe: Overview*. url: lambda.gsfc.nasa.gov/product/map/current/

[13] Planck Collaboration (Y. Akrami *et al.*), *Planck 2018 results. I. Overview and the cosmological legacy of Planck*. e-Print: arXiv:1807.06205 [astro-ph.CO]

[14] P.A.R. Ade *et al.* (Keck Array and BICEP2 Collaborations), *Improved Constraints on Cosmology and Foregrounds from BICEP2 and Keck Array Cosmic Microwave Background Data with Inclusion of 95 GHz Band*. Phys. Rev. Lett. 116, 031302

[15] Clive Dickinson, *CMB foregrounds - A brief review.* e-Print: arXiv:1606.03606 [astro-ph.CO]

[16] Planck Collaboration (R. Adam *et al.*), *Planck 2015 results. X. Diffuse component separation: Foreground maps.* Astron.Astrophys. 594 (2016) A10

[17] QUIJOTE Collaboration (F. Poidevin *et al.*, *The QUIJOTE Experiment: Prospects for CMB B-MODE polarization detection and foregrounds characterization.* e-Print: arXiv:1802.04594 [astro-ph.CO]

[18] QUIJOTE Collaboration (J. A. Rubiño-Martín *et al.*), *The Quijote CMB Experiment.* Highlights of Spanish Astrophysics V

[19] url: http://www.radioforegrounds.eu

[20] R. Génova-Santos *et al.*, *Measurements of the Intensity and Polarization of the Anomalous Microwave Emission in the Perseus molecular complex with QUIJOTE.* Mon.Not.Roy.Astron.Soc. 452 (2015) no.4, 4169-4182

[21] R. Génova-Santos *et al.*, *QUIJOTE Scientific Results. II. Polarisation Measurements of the Microwave Emission in the Galactic molecular complexes W43 and W47 and supernova remnant W44.* Mon.Not.Roy.Astron.Soc. 464 (2017) no.4, 4107-4132

[22] Patrick T. Wallace, *Concise Telescope Pointing Algorithm Using IAU 2000 Precepts.* Proc. of SPIE Vol. 7019, 701908, (2008)

[23] Denis Tramonte, *Using CMB, LSS and Galaxy Clusters as Cosmological Probes.* IAC Department of Astrophysics PhD theses archive

[24] Jean Kovalevsky, *Modern Astrometry.* Astronomy And Astrophysics Library, Springer

[25] HEALPIX website, url: healpix.jpl.nasa.gov

[26] Jones E, Oliphant E, Peterson P, *et al.*, *SciPy: Open Source Scientific Tools for Python.* url: http://www.scipy.org/

[27] John D. Hunter, *Matplotlib: A 2D Graphics Environment.* Computing in Science Engineering, 9, 90-95 (2007)